On the Exploitation of Mode Localization in Surface Acoustic Wave MEMS for Sensing Applications

A thesis submitted to the Faculty of Science, Agriculture and Engineering for the Degree of Doctor of Philosophy

By

Thomas H. Hanley

School of Mechanical and Systems Engineering

Newcastle University

March 2017

Abstract

Mode localization refers to the spatial trapping of energy in a coupled oscillatory system that occurs when a disorder is introduced into a previously ordered system. This thesis explores the exploitation of this phenomenon in surface acoustic wave (SAW) devices for sensing applications. The sensing application of primary focus within this work is a magnetic field sensor, wherein the strength of mode localization changes in proportion to an external magnetic field. In addition, application as a bio-mass sensor is suggested and briefly discussed.

Utilisation of mode localization as a sense mechanism involves the use of changes in the normalised mode shape of a weakly-coupled two degree-of-freedom system as the sensor output. This is in contrast to the use of shifts in frequency, phase or amplitude as is commonplace in resonant micro-electromechanical systems (MEMS) sensor technology. The theory and principles of device operation are introduced utilising a discretised model. In particular, the use of a periodic array to couple the sensors' two degrees-of-freedom is investigated. A generalised geometry of the SAW device is introduced, consisting of a pair of acoustically-coupled cavities. An analytical solution is found for the displacement fields within the cavities. The solution is achieved by coupling the internal cavity solutions using a ray tracing method. The results of the analytical solution are compared to a numerical solution found using commercial finite element analysis (FEA) software; good agreement is observed.

The model is subsequently used to analyse and discuss device performance in the presence of noise; expressions are presented describing device operation and performance, and a case study is outlined evaluating use as a MEMS magnetometer. Finally, the design, manufacture and testing of a prototype design is discussed.

Acknowledgements

Foremost, I would like to express my sincere gratitude to my principle supervisor Dr Barry Gallacher for encouraging and enabling me to embark upon this period of research. Barry's passion to continually develop and explore new ideas has been inspiring. The many animated exchanges have been a highlight of my time within the research group, as well as being hugely beneficial to my understanding of mechanics and dynamic systems. I would also like to thank Dr Harry Grigg for always finding time to lend an erudite ear, the unique insights he provided have had influences on many aspects of the work.

Thanks are also due to Dr Carl Dale for his help and advice in the lab and to Dr Chen Fu for the manufacture of the prototype devices. As well as all of the postgraduate researchers whom I've had the pleasure of studying alongside.

I am indebted to my family for their unwavering support and to Tom Hepburn for reminding me, when necessary, that there was a world outside of the books. Finally, I owe a great debt to my partner Anna, whose endless support and encouragement has enabled me to complete this thesis. I cannot thank you enough.

Table of Contents

Table of Figures

List of Symbols

Terms will be described in the text as they are introduced. All variables should be considered scalar unless one of the following formats is applied: vectors are represented as lower- or upper-case, underlined characters, e.g. $\underline{u}$, $\underline{F}$; matrices are shown in upper case bold e.g. **U**. When convenient, over-dots are used to denote time differentiation. A term with an over-tilde refers to a defined non-dimensional parameter e.g. $\widetilde{\Omega}$ and a term with an over-bar refers to a parameter, or equivalent lumped parameter, describing a region of 'plated' elastic half-space e.g. $\bar{k}$ is the equivalent lumped stiffness of a region of plated elastic half-space.

Chapter 1

λ	Wavelength	ω	Angular frequency
μ	Propagation constant	d	Period of a lattice of particles
m	Mass	Δm	Change in mass
δ	Non-dimensional mass perturbation	k	Stiffness of an anchoring spring
k_C	Stiffness of a coupling spring	κ	Non-dimensional coupling spring stiffness
F_i	Force applied to i^{th} degree of freedom	u_i	Displacement of the i^{th} degree of freedom
${\lambda_0}^{(i)}$	i^{th} eigenvalue	$\lambda_p^{(i)}$	i^{th} perturbed eigenvalue
$\underline{u_0^{(i)}}$	i^{th} eigenvector	$\underline{u_p^{(i)}}$	i^{th} perturbed eigenvector
M	Mass matrix	**δM**	Mass perturbation matrix
K	Stiffness matrix	**δK**	Stiffness perturbation matrix
Z	Dynamic stiffness matrix	**T**	Transfer matrix
I	Identity matrix		

Chapter 2

m	Equivalent lumped mass of an un-plated region	$\overline{m}$	Equivalent lumped mass of a plated region
m_p	Perturbed mass	$\widetilde{m}$	Non-dimensional mass of plated region
$\widetilde{m_p}$	Non dimensional perturbed mass	k	Equivalent lumped stiffness of an un-plated region
$\overline{k}$	Equivalent lumped stiffness of a plated region	k_p	Perturbed stiffness
$\tilde{k}$	Non-dimensional stiffness of plated region	$\widetilde{k_p}$	Non-dimensional perturbed stiffness
ω_n	Natural frequency	t	Time
Ω	Excitation frequency	$\widetilde{\Omega}$	Non-dimensional excitation frequency
$\underline{u}$	Displacement vector	$\underline{F}$	Forcing vector
F	Scalar force	N	Number of periods in coupling array
ς	Simplification parameter	α_c	Cross receptance
β	Rayleigh stiffness proportional damping coefficient	$\widetilde{\mathbf{M}}$	Non-dimensional mass matrix
$\widetilde{\mathbf{K}}$	Non-dimensional stiffness matrix	$\mathbf{C}$	Damping matrix

Chapter 3

x_i	i^{th} spatial coordinate	$\underline{u}$	Displacement field vector
u_i	i^{th} component of displacement	$\underline{\tau}$	Stress vector
τ_{ii}	ii^{th} stress field component	ρ	Density
∇	Gradient operator	v	Poisson's ratio
λ_L	Lame's first parameter	μ_L	Lame's second parameter

c_T	Transverse wave speed	c_R	Rayleigh wave speed
γ	Wavenumber in the direction of propagation (x_1-direction)	c_L	Longitudinal wave speed
φ_j	j^{th} component of integrated depth behaviour	ξ	Depth wavenumber (x_2-direction)
T^s	Surface stress field	ψ	Surface displacement field
$\delta(x)$	Dirac delta function	P	Line load
$\nabla \cdot \underline{u}$	Divergence of $\underline{u}$	$\mathcal{F}, \mathcal{F}^{-1}$	Fourier transform pair
$\mathbf{d}$	Piezoelectric coefficient matrix	$\nabla \times \underline{u}$	Curl of $\underline{u}$
$\mathbf{e}$	Dielectric permittivity matrix	I_{uii}	Fourier inversion integral
$\underline{\mathrm{E}}$	Electric field vector	$\underline{\mathrm{D}}$	Charge density vector
$\underline{\varepsilon}$	Strain vector	$\mathbf{C}$	Elasticity matrix
s	Period of array	d	Half distance of plated region
$\underline{\Psi_n}$	State vector	$\mathbf{D}$	Differential operator matrix
$\mathbf{P}$	Phase matrix	$\underline{\phi_n}$	Transfer matrix amplitude vector
w	Upper left component of transfer matrix	z	Upper right component of transfer matrix
$\mathbf{Z}$	Shifted transfer matrix	m	Scalar in characteristic equation
ζ	Half the trace of $\mathbf{Z}$	$U_N(\zeta)$	N^{th} Chebyshev polynominal of the second kind
T_N	Transmission coefficient	R_N	Reflection coefficient
$\widetilde{T_N}$	Non-dimensional transmission coefficient	$\widetilde{R_N}$	Non-dimensional reflection coefficient
$\widetilde{c_R}$	Non-dimensional Rayleigh wave speed	r	Plating ratio

f	Frequency	a	Length of reference cavity
b	Length of sense cavity	x_R	Location of forcing in reference cavity
x_R	Location of forcing in sense cavity	η	Cavity wave speed ratio
χ_α	Path expression	R_C	Coupling array reflection coefficient
R_R	Reference cavity enclosing array reflection coefficient	R_S	Sense cavity enclosing array reflection coefficient
T_C	Coupling array transmission coefficient	$\Gamma, \Gamma_R, \Gamma_S$	Path expression products
ψ_R	Reference cavity surface displacement field	ψ_S	Sense cavity surface displacement field
Λ	Denominator of cavity displacement fields	$P_{\mathrm{REF}}, P_{SENSE}$	Cavity Line loads
$G_{\mathrm{SS}}, G_{\mathrm{RR}}$ $G_{\mathrm{RS}}, G_{\mathrm{SR}}$	Frequency response functions	α_L	Attenuation coefficient
T_{CL}	Lossy transmission coefficient	L_{CA}	Coupling array length

Chapter 4

$\widetilde{\Omega}_n$	Non-dimensional resonant frequency	$\widetilde{L_{eq}}$	Non-dimensional equivalent coupling array length
ϑ	Phase shift through coupling array	ϕ	Phase of R_C
S	Sensitivity	Q	Quality factor
N_C	Number of periods in coupling array		

Chapter 5

C_1	Linear approximation coefficient	ζ_a	Material anisotropy coefficient
α_d	Dissipation parameter	b_w	Beam width
T	Temperature	k_B	Boltzmann constant
c_d	Damping coefficient	$F_{mech-therm}$	Force due to mechanical-thermal noise
$\mathrm{E_I}$	Inertial energy of a cavity	m_{eq}	Equivalent mass of a cavity
L_C	Cavity length	L_w	Device width
ψ_{noise}	Surface displacement due to noise		

Chapter 1. Introduction

1.1 Problem statement and motivation

In the field of micro-electromechanical systems (MEMS) it is commonplace for sensors to be designed to utilise a mechanical resonator for transduction, devices within this subset are termed resonant MEMS sensors. The output of such a device is typically the change in frequency, amplitude or phase of the mechanical resonance in proportion to some external influence. Common applications include gyroscopes, accelerometers, magnetometers, pressure sensors and mass sensors. This thesis concerns an emerging subset of resonant MEMS sensors which utilise an alternative resonant sensing protocol. These emerging devices use mode localization as the output metric rather than the aforementioned sensing techniques. This is explored with the primary motivation of developing a high signal-to-noise ratio (SNR) MEMS magnetometer. In addition, it is suggested that the principle of operation can be used to develop a robust, high-sensitivity MEMS bio-mass sensor.

Mode localization refers to the spatial trapping of energy in a coupled oscillatory system that occurs when a disorder is introduced into a previously ordered system. Mode localization sensing has recently emerged as an alternative resonant sensing protocol, with particular prominence in the field of MEMS. It has been shown to exhibit several advantages over other resonant methods, in particular a potential for higher sensitivity and rejection of common mode noise. Mode localization sensors have been approached primarily in the case of two weakly coupled symmetrical oscillators [1]–[3]. The current work extends this theory to encompass the use of periodic structures to couple the resonators. The use of periodic arrays presents potential sensitivity advantages and opens up the feasible choices of geometry.

Realisation through the use of a surface acoustic wave (SAW) architecture is asserted from the outset. The use of SAW, already ubiquitous in microelectronic filters, presents many advantages when compared to the alternative of constructing periodic arrays of suspended MEMS. For one, the short wavelengths can allow long periodic structures whilst maintaining small device size. Furthermore, the SAW devices require a simple

and inherently robust architecture; there are no deep cavity etches or slender beams and the manufacturing process is well established.

1.2 Contribution

The predominant contribution of the current work as a whole is the design of a novel SAW MEMS sensor utilising mode localization in periodic structures. This is detailed from the concept and basic theory of operation (chapter 2), through to the performance (chapter 4) and limitations on functionality (chapter 5). This thesis outlines the concept, and proposes both a design and a potential application of the sensor (chapter 6).

Much of the related work has focused predominantly on application and implementation of mode localization sensing, performing numerical simulations and harvesting valuable experimental data from prototype devices. In addition to presenting and appraising a novel sensor design, this thesis aims to take a step back to explore the phenomenon more deeply from an analytical mechanics viewpoint. One of the main contributions of the current work is presented in chapter 3, detailing a general analytical model for localization in periodically patterned surface acoustic wave structures. Scrutiny of the equations can provide deeper insight into the physical phenomena at play, the causes of localization, in addition to allowing for more guided device design.

1.3 Orientation

The theoretical backbone of this work draws heavily from the vast amounts of literature extant on the well-established fields of periodic structures and localization. The impact of the work is, however, intended to refer to the more recently emerging field of MEMS mode localization sensors. A familiarity with these topics is essential for navigation of this thesis. This section is intended to review the pertinent literature and provides the reader, who is unfamiliar with any of the topics of this thesis, a brief, yet sufficient introduction to the background and principles of each topic. As the thesis progresses and more specialist topics are introduced, the relevant literature is presented where necessary.

1.2.1 Introduction to the Wave Propagation Properties of Periodic Media

Due to the expansive literature available of some relevance to the study of periodic structures, beginning as early as Newton's calculation of the velocity of sound [4], in which he employed a one-dimensional lattice of point masses. The review will not be encompassing, instead, the seminal works will be indicated, and then the fundamental phenomena and terminology associated with periodic media will be introduced. The section will close by indicating works of particular relevance to the analysis of the following chapters.

The majority of modern day analysis draws on the work of Floquet [5] and Bloch [4]. Floquet approached the problem of parametric periodicity in the time domain, which reduces to the solution of Hill's equation. It was shown that the solution was periodic and a general solution of Hill's equation was presented. Bloch approached the problem of parametric periodicity in the spatial domains from the field of solid-state physics, thus the problem was generalised to three dimensions of infinite expanse and solutions equivalent to that of Floquet where found. Two excellent and authoritative reviews are provided by both Elachi [6] and Mead [7] these cover, almost all of the work of relevance and particularly the application of periodic media to mechanical engineering. The seminal work of Brillouin [4] must be mentioned for the reader unacquainted with periodic media. The work of Brillouin outlines in great detail much of the fundamental theory used throughout this work and serves as a brilliant reference for the engineer looking to exploit the phenomena, as it has for the author.

The most prominent property possessed by periodic structures is the exhibition of distinct regions in the frequency domain in which waves are alternately propagated or are attenuated. These are known as 'pass-bands' and 'stop-bands' respectively. Some authors prefer the phrases, 'propagation-zone' and 'attenuation-zone', however, within this work, the former terminology will be used. The stop-bands occur when Bragg's law [4] is met, in the case of one-dimensional wave propagation, this reduces to equation 1.1.

$$d = \frac{n\,\lambda}{2} \tag{1.1}$$

With d representing the period within the array, λ the wavelength of the incident wave and n an integer. The nature of this behaviour will be demonstrated using two classical structures, the one-dimensional monatomic and diatomic lattices (Figure 1.1).

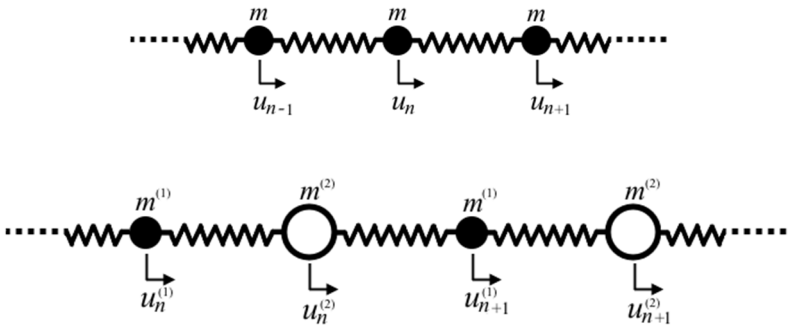

Figure 1.1 Monatomic and diatomic lattice schematics

The general solution for a wave travelling through either lattice is given in equation 1.2. The parameter μ is the complex-valued wavenumber, often referred to as the propagation constant. This defines the change in amplitude and phase of the propagating wave. The real part of the wavenumber describes the number of waves per unit distance and is defined as the reciprocal of the wavelength multiplied by 2π. The imaginary part of the wavenumber defines any attenuation or amplification of the wave in the spatial domain. The wavenumber of the array is a function of the angular frequency, ω. The dispersion spectra are obtained by plotting μ vs. ω, examples of these for the monatomic and diatomic lattices are overlaid in Figure 1.2.

$$u_n = e^{i\mu(\omega)nd} \tag{1.2}$$

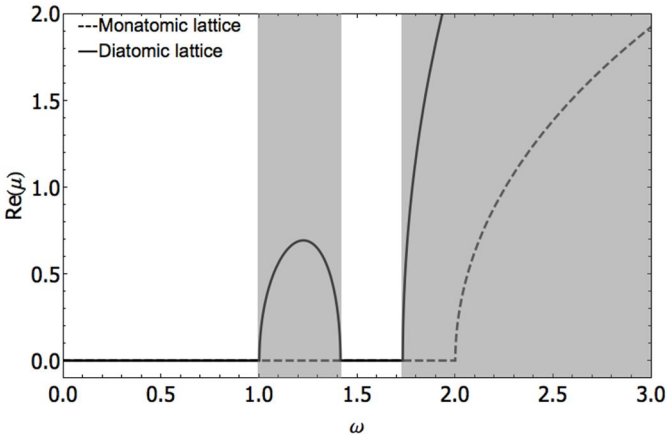

Figure 1.2 Monatomic and diatomic lattice dispersion.

The white and grey regions in Figure 1.2 represent the pass- and stop-bands of the diatomic lattice respectively. An important general property of periodic arrays is demonstrated by the spectra: the number of pass-bands in the dispersion spectrum of a periodic structure is determined by the number of degrees of freedom (DOFs) per-period. This is demonstrated by the presence of two pass-bands for the diatomic lattice and one for the monatomic lattice (Figure 1.2). If a structure is modelled as a continuous medium, then it possesses an infinite number of pass bands. A stop band emerges around each point when Bragg's law is met, the width of the stop band determined by the system parameters.

The propagation constant and the 'transfer matrix' (TM) are two tools that are ubiquitous in the study of periodic media and will be used repeatedly throughout this thesis. The derivation for the propagation constant of a 1-DOF period is straight forward, and is presented here as a simple introduction. Figure 1.3 shows one resonator from the array and its nearest neighbour coupling. Assuming simple harmonic motion with angular frequency, ω. Newton's second law can be applied to find equation 1.3.

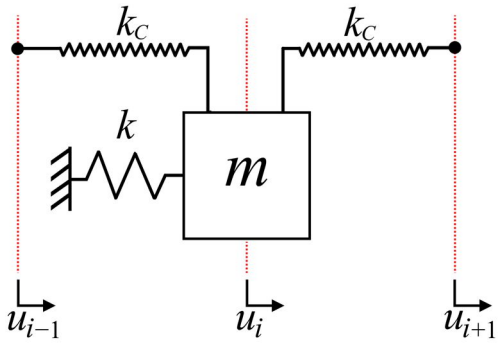

Figure 1.3 Example schematic for propagation constant derivation

$$(k + 2\,k_C - \omega^2 m)u_i - k_C\,u_{i-1} - k_C\,u_{i+1} = 0 \qquad (1.3)$$

At this point a Floquet-Bloch relationship between the DOFs is assumed (eqs. 1.4-5). The short expressions representing the Floquet-Bloch relationship insert the assumption that the system response is spatially periodic with the same period as the system. Inserting these equations into equation 1.3 and cancelling u_i throughout gives equation 1.6.

$$u_{i-1} = e^{-\mu} u_i \qquad (1.4) \qquad\qquad u_{i+1} = e^{\mu} u_i \qquad (1.5)$$

$$(k + 2\,k_C - \omega^2 m) - k_C(e^{\mu} + e^{-\mu}) = 0 \qquad (1.6)$$

This can now be solved for μ in terms of ω, the solution is given in equation 1.7.

$$\mu = ArcCosh\left(\frac{k + 2\,k_C - \omega^2 m}{2\,k_C}\right) \qquad (1.7)$$

This four line derivation provides an easy way to see the origins of the propagation constant and aid with its interpretation. Similar methods of derivation to this were used extensively by Mead [8]–[12], and fall in to a class referred to as receptance methods. Throughout this thesis however, the transfer matrix will be employed for calculating propagation constants. Although more convoluted for this simple, discrete case, the properties of the TM become very powerful when implementing boundary conditions or joining systems together. In addition to this, in the case of continuous systems, the calculation using the transfer matrix is no more long-winded than using receptance methods. As an introduction, the above calculation is repeated using the TM method. The initial schematic is redefined to aid with the derivation (Figure 1.4). Included in the schematic this time is the coupling forces between adjacent cells.

Considering the unit cell, i, Newton's second law can be applied to the DOFs on the right- and left-hand sides (eqs. 1.8 and 1.9 respectively). These can be combined to give the dynamic stiffness matrix, $\mathbf{Z}$ (eq. 1.10).

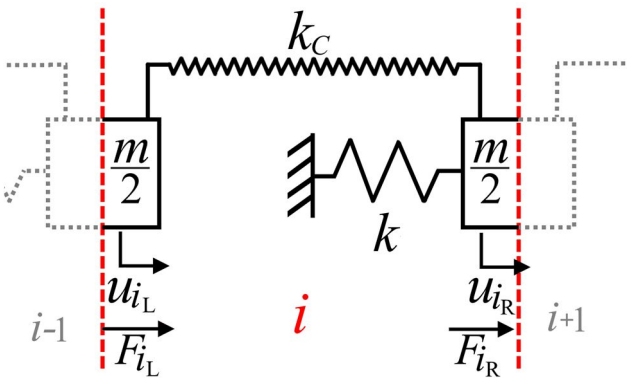

Figure 1.4 Example schematic for transfer matrix derivation

$$F_{i_R} - k_C\left(u_{i_R} - u_{i_L}\right) - k u_{i_R} = -\omega^2 \frac{m}{2} u_{i_R} \tag{1.8}$$

$$F_{i_L} - k_C\left(u_{i_L} - u_{i_R}\right) = -\omega^2 \frac{m}{2} u_{i_L} \tag{1.9}$$

$$\begin{Bmatrix} F_{i_R} \\ F_{i_L} \end{Bmatrix} = \begin{bmatrix} k + k_C - \omega^2 \frac{m}{2} & -k_C \\ -k_C & k_C - \omega^2 \frac{m}{2} \end{bmatrix} \begin{Bmatrix} u_{i_R} \\ u_{i_L} \end{Bmatrix} = \mathbf{Z} \begin{Bmatrix} u_{i_R} \\ u_{i_L} \end{Bmatrix} \tag{1.10}$$

Using simple algebraic manipulation, the system of equations in 1.10 can be rearranged and represented in terms of the 'state vectors' at the either end of the cell. This can be written in terms of the elements of the dynamic stiffness matrix in matrix form eq. 1.11 [13].

$$\begin{Bmatrix} u_{i_R} \\ F_{i_R} \end{Bmatrix} = \begin{bmatrix} \frac{-Z_{22}}{Z_{21}} & \frac{1}{Z_{21}} \\ Z_{12} - \frac{Z_{11}Z_{22}}{Z_{21}} & \frac{Z_{11}}{Z_{21}} \end{bmatrix} \begin{Bmatrix} u_{i_L} \\ F_{i_L} \end{Bmatrix} \tag{1.11}$$

Now, addressing the force and displacement continuity at the boundary between cells (eqs. 1.12 and 1.13) and inserting this into eq. 1.11 gives the transfer matrix **T** in eq. 1.14.

$$u_{i_L} = u_{i-1_R} \tag{1.12}$$

$$F_{i_L} = -F_{i-1_R} \tag{1.13}$$

$$\begin{Bmatrix} u \\ F \end{Bmatrix}_{i_R} = \begin{bmatrix} \frac{-Z_{22}}{Z_{21}} & \frac{1}{Z_{21}} \\ \frac{Z_{11}Z_{22}}{Z_{21}} - Z_{12} & \frac{-Z_{11}}{Z_{21}} \end{bmatrix} \begin{Bmatrix} u \\ F \end{Bmatrix}_{i-1_R} = \mathbf{T} \begin{Bmatrix} u \\ F \end{Bmatrix}_{i-1_R} \tag{1.14}$$

The form of the transfer matrix in eq. 1.14 is general for all mono-coupled systems and can be used once the dynamic stiffness matrix has been found. A mono-coupled system is defined as one with a single constraint coupling adjacent DOFs. A similar generalisation to multi-coupled systems is given in reference [13].

In order to obtain the propagation constant, Floquet-Bloch theory is once again asserted in the form of equation 1.15. This is equated to eq. 1.14 producing the eigenvalue problem in eq. 1.16 (where **I** is the 2x2 identity matrix).

$$\begin{Bmatrix} u \\ F \end{Bmatrix}_{i_R} = e^{\mu} \begin{Bmatrix} u \\ F \end{Bmatrix}_{i-1_R} \tag{1.15}$$

$$|\mathbf{T} - e^{\mu}\mathbf{I}| = 0 \tag{1.16}$$

The two eigenvalues, λ_0 and, $\frac{1}{\lambda_0}$ are equal to e^{μ} and $e^{-\mu}$ respectively [13] therefore:

$$e^{\mu} + e^{-\mu} = 2\,Cosh(\mu) = \lambda_0 + \frac{1}{\lambda_0} \tag{1.17}$$

The sum of the eigenvalues is equal to the trace of the matrix, where the trace is defined as the sum of the elements residing on the principle diagonal. The trace is invariant under a change of basis, allowing equation 1.18 to be written (for the mono-coupled system).

$$Cosh(\mu) = \frac{T_{11} + T_{22}}{2} \tag{1.18}$$

Evaluating eq. 1.18 yields an identical expression to eq. 1.7, demonstrating the equivalence of the two methods.

An important conclusion for this thesis in particular, which has been reached relatively recently, concerns the validity of the transfer matrix approach, and more generally Floquet-Bloch theory for finite systems, or systems with few periods. Griffiths, Pererya and Hussein [14]–[17] all produced results that showed the frequency band structure was consistent for both finite and infinite system, showing that structures with as few as two cells can exhibit a band structure [16]. Griffiths [14] presented a pedagogical paper in order to collect together cross-discipline literature and current understanding of waves in locally periodic structures as well as finite periodic structures. This terminology is depicted graphically in Figure 1.5.

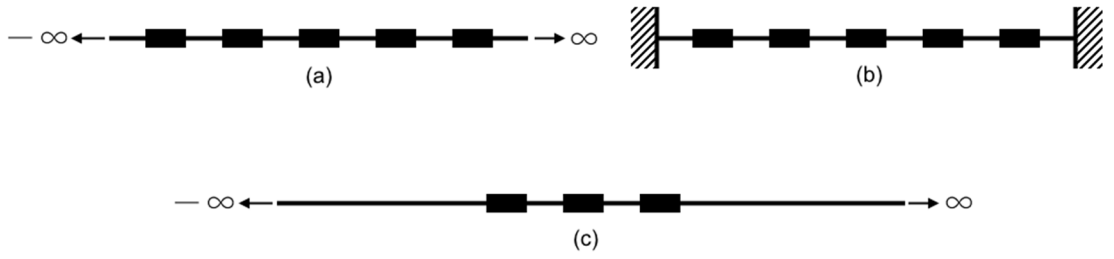

Figure 1.5 (a) An infinite periodic structure. (b) a finite periodic structure. (c) a locally periodic structure.

The majority of the paper refers to the field of quantum mechanics and focuses on locally periodic structures. These are infinite systems where the periodic discontinuities are localized (Figure 1.5c), the dispersion however is still continuous. Griffiths elucidates the nature of truly finite periodic structures, that is, with conservative boundary conditions. These have discrete 'bound states' in the quantum case or standing waves in the case of mechanical waves, rather than a continuous dispersion spectrum from 'scattering' or travelling waves. Using Schrödinger's equation as an example, the structure of the transfer matrix was detailed. It was then shown how substitution of the boundary conditions leads to a condition to be solved for the allowable energy states. In the case of a mechanical system these correspond to the eigenfrequencies. Griffiths presents a recurrence relation used to represent N cells from the single cell transfer matrix, with no reference to Floquet-Bloch theory, thus valid for any length of periodic array. A simple closed form expression for the transmission coefficient of locally periodic systems is shown and examples provided.

Pereyra [15] presented a method applied to locally periodic solid-state problems utilising the TM in a similar way to Griffiths. Pereyra elucidates details about the structure of the transfer matrix and its recursion relation. Pereyra's sequel [18], [19] aimed to provide analytical expressions for the eigenvalues and eigenfunctions of real finite periodic systems with arbitrary cell potential. Analytical expressions for the wavefunction and resonant energy (eigenfunctions and eigenvalues) of bounded and quasi-bounded periodic systems governed by Schrödinger's equation. This is analogous and can be adapted to all systems governed by the wave equation. It was shown that for finite periodic systems the Bloch function property is inaccurate. Properties of the resonant states and eigenfunctions were described.

1.2.2 Localization in Periodic Structures

The entirety of this thesis is focussed on exploiting the phenomena associated with localization. The term 'localization' is used in different ways, even in closely related fields, and the terminology is often confused. It is therefore fitting to begin with a brief orientation into the use within this work.

The study of localization in linear periodic arrays stretches across many disciplines. The first treatise, however, began in the field of solid-state physics with P.W. Anderson,

whom received the Nobel Prize in physics in 1977, partly for his work on the topic [20]. There are also fascinating localization phenomena that are exclusive to non-linear periodic structures, such as intrinsic localized modes (ILM's) and discrete breathers [21], which no doubt can, and will, be exploited for engineering gain at some point in the future. This thesis however focuses on the purely linear phenomena of local resonances and localized modes. To begin, the subtle difference between these two similar, yet distinct, phenomena will be defined:

- *Local resonance*: a local resonance occurs due to spatially localized forcing at a frequency within the stop-band of the array. When excited at a stop-band frequency, waves cannot propagate away from the source of the excitation. The surrounding array effectively acts as a non-dissipative boundary condition, hence the energy is trapped in the excitation region. A local resonance is therefore not a mode of the periodic structure *as a whole,* but modal behaviour of a subsection of the array.
- *Localized Mode*: a localized mode is induced by the introduction of a disorder into the array. The modes of a perfectly periodic system all reside within the pass-band. Once a disorder is introduced, a mode of the *whole structure* moves into the stop-band of the array (Figure 1.6). This is the phenomenon described by Anderson and is known either eponymously or as 'strong' localization.

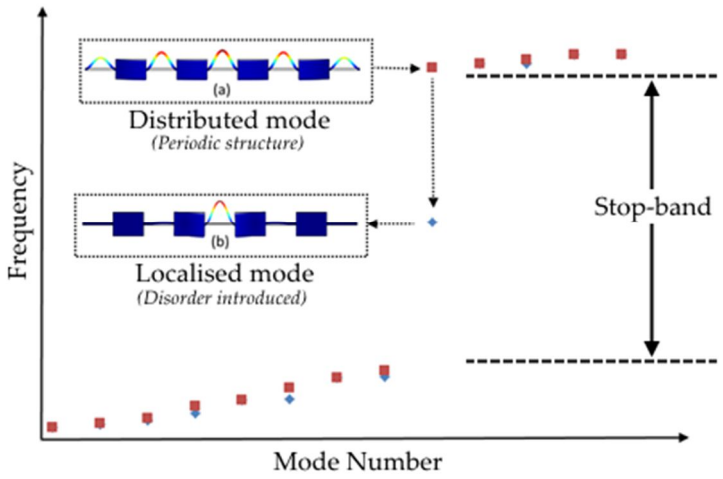

Figure 1.6 The frequency space behaviour of mode localization. When a disorder is introduced into the perfectly periodic example structure of a 'stepped-beam' the mode is localized and moved to a frequency within the stop band. In this example the disorder has been introduced as a perturbation to the thickness of the central slender beam.

Although visually the difference may seem trivial, it becomes non-trivial when one wants to either simulate or exploit either effect. Two examples which demonstrate this are: (1) a local resonance must be excited by a spatially localized force, whereas a localized mode is indiscriminate of forcing location and (2) localized modes can be found through modal analysis of the homogeneous equations of the structure, but a local resonance is found only through a specific forced case.

1.2.3 Mode Localization Sensors

Mode localization refers to the spatial trapping of energy in a coupled oscillatory system that occurs when a disorder is introduced into a previously ordered system. In the structures of interest to this thesis this is manifested as a dramatic change in the mode shapes. This was first suggested as a novel sense protocol in references [1], [2] and coined 'mode localization sensing'. The sense mechanism was initially proposed as an alternative to measuring frequency-shift, and therefore this method has been used as a benchmark for comparison [2], [3], [22].

Mode localization sensors have been approached primarily in the case of two weakly coupled symmetrical oscillators rather than periodic systems. They exploit the large change in the eigenvector that occurs when the symmetry is broken. A simplified model of a mode localization mass sensor is presented in Figure 1.7. The identical resonators are coupled by the weak spring of strength k_c. In the case when $\Delta m = 0$ the system exhibits both in-phase and out-of-phase modes with equal distribution of displacement amplitude. As is commonly known, the in-phase mode is the fundamental and the out-of-phase occurs at a higher frequency. When $\Delta m \neq 0$ the modal amplitude distribution is weighted unevenly, favouring the lower or higher frequency resonators, in the in-phase and out-of-phase modes respectively. That is, if the system is vibrating in its fundamental mode, and a mass is added to one resonator, this resonator will experience a much larger displacement relative to the other resonator. In the second mode however, the un-laden resonator will exhibit the larger relative displacement. The sensors are proposed to operate in one mode and use the ratio of the amplitude of the resonators to detect the size of the added mass.

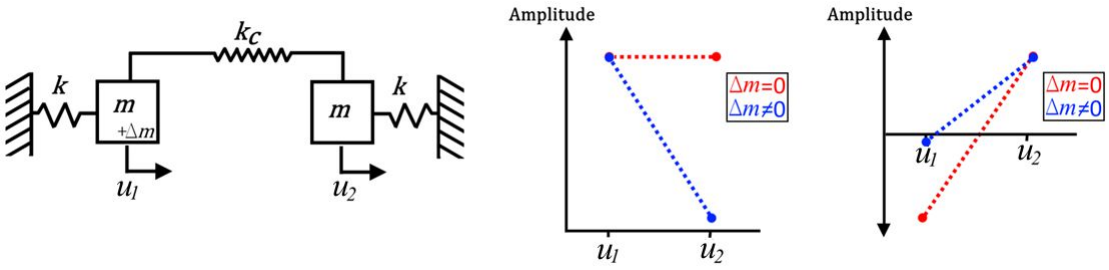

Figure 1.7 Illustrative example of the principles of mode localization sensing

The mass-spring systems can take a variety of physical forms. A commonly proposed geometry in the literature is two cantilever beams with small coupling overhang [2], [3], [22]. Other geometries have been proposed that exploit electrostatic coupling. These include ring resonators, free-free beams and double-ended tuning fork (DETF) resonators.

The effect and the dependence of the coupling strength is shown clearly using a simple eigenvalue perturbation method. Using the example system in Figure 1.7, the non-dimensionalised equations of motion for the system can be posed as an eigenvalue problem (EVP) by, assuming harmonic motion [2] .

$$\left(\mathbf{K} - \lambda(\mathbf{M} + \boldsymbol{\delta}\mathbf{M})\right)\underline{u} = 0 \tag{1.19}$$

$$\mathbf{K} = \begin{pmatrix} 1+\kappa & -\kappa \\ -\kappa & 1+\kappa \end{pmatrix} \tag{1.20}$$

$$\mathbf{M} = \begin{pmatrix} 1 & 0 \\ 0 & 1 \end{pmatrix} \tag{1.21}$$

$$\boldsymbol{\delta}\mathbf{M} = \begin{pmatrix} 0 & 0 \\ 0 & \delta \end{pmatrix} \tag{1.22}$$

$$\delta = \frac{\Delta m}{m} \tag{1.23}$$

$$\kappa = \frac{k_c}{k} \tag{1.24}$$

If $\Delta m = 0$, the normalised, unperturbed eigenstates of the symmetrical system can be found to be those given in eqs. 1.25-28.

$$\lambda_0{}^{(1)} = 1 \qquad (1.25)$$

$$u_0^{(1)} = \frac{1}{\sqrt{2}}\begin{Bmatrix}1\\1\end{Bmatrix} \qquad (1.26)$$

$$\lambda_0{}^{(2)} = 2\kappa + 1 \qquad (1.27)$$

$$u_0^{(2)} = \frac{1}{\sqrt{2}}\begin{Bmatrix}1\\-1\end{Bmatrix} \qquad (1.28)$$

If $\Delta m \ll \kappa$, an eigenvalue perturbation method can be used to obtain the solution to perturbed equation 1.19. Using the unperturbed solution, the perturbed eigenvalues and vectors can be defined by equations 1.29 and 1.30 respectively [23].

$$\lambda_p^{(i)} = \lambda_0^{(i)} + u_0^{(i)^{\mathrm{T}}} \cdot \left(\boldsymbol{\delta K} - \lambda_0^{(i)} \boldsymbol{\delta M}\right) \cdot u_0^{(i)} \qquad (1.29)$$

$$u_p^{(i)} = u_0^{(i)} \cdot \left(1 - \frac{1}{2} u_0^{(i)\mathrm{T}} \cdot \boldsymbol{\delta M} \cdot u_0^{(i)}\right) + \sum_{\substack{j=1 \\ j \neq i}}^{2} \frac{u_0^{(j)^{\mathrm{T}}} \cdot \left(\boldsymbol{\delta K} - \lambda_0^{(i)} \boldsymbol{\delta M}\right) \cdot u_0^{(i)}}{\lambda_0^{(i)} - \lambda_0^{(j)}} \cdot u_0^{(j)} \qquad (1.30)$$

Using equations 1.29 and 1.30 the relative change in the eigenstate (mode shape) and eigenvalue (square of the resonant frequency) have been found to be as given in equations 1.31-32 [24].

$$\frac{\lambda_p^{(i)} - \lambda_0^{(i)}}{\lambda_0^{(i)}} = \frac{-\delta}{2} \qquad (1.31)$$

$$\frac{\left|u_p^{(i)} - u_0^{(i)}\right|}{\left|u_0^{(i)}\right|} = \left(\frac{1}{4} + \frac{1}{4\kappa}\right)\delta \qquad (1.32)$$

Equation 1.32 describes the sense protocol of mode-localization. It can be seen that decreasing the coupling strength, κ, can amplify the response to a fixed change in mass, δ. This result has drawn the interest of many researchers to see if mode localization presents a viable new sense paradigm to compete with other MEMS sense technologies.

Mode localization sensors have been shown to possess potentially advantageous properties when compared with the commonly used frequency-shift sensors. The most prominent of these is the potential improvement in sensitivity; theoretically orders of magnitude better than the aforementioned frequency-shift alternative [2]. In addition, the sensors benefit from common mode rejection, that is, changes in the environment

or ambient conditions that affect both resonators, will not affect the measurement. This is a distinct advantage over frequency-shift measurement and is important for countering drift and false measurements.

The vast majority of explorations into the exploitation of mode localization have been in the context of the development of ultra-sensitive mass sensors. These put particular emphasis upon targeting bio-molecules, to facilitate the realisation of low-cost, effective medical diagnostic devices. The origins of the idea of exploiting mode localization for sensing means can be attributed to Nicu and Bergaud [1]. A discretized model was used to represent a double-ended tuning fork resonator and operation as a bio-mass sensor was demonstrated using the theoretical results. The conditions for the avoidance of nonlinearity were considered, the response was shown to be governed by Duffing's equation; however, this analysis was specific to the case of the double ended tuning fork.

The sense concept was given further consideration by Spletzer *et al.* [2], whom presented the first experimental evidence of operation. The article introduced the method of using coupled cantilevers for mass detection. Experimental validation was sought for the predictions of an eigenvalue perturbation method applied to a discretised system of two coupled resonators. The study highlighted the most attractive features of the sense method: a high-sensitivity that is independent of quality factor and intrinsic common mode rejection, making the device less susceptible to drift and false readings due to changes in the ambient environment. It was highlighted that these features were achieved prior to any in-depth optimisation of the geometry.

Thiruvenkatanathan *et al.* investigated similar systems, but focused attention upon the effect of the coupling strength on the sensitivity [3], [25]. It was shown that ensuring weak coupling is vital to enabling high sensitivity. This lead to the investigation of various electrostatically coupled high-Q geometries. These were shown to be capable of decreasing the coupling strength beyond that of a direct mechanical coupling, leading to a potential further increase in sensitivity.

The investigation into the effect of the coupling strength drew attention to the limits imposed upon the maximum sensitivity of such devices. The limits occur primarily due

to the well-documented phenomenon of eigenvalue loci-veering [26] – and the subsequent bandwidth considerations – as well as the limits of the noise within the system. This was analysed in detail in reference [27]. The analysis yielded a fundamental limit on the resolution of this two-degree-of-freedom class of mode localization sensors. Similar investigations into the noise sensitivity of coupled microcantilever arrays has been conducted more recently by Ryan *et al.* [28], [29].

DeMartini *et al.* [30] highlighted the superior ability of coupled resonators arrays for multiple analyte detection, when compared to un-coupled arrays. Arrays of functionalised un-coupled arrays, although capable of detecting multiple analytes, require greater signal processing ancillaries, whereas a coupled resonator system can function as a single input-single output device. A complex topology using four micro-beam resonators attached to a shuttle mass was modelled using an equivalent lumped parameter system. The novel sense method used four separate localized modes and detected the frequency shift of the modes via analysis of the frequency response of the shuttle mass. The sense method was applied to a coupled cantilever geometry in reference [31].

One of the major inhibitors to the implementation of this class of devices is the sensitivity to the presence of a fabrication imperfection. The imperfections can induce localization and thus impose a limit on the potential size and resolution of the devices. This problem was addressed in a novel way by Gil-Santos *et al.* [32]. The study proposed the use of thermomechanical noise as a means of excitation of nanomechanical cantilevers – previous studies involving cantilevers had all employed piezoelectric base excitation, which is poor at exciting the anti-symmetric mode. It was shown that this transduction scheme eliminates the requirement for the initial disorder to be zero as well as not requiring any excitation circuitry. The former potentially enables a dramatic improvement in the potential device resolution.

Pakdast and Lazzarino [33] investigated the use of three coupled cantilevers for mass detection. The geometry was shown to be less sensitive to surface stress than the two coupled cantilever system, as well as allowing the possibility to determine which cantilever the mass had adsorbed to. Other extensions of note include Chopard *et al.* [34], who proposed the use of piezoelectric transduction.

The extension to systems of higher degrees of freedom was suggested by Spletzer *et al.* [2]. It was noted that the extension to a large array of cantilevers could enable multiple analyte detection. This was expanded upon by the same author in reference [22] in which a system of fifteen coupled microcantilevers were analysed using a similar procedure. The investigation revealed that the addition of mass to each cantilever will produce a unique eigenmode shift. Indicating that the location of the analyte can be deduced from the pattern of eigenmode shifts. It was suggested that this could enable simultaneous multi-analyte detection. In addition, and of critical importance in the context of this body of work, the sensitivity to the addition of a mass was improved by an order of magnitude over the previously analysed two-cantilever system.

Zalalutdinov *et al.* [35] manufactured a 2D lattice of nanomechanical paddle resonators to investigate the suppression of the intrinsic localization due to a manufacturing disorder. It was sought to answer the question of whether extended modes could be realised in large arrays. It was found that the extended modes could be realised, with participation from all resonators. It was suggested that the results are of relevance to signal processing and sensing applications.

1.3 Open questions

The following chapters each aim to answer a specific question that is currently unanswered in the literature. The specific open questions corresponding to each chapter that this thesis aims to answer are enumerated below.

1. *How does using a periodic array as a coupler affect or enhance the operation of a mode localization sensor?*

   Chapter 2 looks to a simplified model of the proposed device, paying particular attention to the novel coupling method. The models used are of a similar type to those present in the literature, aiming to allow direct comparison.
2. *Can a mode localization sensor be constructed using SAW?*

   The overt assumption in beginning this work is that such a sense mechanism can be transferred to a SAW architecture. Evidence towards this assumption is provided in the modelling work carried out to produce chapter 3.

3. *What benefits are afforded by using the SAW platform and how can they be best exploited?*

   The analysis presented in chapter 4 looks specifically at the model derived to describe the SAW system, aiming to answer the question posed.

4. *What limits are imposed on such a device by loss mechanisms and thermal noise contributions?*

   Chapter 5 intends to tackle this question, examining the feasibility of the proposed device in the presence of the limiting factors it will face in operation.

5. *Does the SAW mode localization sensor present a viable platform to construct a competitive MEMS magnetometer?*

   The theoretical conclusions on device performance are posed in terms of the field of MEMS magnetometers in chapter 6. This application is employed as a yardstick to test the impact of the proposed device on current problems in the field of MEMS sensing.

Chapter 2. Theory and Principles of Operation

2.1 Introduction

Within this chapter the principles of the proposed novel sensor are described using simplified discretized models. This aligns with the majority of the analysis available in the literature and facilitates comparison between similar proposed devices. The novelty of the device presented here is twofold; firstly, the use of a periodic coupling array, and secondly the use of SAW, to be addressed in more depth in following chapters. The purpose of this chapter is to introduce the device and present simplified models to gain insight and intuition into the operation.

The device is an extension of the 'mode localization sensor' that has been introduced recently in the literature, and is reviewed in depth in the opening chapter. This chapter begins by introducing the extensions proposed by this thesis, namely, the introduction of a periodic array as a coupler and the use of a SAW architecture. These are discussed in section 2.3. Two models will be used in combination to describe the mode of operation and performance. A lumped parameter model is introduced as a means of gleaning insight and intuition into the expected device behaviour. The system matrices are presented in a non-dimensional form alongside an approximate 2-DOF representation. The 2-DOF model allows for more straightforward analytical interrogation. The eigenvalues and eigenvectors are found both numerically and analytically. The proposed operation of the device is described qualitatively using the LPM models. In addition, selective forcing, the behaviour of the eigenvalues and device sensitivity are discussed separately, before conclusions are drawn.

2.3 The SAW mode localization sensor

One of the primary thrusts of the present work is to investigate the utility and potential benefit of a finite periodic array coupling the two DOFs of the mode localization sensor. It was indicated in the opening chapter that periodic structures possess a stop band, a region in frequency space in which energy cannot be transferred across it. In a finite periodic array the amount of energy that can be transmitted in the stop band is proportional to the number of periods in the array. A common result from the literature

on mode localization sensing is the need for weak coupling; a periodic array presents a means of achieving weak coupling for a multitude of sensor geometries. It is proposed here to utilise a SAW architecture. The use of SAW presents many advantages when compared to the alternative of constructing periodic arrays of suspended MEMS. The SAW devices require a simple and inherently robust architecture; there are no deep cavity etches or slender beams. The manufacturing process is well established and SAW resonators are commonplace in microelectronics. Therefore, the use of SAW presents a favourable platform to introduce a novel sense protocol. The author introduced the concept of a SAW mode localization sensor in references [36], [37] which, to the authors' knowledge are the first examples available in the literature.

The proposed configuration consists of two cavities, coupled by an N-period reflective array. The arrays are constructed from a patterned metal film deposited on a piezoelectric substrate. In the general case, excitation can occur in either cavity, or both cavities. Regardless of the excitation method, one cavity is deemed the reference, and the other the sense, cavity. The coupling strength between the two cavities is governed by the shared periodic reflector, deemed the 'coupling array'. The basic arrangement is depicted in Figure 2.1.

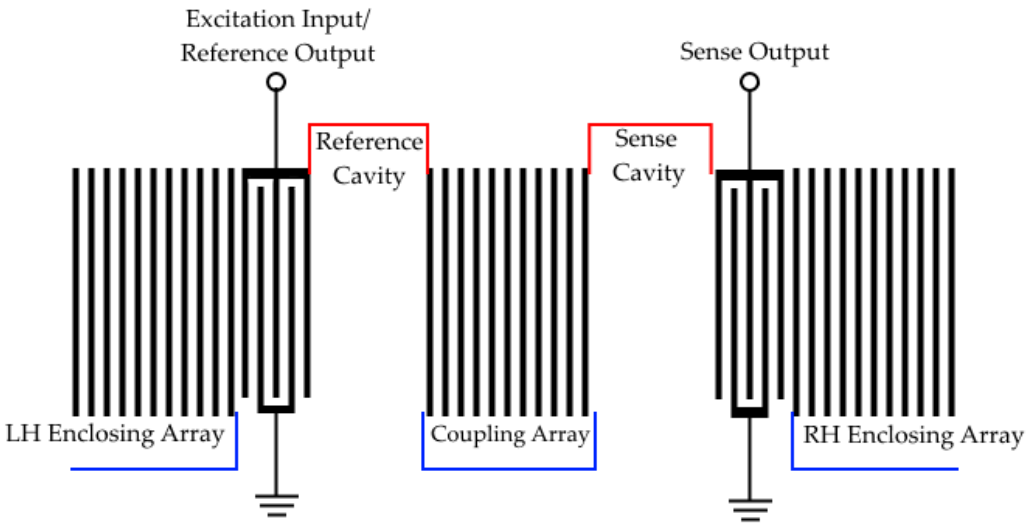

Figure 2.1 Schematic of basic SAW device geometry. The enclosing arrays act to bound the geometry working as quasi-hard boundary conditions. A mode is excited between the enclosing arrays by excitation in the reference cavity. The relative displacement amplitude of the sense cavity with respect to the reference cavity is used as the sensor output. The input can be any physical phenomenon that perturbs the surface wave speed within the sense cavity e.g. mass adsorption or magnetostrictive stiffening.

The output of the device is the ratio of the sense cavity displacement amplitude to the reference cavity displacement amplitude, or the inverse. The theory of operation is that this output responds in proportion to a break in the symmetry of the two cavities, directly analogous to the mode localization sensors described in section 1.1. A perturbation of the wave-speed in the sense cavity will be induced to break the symmetry. Causing an output response in proportion to the perturbation size and the coupling strength.

2.4 Lumped parameter model

A representative lumped parameter model (LPM) is introduced to give an initial assessment of the device behaviour. This will also allow direct comparison to the results presented in the literature, which are consistently modelled using LPMs. The LPM consists of two monatomic lattices coupled by a partially anchored diatomic lattice. This is shown schematically in Figure 2.2. A system of this kind can be found to be equivalent by posing the problem on a string and deriving the finite difference equations.

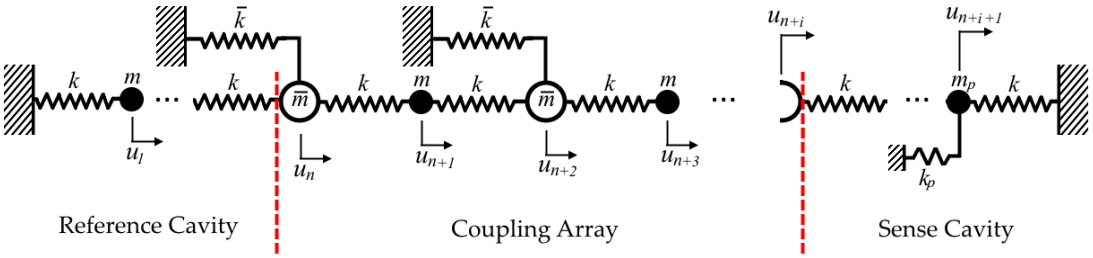

Figure 2.2 Schematic of LPM representation

The lattice consists of both anchored and free masses, each representing different regions of the SAW system described by Figure 2.1. The free masses represent a region of un-plated substrate, such as the cavities. The anchored masses represent a plated region, such as the IDT fingers or reflectors. The anchor spring and perturbed mass, $\overline{k}$ and $\overline{m}$, represent the stiffness perturbation and mass loading due to the plate respectively. The model excludes the enclosing cavities and replaces these with hard boundary conditions. This is the artificial boundary of the device, in the SAW device, any wave propagation past this point is regarded as loss.

2.4.1 System matrices

Applying Newton's second law to the schematic of Figure 2.2, with 1 DOF assigned per cavity, leads to the system matrices and equation of motion described in equations 2.1-2.3.

$$\mathbf{M}\underline{\ddot{u}} + \mathbf{K}\underline{u} = \underline{F} \tag{2.1}$$

$$\mathbf{M} = \begin{bmatrix} m & & & & & \\ & \overline{m} & & & & \\ & & m & & & \\ & & & . & & \\ & & & & \overline{m} & \\ & & & & & m_p \end{bmatrix} \tag{2.2}$$

$$\mathbf{K} = \begin{bmatrix} 2k & -k & & & \\ -k & \overline{k} + 2k & -k & & \\ & -k & 2k & -k & \\ & & & . & \\ & & & -k & k_p + k \end{bmatrix} \tag{2.3}$$

It is useful to reduce the variables by non-dimensionalising the system matrices. It was chosen to normalise to the 'substrate' mass and stiffness, m and k. After normalisation, setting $\underline{F} = \underline{0}$ and assuming time harmonicity at angular frequency ω produces an EVP in a non-dimensional form. In this case the eigenvalues are non-dimensionalised by the natural frequency of the one 'substrate element', if it were uncoupled. The EVP is shown in non-dimensional form in equations 2.4-2.11.

$$\left|\widetilde{\mathbf{M}}^{-1}\widetilde{\mathbf{K}} - \lambda_0\mathbf{I}\right| = 0 \tag{2.4}$$

$$\widetilde{\mathbf{M}} = \begin{bmatrix} 1 & & & & & \\ & \widetilde{m} & & & & \\ & & 1 & & & \\ & & & . & & \\ & & & & \widetilde{m} & \\ & & & & & \widetilde{m_p} \end{bmatrix} \tag{2.5}$$

$$\tilde{\mathbf{K}} = \begin{bmatrix} 2 & -1 & & & \\ -1 & \tilde{k}+2 & -1 & & \\ & -1 & 2 & -1 & \\ & & & \cdot & \\ & & & -1 & \widetilde{k_p}+1 \end{bmatrix} \tag{2.6}$$

$$\omega_n = \sqrt{\frac{k}{m}} \tag{2.7}$$

$$\tilde{m} = \frac{\overline{m}}{m} \tag{2.8}$$

$$\widetilde{m_p} = \frac{m_p}{m} \tag{2.9}$$

$$\tilde{k} = \frac{\overline{k}}{k} \tag{2.10}$$

$$\widetilde{k_p} = \frac{k_p}{k} \tag{2.11}$$

2.4.2 Approximate 2-DOF Representation

An approximate alternative representation of the LPM is presented to enable the behaviour to be investigated analytically. The system is modelled as having 2-DOFs, each cavity represented as a single DOF, with the periodic array represented using an equivalent cross receptance. A receptance is defined as a force per unit displacement. The idea of using receptances for periodic structures was exploited heavily by Mead in references [8]–[12]. This model discards information about the displacements of the intermediate DOFs and therefore all the non-localized modes. Figure 2.3 shows a schematic of the model.

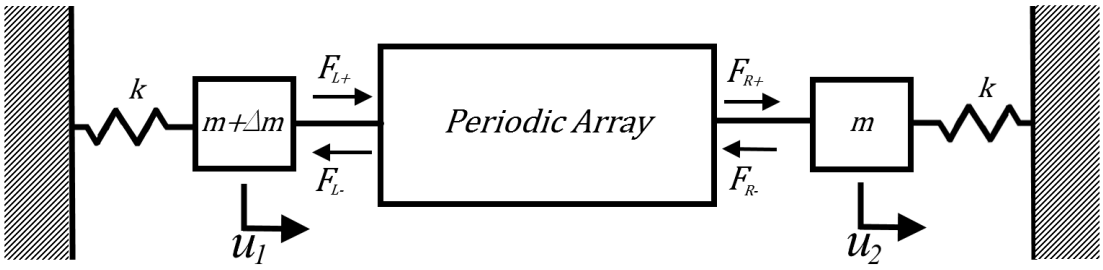

Figure 2.3 Schematic of approximate device representation

The periodic structure separating the two resonators is assumed to have sufficient periods such that Floquet-Bloch theorem can be assumed valid. In addition, one-way coupling into the periodic array is assumed for the force waves originating at either the left or the right hand end. This assumption states that a force originating at the LH

or RH boundary propagates away from the boundary into the periodic array with negligible reflection at the localized mass-periodic array boundary. Additionally, reflections from within the periodic array are assumed sufficiently weak by the time they reach the end boundary, and therefore can be neglected. Due to these assumptions, there are two separate force relations, one for forwards travelling waves originating at the LH boundary and one for rearwards travelling waves originating at the RH boundary. These are given in equations 2.12 and 2.13 respectively.

$$F_{R+} = e^{N\mu} F_{L+} \tag{2.12}$$

$$F_{L-} = e^{N\mu} F_{R-} \tag{2.13}$$

N is the number of periods within the periodic array and μ is the frequency dependent propagation constant. μ is a function of the elements of the receptance matrix, calculated for a single period of the array.

To find the forwards travelling wave originating at the left-hand end (LHE), the equilibrium requirements at u_1 must be considered, whilst ignoring the contribution of F_{L-}. An identical procedure can be considered at x_2 for the rearwards travelling wave. With reference to Figure 2.3 it can be seen that the forces F_{L+} and F_{R-} are as shown in equations 2.14 and 2.15.

$$F_{L+} = k\, u_1 \tag{2.14}$$

$$F_{R-} = k\, u_2 \tag{2.15}$$

Combining the relationships shown in equations 2.12-2.15, the force on one mass due to a displacement at the other can be found. These are shown explicitly in equations 2.16 and 2.17.

$$F_{L-} = k\, e^{N\mu}\, u_2 \tag{2.16}$$

$$F_{R+} = k\, e^{N\mu}\, u_1 \tag{2.17}$$

The preceding derivation has effectively calculated the equivalent cross receptance, α_c, for the periodic array, as given explicitly in equation 2.18.

$$\alpha_c = \frac{1}{k e^{N\mu}} \tag{2.18}$$

The equation of motion for the 2-DOF system can now be written. This is shown in equations 2.19-2.22.

$$[\mathbf{K} - \omega^2 \mathbf{M}] \begin{Bmatrix} u_1 \\ u_2 \end{Bmatrix} = 0 \tag{2.19}$$

$$\mathbf{M} = \begin{bmatrix} 1+\delta & 0 \\ 0 & 1 \end{bmatrix} \quad (2.20) \qquad \mathbf{K} = \begin{bmatrix} 1 & e^{N\mu} \\ e^{N\mu} & 1 \end{bmatrix} \quad (2.21) \qquad \delta = \frac{\Delta m}{m} \tag{2.22}$$

The eigenvalues and eigenvectors of the system are shown in equations 2.23-2.27.

$$\omega_1{}^2 = \frac{2+\delta-\varsigma}{2(1+\delta)} \tag{2.23}$$

$$\underline{u_0}^{(1)} = \begin{Bmatrix} -\dfrac{e^{-N\mu}(\delta+\varsigma)}{2(1+\delta)} \\ 1 \end{Bmatrix} \tag{2.24}$$

$$\omega_2{}^2 = \frac{2+\delta+\varsigma}{2(1+\delta)} \tag{2.25}$$

$$\underline{u_0}^{(2)} = \begin{Bmatrix} -\dfrac{e^{-N\mu}(\delta-\varsigma)}{2(1+\delta)} \\ 1 \end{Bmatrix} \tag{2.26}$$

$$\varsigma = \sqrt{4e^{2N\mu} + 4e^{2N\mu}\delta + \delta^2} \tag{2.27}$$

The propagation constant for the anchored diatomic lattice can be found using the method outlined in section 1.2 of the previous chapter. The unit cell is displayed in Figure 2.4 and the equations of motion for the masses are given in equations 2.28 and 2.29.

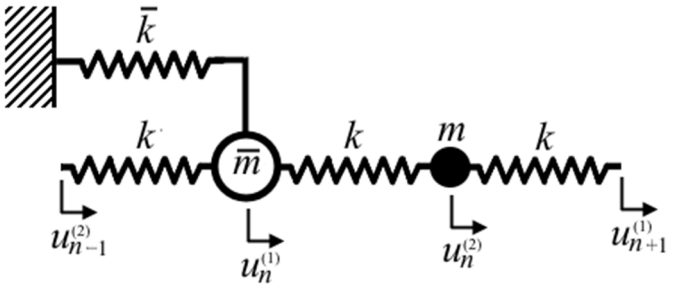

Figure 2.4 Unit cell of periodic coupling array

$$\bar{m}\ddot{u}_n^{(1)} = -k\left(u_n^{(1)} - u_{n-1}^{(2)}\right) - k\left(u_n^{(1)} - u_n^{(2)}\right) - \bar{k}u_n^{(1)} \tag{2.28}$$

$$m\ddot{u}_n^{(2)} = -k\left(u_n^{(2)} - u_n^{(1)}\right) - k\left(u_n^{(2)} - u_{n+1}^{(1)}\right) \tag{2.29}$$

After asserting a Bloch type solution and time harmonicity, these equations of motion can be presented in matrix form. The determinant of the resulting 2x2 matrix is set equal to zero and rearranged for the propagation constant. This is given in equation 2.30.

$$\mu = \frac{2k^2 + 2k\left(\bar{k} - m\omega^2\right) - \left(\bar{k}m + 2k\bar{m}\right)\omega^2 + m\bar{m}\omega^4}{2k^2} \tag{2.30}$$

2.5 Discussion

2.5.1 Frequency Response

The models outlined in the previous sections can be used in unison to give an informative qualitative description of the devices behaviour in frequency space. From which the modal behaviour can be inferred and subsequently confirmed by solving the numerical EVP.

Initially the symmetric condition will be addressed, a representative plot of the mode distribution in frequency space is given in Figure 2.5 for a system with 30 coupling DOFs and 4 DOFs per cavity.

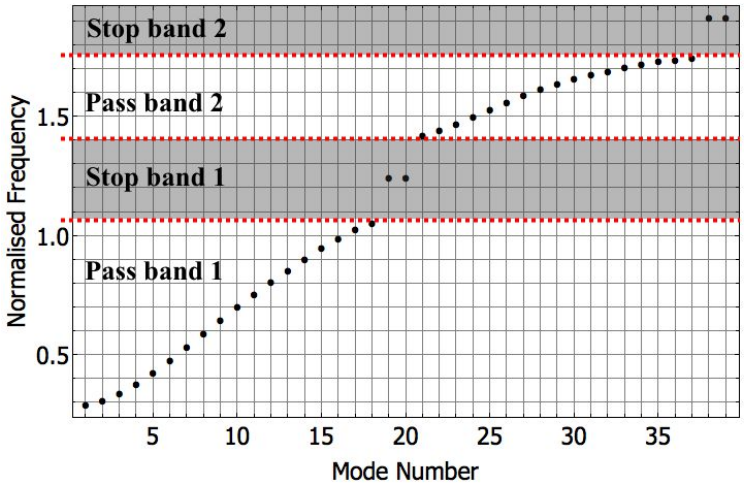

Figure 2.5 Modal distribution in frequency space showing pass and stop bands

The location of the pass and stop bands have been indicated on the plot, it can be seen that two stop bands exist and the majority of the modes are clustered into the pass bands. Two 'localized' modes exist in the central stop band. In the special case where the cavities are matched to the coupling array, all modes exist within the pass band. The effect of increasing the length of the cavities is depicted in Figure 2.6. The cavity length can be used to tune the location of the modes in the stop band.

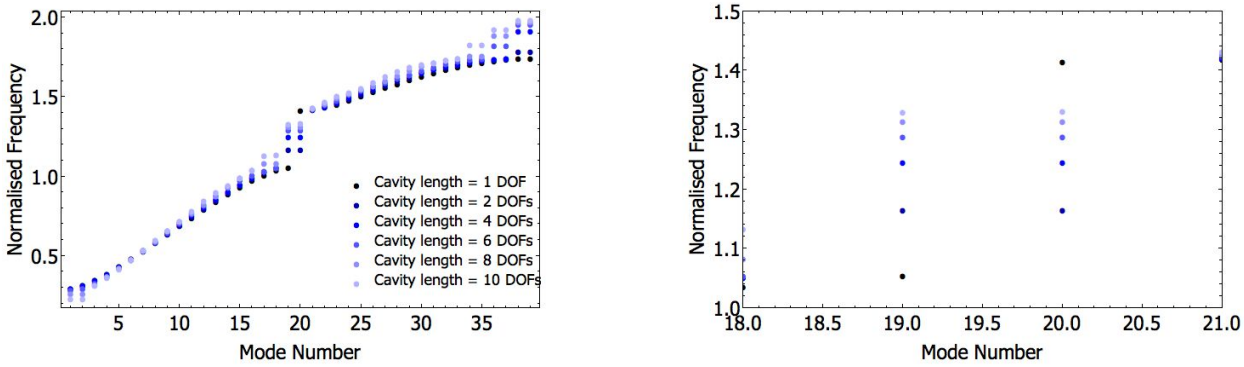

Figure 2.6 Effect of cavity length on modal distribution

The relationship between the system as a whole and dispersion spectrum of the coupling array can be seen more clearly by overlaying the modal distribution on the dispersion spectrum. An example of this is given in Figure 2.7, where the attenuation coefficient, $Re(\mu)$, is plotted against frequency.

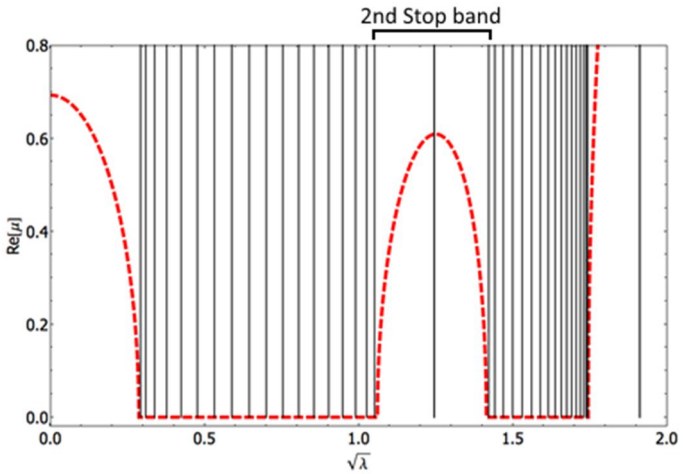

Figure 2.7 Mode distribution plotted with coupling array dispersion

This plot configuration is very useful for the current analysis as it provides the modal behaviour and one can also interpret the forced response. If the structure were to be excited at a frequency within a stop band, the energy is trapped at the forcing location and a local resonance will occur. The strength of the localization can be quantified by the attenuation constant. This is the imaginary part of the complex wavenumber, thus an increase in this leads to faster spatial attenuation and a sharper, more localized resonance. It is clear that the sharpest local resonance will appear when the excitation frequency resides in the centre of the stop band.

The dispersion spectrum and modal distribution will distort as the parameters of the coupling array are varied. The stop band of interest for the current analysis is the stop band residing just above a normalized frequency of unity, corresponding to the primary $\frac{\lambda}{2}$ stop band. The stop band limits, and their dependence on the array parameters, can be found by considering the propagation constant expression (eq. 2.31). In the pass bands the solution is purely imaginary, the inverse hyperbolic function ArcCosh, appearing in the propagation constant definition of eq. 1.7, is purely imaginary when its argument is real and within the range -1 to 1. Thus, the argument is set equal to both -1 and 1 and the roots of ω found. After neglecting solutions for which $\omega < 0$, four solutions are yielded which correspond to the upper and lower limits of the pass bands. The two positive solutions for $\arg(\mu) = -1$ are the limits of the stop band of interest. These are given in equations 2.31 and 2.32.

$$\omega_{L1} = \sqrt{\frac{2k}{m}} \tag{2.31}$$

$$\omega_{L2} = \sqrt{\frac{2k + \overline{k}}{\overline{m}}} \tag{2.32}$$

It can be seen that these are the natural frequencies of the two degrees of freedom, if they were uncoupled. Therefore, if the parameters are chosen such that $\omega_{L1} = \omega_{L2}$, then the stop band does not exist. Furthermore, in the case plotted in Figure 2.7, ω_{L2} is the lower limit of the stop band; however it is possible to reverse this by increasing the stiffness, $\overline{k}$ or reducing the mass, $\overline{m}$ sufficiently, or indeed a combination of the two. Increasing the width of the stop band also has an effect on the size of its peak. Considering again the case plotted in Figure 2.7, the effect of steadily increasing $\overline{m}$ is shown in Figure 2.8. It is of note that the modal frequencies will always remain bound within their pass band or stop band, no matter how the parameters within the array are varied.

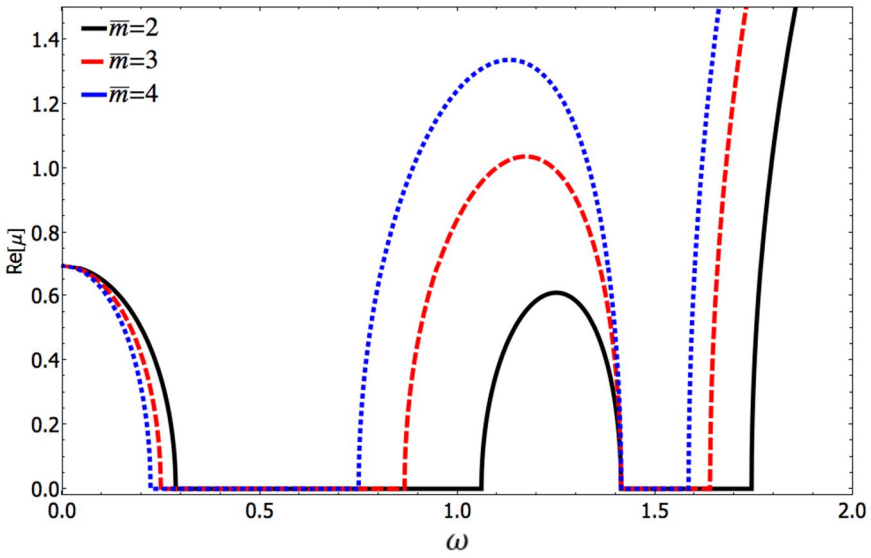

Figure 2.8 Example of effect of array parameters on dispersion

For the present description of the device the coupling array parameters are fixed arbitrarily. The only assumptions adhered to are that the coupling array is weakly anchored ($\overline{k} \ll k$) and that $\overline{m} > m$, this ensures that the limit ω_{L2} remains as the lower limit. More detail on how the parameters will be chosen for the SAW device are

elaborated in the following chapters. The localized modes within the pass band in Figure 2.7 are analogous to the two modes of the 2-DOF resonators described in previous mode localization sensor literature and addressed in chapter 1. These are plotted in Figure 2.9, demonstrating that the modes differ only by the phase shift between the cavities, as with the 2-DOF example systems.

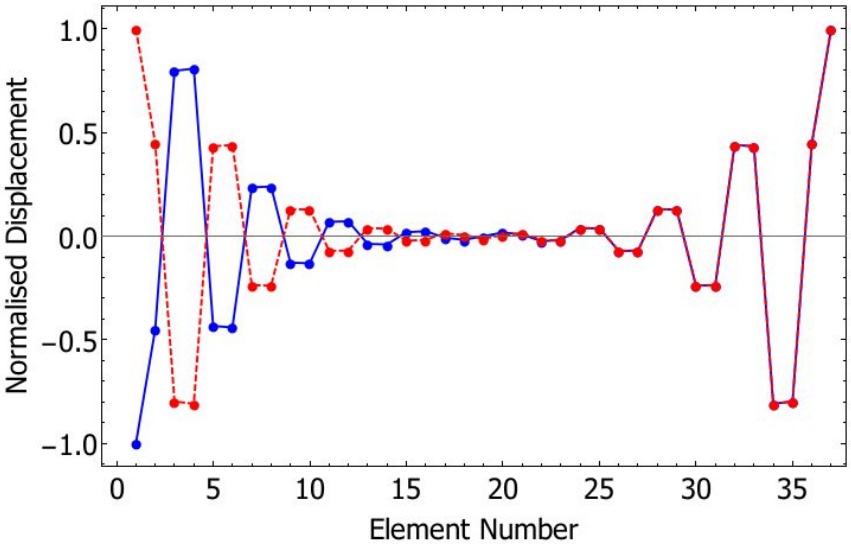

Figure 2.9 Localized modes

2.5.2 Qualitative overview of device operation

The previous section summarised the general behaviour of the system. Within this section, the means of operation will be discussed. The operation is analogous to the mode localization devices previously described. One mode will be excited and the change in the amplitude ratio, due to an induced asymmetry, will be sensed. This will be referred to as 'mode-tracked' operation. Methods of achieving this in practise include the use of a phase locked loop (PLL), a control system sensing and correcting for changes in the response phase. This will also correct for frequency drift due to ambient effects such as temperature fluctuations. The desired response can therefore be found by computing the change in the mode shape with an induced asymmetry. One way this can be found is from numerical solution of the EVP outlined in equations 2.4-2.11.

Plotted in Figure 2.10 are the in-phase and anti-phase mode shapes, evaluated for various sizes of asymmetry. In this case, the mass m_p was steadily increased. The behaviour of the modes in frequency space is presented in Figure 2.11.

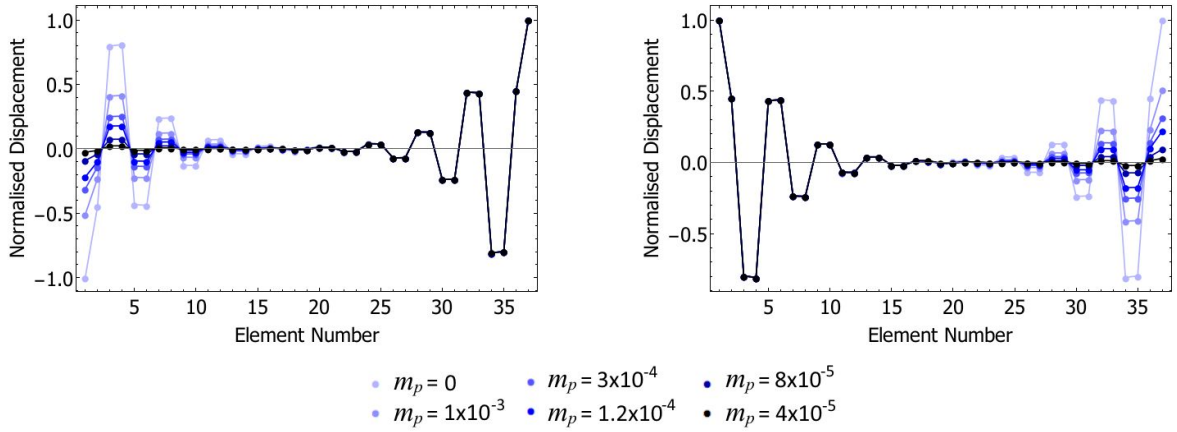

Figure 2.10 Example of mode shape change during device operation

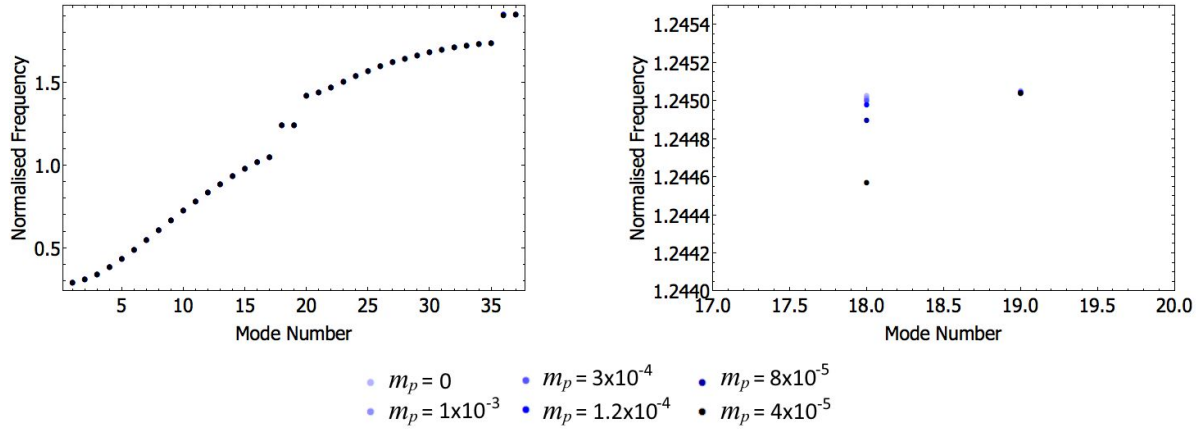

Figure 2.11 Frequency shift during device operation

The modes and frequencies behave in a very similar way to the examples in the literature, a large change is seen in the mode shape as well as a relatively small change in the natural frequencies. It can be seen that softening one of the cavities (increasing mass or reducing stiffness), will cause the lower frequency mode to drift downwards in frequency space, but will have negligible effect on the higher frequency mode. Although not shown, the reverse is true for a stiffening asymmetry, that is reducing mass or increasing stiffness, the higher frequency will drift upward with a negligible effect on

the lower frequency. In both cases the overall movement of the natural frequencies is very small in comparison to the change in the mode shape.

2.5.3 Selective excitation

The above described method of operation assumes a single mode can be excited. Previously proposed mode localization sensors have highlighted single mode excitation as a concern [27] as the excitation methods, primarily base excitation, have coupled into both modes relatively strongly. This produces a limitation on the device in that the bandwidth of each mode must be narrow enough so that the modes do not superpose. The currently proposed geometry however, allows highly selective excitation. This enables the forcing chosen to couple much more strongly into one of the modes, removing the limitation on the bandwidth. This is shown in the sequel.

The steady-state forced response of the system can be evaluated numerically using the system matrices and equation of motion outlined in equations 2.1-2.3. However, in order for there to be coupling between modes, it is necessary to introduce some dissipation into the system. To ease computation of the solution Rayleigh damping is assumed, where the damping has been assumed to be proportional to the stiffness matrix. The forced and damped system of equations to be solved is now presented in equations 2.33-2.34.

$$\mathbf{M}\underline{\ddot{u}} + \mathbf{C}\underline{\dot{u}} + \mathbf{K}\underline{u} = \underline{F} \tag{2.33}$$

$$\mathbf{C} = \beta\mathbf{K} \tag{2.34}$$

Three excitation scenarios will be discussed, in each case the excitation occurs only at the distal DOFs. The excitation arrangements are defined as in-phase, anti-phase and asymmetric forcing, these are depicted in Figure 2.12. The first two couple strongly into their synonymous modes, and weakly into the other. Asymmetric forcing refers to forcing only one distal DOF and not the other, this couples equally into both modes.

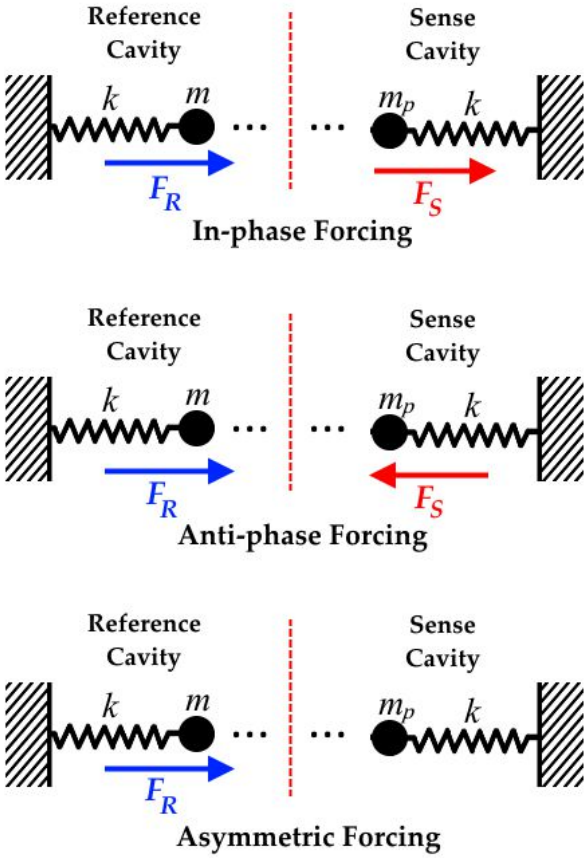

Figure 2.12 Graphics depicting the three forcing scenarios to be considered in the analysis.

The forcing is described by the forcing vector on the right-hand side of equation 2.33. The three forms this will take are shown in equations 2.35-2.36.

$$\underline{F}^{(\pm)} = [1 \quad 0 \quad \cdots \quad 0 \quad \pm 1]^{\mathrm{T}} e^{-i\Omega t} \tag{2.35}$$

$$\underline{F}^{(L)} = [1 \quad 0 \quad \cdots \quad 0 \quad 0]^{\mathrm{T}} e^{-i\Omega t} \tag{2.36}$$

This is presented in terms of the non-dimensional matrices in equation 2.37.

$$\widetilde{\mathbf{M}}\underline{\ddot{u}} + {\omega_n}^2 \beta \widetilde{\mathbf{K}}\underline{\dot{u}} + {\omega_n}^2 \widetilde{\mathbf{K}}\underline{u} = \frac{1}{m}\underline{F} \tag{2.37}$$

At steady-state, the frequency of the response is assumed to match that of the forcing and thus takes the form in equation 2.38.

$$\underline{u} = \underline{u_0} e^{-i\Omega t} \tag{2.38}$$

Substituting this into equation 2.38 yields a set of readily solvable linear equations for $\underline{u_0}$, the complex amplitude vector. This is given in equation 2.39, where a non-dimensional excitation frequency,$\widetilde{\Omega}$, has been defined.

$$\underline{u_0} = \left[\widetilde{\mathbf{M}}^{-1}.\widetilde{\mathbf{K}}\left(1 - i\omega_n\widetilde{\Omega}\beta\right) - \widetilde{\Omega}^2\mathbf{I}\right]^{-1}.\left(\frac{1}{k}\widetilde{\mathbf{M}}^{-1}.\underline{F}\right) \tag{2.39}$$

$$\widetilde{\Omega} = \frac{\Omega}{\omega_n} \tag{2.40}$$

Two damping conditions will be considered: weak damping, where the modes can be easily distinguished from each other in frequency space, and a stronger damping, although still underdamped, where the modes share a single peak in frequency space. First, the frequency response up to, and across, the first stop band is shown.

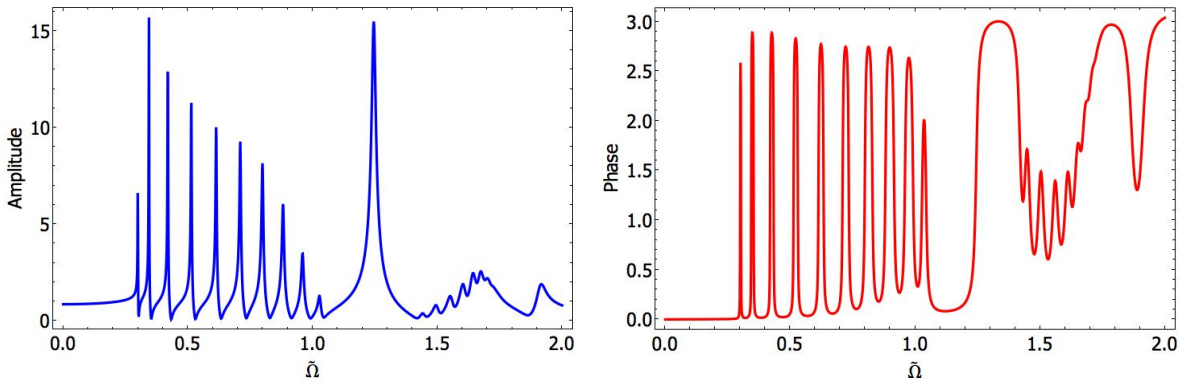

Figure 2.13 Amplitude and phase frequency response plots

The case plotted in Figure 2.13 has ten modes in the first pass band, (as expected from the 22 DOF system), there is large response present in the stop band. This is the frequency range where the two modes of interest reside. Decreasing the damping in the system will lead to a frequency separation between the modes. The weakly damped and strongly damped frequency responses are shown in Figure 2.14 for the three forcing scenarios, where only the stop band frequencies have been plotted.

The displacement fields corresponding to the peaks in Figure 2.14 are plotted in Figure 2.15. Detailing both the strongly and weakly-damped cases and the three excitation methods. Each plot displays the steady-state response due to excitation at two separate frequencies. In the strongly-damped case these are either side of the resonance peak, at

normalised frequencies of 1.22 and 1.27. For the weakly damped case these are $\widetilde{\Omega} = 1.244$ and $\widetilde{\Omega} = 1.246$. The plots in Figure 2.15 show that when the forcing is chosen to couple strongly into one mode, the chosen mode dominates across the frequency range of interest. This is true in both the strongly and weakly damped case, and therefore it can be expected that modal superposition will not have a detrimental effect on device performance.

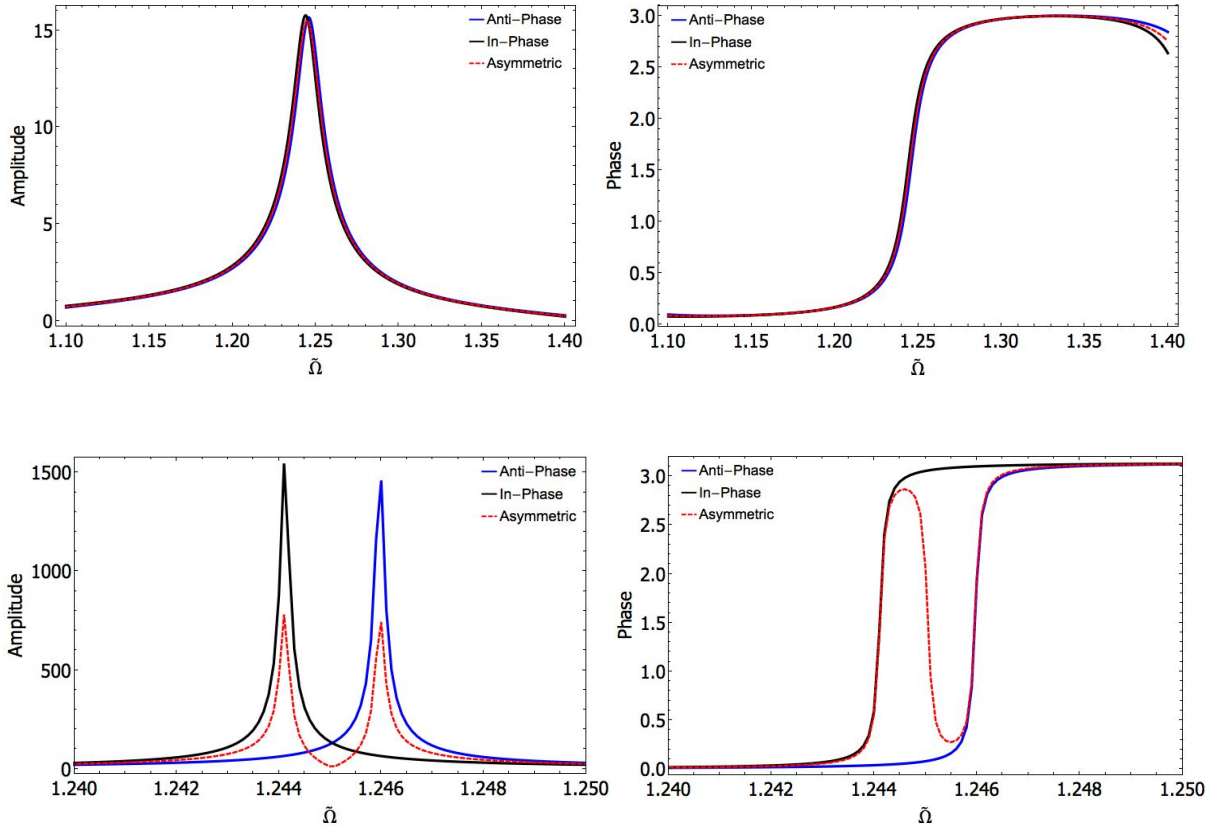

Figure 2.14 Amplitude and phase response for heavily damped (top) and weakly damped (bottom) system.

When the forcing is indiscriminate of which mode it is excited, the anti-phase mode is excited at a higher frequency than the in-phase mode. This is most likely due to the fact that, in this configuration it is half a wavelength longer, and thus more strain energy is stored in the mode, with a smaller relative change in the inertial energy. This may change for different geometric layouts. Addressing the weakly damped case first, it can be seen that that when excited at the separate frequencies, the modes are strongly coupled into, and display similar mode shapes to the selectively excited counterparts. In the heavily damped case, when excited either side of the resonant peak, it can be seen that the behaviour switches between in-phase and anti-phase oscillation. However,

the response is, as expected, a weighted sum of the two modes. The response is asymmetric; one DOF is displaced to a much greater degree than the other. This is undesirable for the purposes of the device under investigation.

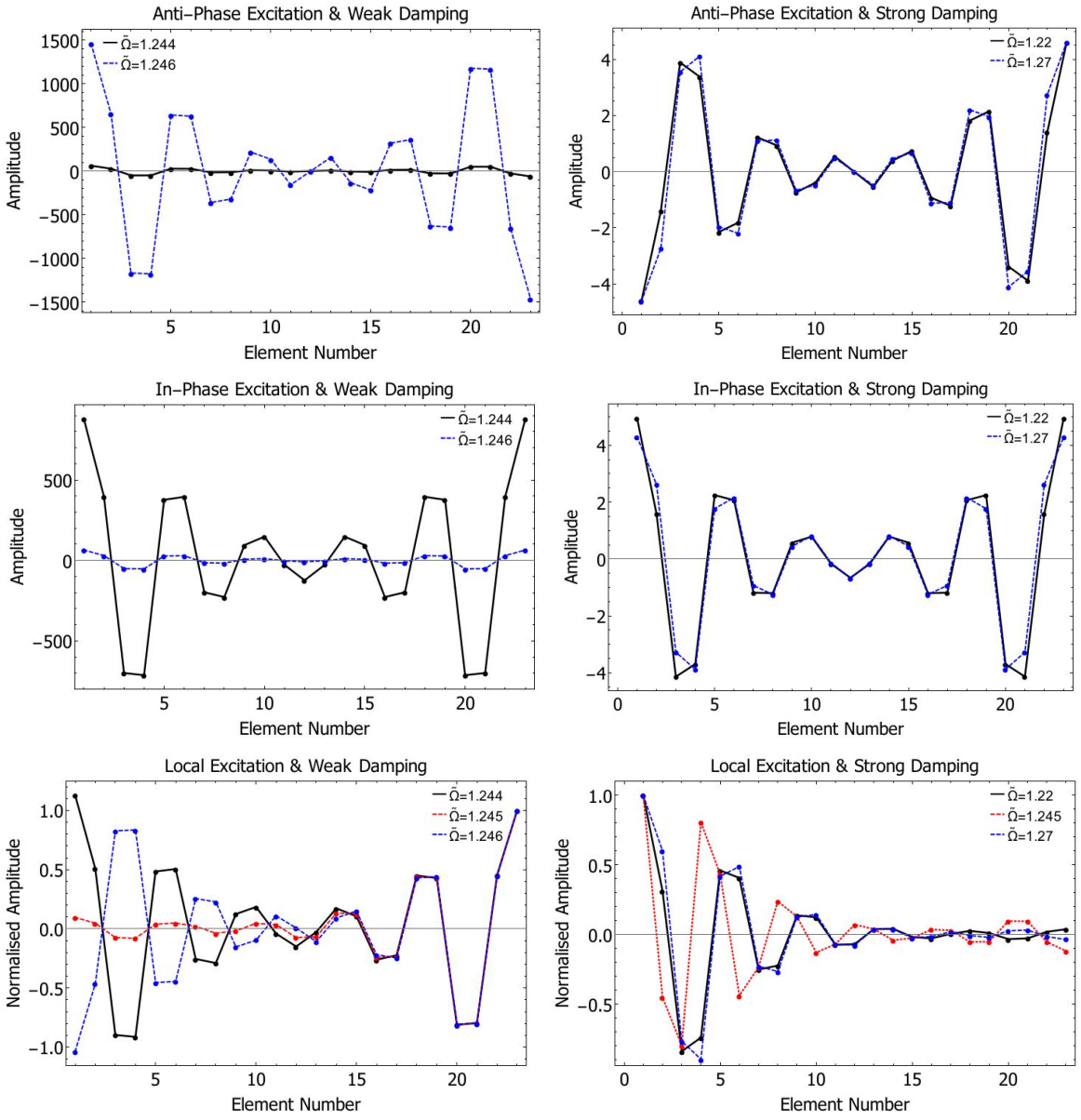

Figure 2.15 Displacement field response for selective excitation and different damping cases.

2.5.4 Sensitivity

It is known from the literature that device sensitivity increases with a decreasing strength of coupling [2], [3]. The potential form of this relationship can be approximated by the model of section 2.4.2. If it is again assumed that the mass perturbation is small, that is $\delta \ll 1$. Then the ratio of the two DOFs can be simplified as in equations 2.41-2.44.

If $\mu \neq 0,\ \delta \ll 1$;

$$\left|\frac{u_2}{u_1}\right| = \frac{e^{-N\mu}\left(\delta + \sqrt{4e^{2N\mu} + 4e^{2N\mu}\delta + \delta^2}\right)}{2(1+\delta)} \tag{2.41}$$

$$\left|\frac{u_2}{u_1}\right| \approx \frac{e^{-N\mu}\left(\delta + 2e^{N\mu}\sqrt{1+\delta}\right)}{2(1+\delta)} \tag{2.42}$$

$$\left|\frac{u_2}{u_1}\right| \approx \frac{e^{-N\mu}(\delta + 2e^{N\mu})}{2} \tag{2.43}$$

$$\left|\frac{u_2}{u_1}\right| \approx \frac{\delta e^{-N\mu} + 2}{2} \tag{2.44}$$

This implies that for small δ, the response is approximately linear. The potential sensitivity can then be found by differentiating the mode shape ratio with respect to δ.

$$\left|\frac{\partial}{\partial\delta}\left(\left|\frac{u_2}{u_1}\right|\right)\right| \approx \frac{e^{-N\mu}}{2} \tag{2.45}$$

This expression can be directly compared to that found in the literature for a 2-DOF mode localization sensor, highlighted in equation 1.32. For reference these are collated in Table 2.1. It is seen in equation 2.45 that the sensitivity is indeed a function of the coupling strength, however, the coupling strength is now defined by $e^{N\mu}$ rather than κ. Recalling that $\mu < 0$, causing spatial decay, equation 2.45 shows that increasing either the number of periods in the array or the propagation constant yields an exponential increase in sensitivity. This introduces an extra tuning term, potentially allowing for lower coupling strengths, and hence higher sensitivities, than currently achievable. The similarity of the two sensitivity expressions provides evidence towards the fundamental equivalence of the behaviour of the two systems. That is, the periodically coupled mode localization sensor behaves as the 2-DOF mode localization sensor and it is expected that conclusions drawn in previous research should still hold for the newly proposed system.

Table 2.1 Mass sensitivity comparison

System	Sensitivity to a mass perturbation	References
2-DOF Mode localization sensor	$\frac{1}{2\kappa}$	Equation (3), [24]
Periodically coupled mode localization sensor	$\frac{1}{2e^{N\mu}}$	Equation (2.45)

2.6 Conclusions

A novel MEMS sensor protocol has been introduced, utilising a SAW architecture. The device response and characteristics have been described qualitatively on a fundamental level utilising an LPM. An analytical approximation was presented. These were used in combination to depict and describe the mode of operation and performance.

Device response to selective excitation was investigated and depicted graphically. It was shown that the forcing could be chosen to couple strongly into a single mode. Further evidence for this was provided in the form of the numerical solution for the forced response, this showed device behaviour as predicted by the frequency domain plots.

The sensitivity was contrasted to that achievable with a 2-DOF mode localization sensor. The analytical expression used for the comparison was derived using a 2-DOF representation of the system. This yielded an approximate expression for sensitivity that implied approximate linearity of the response and portrayed a dependence upon coupling strength. It was shown that increasing the periods in the coupling array would yield an exponential increase in sensitivity.

The utility of using a periodic coupling array has been proposed to be twofold; the extension to robust sensor geometries such as SAW being the first and secondly the potential for an exponential increase in sensitivity.

Chapter 3. Generalised Model of a SAW Mode Localization Sensor

3.1 Introduction

After the insight gained through the preliminary investigation of lumped parameter models performed in the preceding chapter, the usual engineering route would be to take one of three paths: (1) develop a more accurate analytical model, (2) perform numerical simulations on the system of interest or (3) design a series of experiments or a prototype device for further investigation. The choice of which route to take is often dependent on resources, time constraints and practicality. It is often preferable for many systems to develop experiments with the design aided through finite element analysis (FEA). In the current case however, it was decided to first develop a more accurate analytical model to inform the design of the device. The reasons for this choice over the alternatives are expounded here.

Analytical models can be more useful for insight and design in that they describe the expanse of the parameter space, whereas numerical simulations and experiments provide data points from which the behaviour away from this point must be inferred. Arguably however, the data points provided by numerical or experimental methods are more true to the real system as they do not suffer from the assumptions often necessary to describe the problem analytically. Furthermore with the speed of modern computers, a parameter space can often be mapped out completely and fully using FEA. In the case of the current system however, it was not possible to use FEA in this way as a design tool. The primary reasons for this are twofold, i) The domain cannot be reasonably reduced without losing crucial information, ii) The feature sizes are orders of magnitude smaller than the total simulation domain size. The specifics of how these limitations manifest and affect the simulation are outlined in the following.

Firstly, due to the nature of the device utilising a break in the symmetry of the problem, the geometry cannot be reduced significantly by exploiting symmetric planes in the model. Additionally, in order to reduce bulk scattering and from the edges of the reflectors, it is necessary to ensure the plate thickness is sufficiently small when

compared to the wavelength [38]. This leads to a large array of reflectors and consequently a model that is very large in comparison to the wavelength, likely on the order of hundreds of wavelengths long. Furthermore, a high stress point appears at every discontinuity in the surface, requiring a high mesh resolution to resolve it accurately. This requires mesh elements that are thousands of times smaller than the wavelength of interest. Thus the model is necessarily very large and involves high stress gradients and is therefore very computationally expensive.

This problem has been encountered previously in the study of interdigitated transducers (IDTs). A method of analysis employing both the finite element method (FEM) and the boundary element method (BEM) was formulated to provide a way of solving the problem accurately for many strips with low computational effort. It was potentially viable to solve this system utilising the FEM/BEM approach, however, the script would have to be developed specifically for this problem. It was therefore more time efficient to develop an analytical solution that described the problem that could then serve to directly drive the design of prototype devices.

It is possible that the insight gained from the investigations of chapter 2 could have enabled the design of a 'best guess' prototype. However, as this design is still in its infancy, with many potential permutations, it would be limiting to constrain the investigation at this point. The optimal course of action was deemed to be the investment of time into the development of a more detailed analytical model and the subsequent analysis. The body of this chapter therefore presents the derivation of a general analytical model of the proposed SAW device.

The solution sought is the surface displacement fields within the resonant cavities. The full model is governed by the 3D elastodynamic equations [39]. As only the surface displacement for straight crested waves is sought, the system can be reduced to an equivalent one-dimensional model. This enables the use of the transfer matrix method, which applies rigorously only to one-dimensional solutions [7], to compute the amplitude and phase change across the finite periodic arrays. The implications and effects of this dimension reduction will be discussed within the body of the chapter.

Before the generalised solution that represents the novelty of this chapter can be presented, some preliminaries from the literature need to be addressed. The first of which is the aforementioned reduction of the 3D elastodynamic equations to a one-dimensional form, which is addressed in section 3.2. Although the analysis can theoretically apply to all types of SAW, the present work will consider only Rayleigh waves. Therefore, the reduction of the elastodynamic equations is addressed for plane, straight-crested Rayleigh waves.

The second preliminary is the derivation of the transfer matrix for locally periodic media. This is necessary to define the solutions across the arrays that enclose the cavities and is derived in section 3.4. The wave equation solution will be utilised in the validation of the generalised model by way of comparison to a finite element model of a simplified system.

Section 3.5 presents the derivation of the analytical model, culminating in the solution of the displacement fields within each cavity. This section presents one of the main novel contributions of this thesis to the literature. A generalised geometry is presented in order to capture the complete parameter space. Section 3.5 outlines a simplified one-dimensional finite element model of the system. The system is modelled as a one-dimensional wave equation problem; this eliminates the geometric discontinuities that lead to the stress singularities in the 2D model. This is solved in the frequency domain, which amounts to a steady-state solution of an inhomogeneous one-dimensional Helmholtz equation with variable parameters. This is contrasted to the analytical model in section 3.6. The validity of the model to the system of interest and other potential methods are discussed in section 3.7 before conclusions are outlined in section 3.8.

3.2 Reduction of 3D elastodynamic equations of motion to one-dimension

3.2.1 The linearized 3D elastodynamic equations of motion

This brief section serves to present the coordinate system that will be used throughout and outline the basic equations from which the derivation will proceed. The linearized theory of elasticity is presented in several references, a particularly clear example, used by the author for reference is shown in [39]. The equations are described using the

material description, that is, the natural, undeformed state of the elastic body is used as a reference to the subsequent displacements. A rectangular coordinate system will be employed with the components x_1, x_2 and x_3. The displacement components in each direction are u_1 , u_2 and u_3 respectively, the column vector of displacement components is denoted $\underline{u}$. A right-handed coordinate system is described in which the x_1-direction runs left to right on the page, x_2 runs from top to bottom and x_3 extends into the page as displayed in Figure 3.1.

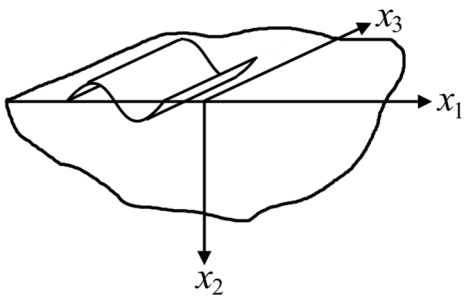

Figure 3.1 Coordinate system and illustration of a segment of one wavelength of a straight crested Rayleigh wave

So as not to overcomplicate the explanation of the phenomena within the chapter, consideration will only be given to an isotropic half space. It will be shown in the conclusion that the results can be easily extended to an anisotropic half space with the use of results readily available in the literature. The displacement equation of motion for an isotropic elastic solid is shown in equation 3.1 [39].

$$\mu_L \nabla^2 \underline{u} + (\lambda_L + \mu_L) \nabla \nabla \cdot \underline{u} = \rho \, \underline{\ddot{u}} \tag{3.1}$$

Where λ_L and μ_L, respectively are the first and second Lamé parameters. ρ is the mass density and ∇ is the Gradient operator. This will serve as the starting point for the following derivation.

The stress-strain relationships are also required in the following and are presented here for reference. A normal stress, τ_{ii}, is related to the strain components through equation 3.2 [39].

$$\tau_{ii} = \lambda_L \left(\frac{\partial u_1}{\partial x_1} + \frac{\partial u_2}{\partial x_2} + \frac{\partial u_3}{\partial x_3} \right) + 2\mu_L \frac{\partial u_i}{\partial x_i} \tag{3.2}$$

Where $i = 1,2$ or 3. A shear stress, τ_{ij},is related to the strain components through equation 3.3 [39].

$$\tau_{ij} = \mu_L \left(\frac{\partial u_i}{\partial x_j} + \frac{\partial u_j}{\partial x_i} \right) \tag{3.3}$$

Where $i, j = 1,2$ or 3 and $i \neq j$.

3.2.2 Rayleigh waves in a semi-infinite half space

The solution of Rayleigh waves in a semi-infinite half space is published in many locations, a very brief summary of the derivation using the present notation is shown here for completeness. For more detail the reader is directed to references [39], [40]. The straight-crested x_1 -propagating Rayleigh wave to be considered is depicted in Figure 3.1.

The elastic body displayed in Figure 3.1 can be described as a semi-infinite half space with bounding surfaces at $x_2 = 0$ and $x_3 = \pm\infty$, with plane waves propagating in the x_1-direction. It is clear that the problem can be immediately reduced to one of two-dimensional plane-strain, that is $u_3 = 0$ and $\frac{\partial}{\partial x_3} = 0$. Equation 3.1 can now be expanded in component form.

$$(\lambda_L + 2\,\mu_L)\frac{\partial^2 u_1}{\partial {x_1}^2} + \mu_L \frac{\partial^2 u_1}{\partial {x_2}^2} + (\lambda_L + \mu_L)\frac{\partial^2 u_2}{\partial x_1 \partial x_2} = \rho\, \frac{\partial^2 u_1}{\partial t^2} \tag{3.4}$$

$$(\lambda_L + 2\,\mu_L)\frac{\partial^2 u_2}{\partial {x_2}^2} + \mu_L \frac{\partial^2 u_2}{\partial {x_1}^2} + (\lambda_L + \mu_L)\frac{\partial^2 u_1}{\partial x_1 \partial x_2} = \rho\, \frac{\partial^2 u_2}{\partial t^2} \tag{3.5}$$

One well known solution to the above equations is that of a wave confined to the surface - a "Rayleigh wave" - The form of the trial solution is presented in equations 3.6-7.

$$u_1 = Ae^{-\xi x_2 + i\gamma(x_1 - c_R t)} \tag{3.6}$$

$$u_2 = Be^{-\xi x_2 + i\gamma(x_1 - c_R t)} \tag{3.7}$$

Where γ and ξ are the generally complex wavenumbers in the u_1 and u_2 directions respectively and c_R is the Rayleigh wave speed. A and B are arbitrary constants. The

real part of ξ in 3.6-7 is considered to be positive, such that waves decay with distance from the surface. 3.6-7 are inserted into 3.4-5 yielding two coupled algebraic equations constituting an EVP that can be solved for permissible values of ξ and the corresponding amplitude ratios $\left(\frac{B}{A}\right)$ (equations 3.8-3.15).

$$\xi_1 = \alpha\gamma \tag{3.8}$$

$$\xi_2 = \beta\gamma \tag{3.9}$$

$$\left(\frac{B}{A}\right)_1 = \frac{i}{\alpha} \tag{3.10}$$

$$\left(\frac{B}{A}\right)_2 = i\,\beta \tag{3.11}$$

$$\alpha = \left(1 - \frac{{c_R}^2}{{c_T}^2}\right)^{\frac{1}{2}} \tag{3.12}$$

$$\beta = \left(1 - \frac{{c_R}^2}{{c_L}^2}\right)^{\frac{1}{2}} \tag{3.13}$$

$${c_T}^2 = \frac{\mu_L}{\rho} \tag{3.14}$$

$${c_L}^2 = \frac{\lambda_L + \mu_L}{\rho} \tag{3.15}$$

From 3.8-3.15 and 3.6-7 a general solution can be written.

$$u_1 = \left(A_1 e^{-\alpha\gamma x_2} + A_2 e^{-\beta\gamma x_2}\right) e^{i\gamma(x_1 - c_R t)} \tag{3.16}$$

$$u_2 = \left(\alpha^{-1} A_1 e^{-\alpha\gamma x_2} + \beta A_2 e^{-\beta\gamma x_2}\right) i e^{i\gamma(x_1 - c_R t)} \tag{3.17}$$

Note that the behaviour of the wavenumber with respect to the wave-speed (the dispersion) is still not known. This is to be found upon insertion of equations 3.16-17 into the boundary conditions. The boundary conditions for the free surface regions are the vanishing of both the normal and shear surface stresses (τ_{22} and τ_{21}respectively) at the boundary ($x_2 = 0$). These conditions are given explicitly in equations 3.18-19, with the u_3 and $\frac{\partial}{\partial x_3}$ terms omitted.

$$\tau_{22_{x_2=0}} = \left[\lambda_L \left(\frac{\partial u_1}{\partial x_1} + \frac{\partial u_2}{\partial x_2}\right) + 2\mu_L \frac{\partial u_2}{\partial x_2}\right]_{x_2=0} = 0 \tag{3.18}$$

$$\tau_{21_{x_2=0}} = \left[\mu_L \left(\frac{\partial u_1}{\partial x_2} + \frac{\partial u_2}{\partial x_1}\right)\right]_{x_2=0} = 0 \tag{3.19}$$

Inserting the general solution 3.16-17 into 3.18 and 3.19 yields a second coupled algebraic problem [39]. Setting the determinant equal to zero yields the Rayleigh phase

velocity (equation 3.20). Demonstrating that the Rayleigh waves in the un-plated regions are non-dispersive, that is, the speed of propagation is independent of the wavelength.

$$\left(2-\frac{{c_R}^2}{{c_T}^2}\right)^{\frac{1}{2}}-4\left(1-\frac{{c_R}^2}{{c_L}^2}\right)^{\frac{1}{2}}\left(1-\frac{{c_R}^2}{{c_T}^2}\right)^{\frac{1}{2}}=0 \tag{3.20}$$

This equation has one root in the interval $0 < c_R < c_T$, which corresponds to the Rayleigh wave speed [39]. The wave-speed c_R is therefore a function of the material properties, and can itself, be thought of as a material property. An approximation for the ratio of c_R to c_T, dependent only on the Poisson's ratio, has been proven approximately accurate for isotropic materials [39], [40] and is shown in equation 3.21.

$$c_R = \frac{0.862 + 1.14v}{1+v} c_T \tag{3.21}$$

Within this thesis the primary substrate material of interest is Lithium Niobate, although anisotropic, the volume average Poisson's ratio has been quoted as 0.25-0.26 [41]. In this special case, taking $v = 0.25$, substitution of 3.21 into 3.12 and then subsequently into 3.20 and 3.13 yields the depth wave numbers as $\alpha = 0.3933$ and $\beta = 0.8475$. Substitution of equations 3.16-17 into the boundary conditions 3.18-19 and subsequent algebraic manipulation yields the ratio of $\frac{A_1}{A_2} = -0.5773$. Inputting these values into equations 3.16-17 yields the 2D free wave solution that will be employed throughout this thesis.

$$u_1 = A(-0.5773e^{-0.3933\gamma x_2} + e^{-0.8475\gamma x_2})Cos(\gamma(x_1 - c_R t)) \tag{3.22}$$

$$u_2 = A(1.4679e^{-0.3933\gamma x_2} - 0.8475\, e^{-0.8475\gamma x_2})Sin(\gamma(x_1 - c_R t)) \tag{3.23}$$

3.2.3 Rayleigh waves in a plated semi-infinite half space

The effect of the plating on the substrate will be represented using equivalent boundary conditions. This necessitates the assumption that the plating thickness is much smaller than the wavelength, which is valid in this scenario. The two-dimensional equations of motion and trial solution presented in equations 3.4-3.7 still hold and the derivation will proceed from there. It is also of note that once the substrate is plated, many

different wave types can be supported. The physics in this formulation is truncated substantially to only consider the possibility of the 'extended Rayleigh wave' [42].

The equivalent boundary conditions are formulated using thin plate equations. These were first introduced by Tiersten [42] and are known eponymously. Tiersten derived the boundary conditions by assuming that the effect of the plate could be represented as an equivalent stress condition due to the thin plate's extensional stiffness and inertia. Due to the assumed thinness of the plate, the flexural stiffness contribution can be neglected. The equivalent boundary conditions are presented in equations 3.24-25.

$$\tau_{22} = 2\bar{h}\bar{\rho}\ddot{u}_2 \tag{3.24}$$

$$\tau_{21} = -8\,\overline{\mu_L}\bar{h}\left(\frac{\overline{\lambda_L}+\overline{\mu_L}}{\overline{\lambda_L}+2\overline{\mu_L}}\right)\frac{\partial^2 u_1}{\partial {x_1}^2} + 2\bar{h}\bar{\rho}\ddot{u}_1 \tag{3.25}$$

Where an overbar has been used to distinguish properties that correspond to the plate rather than the substrate. The sole new parameter introduced is $\bar{h}$ which is half the plating thickness. The $2\bar{h}\bar{\rho}\ddot{u}_i$ term common to both boundary conditions corresponds to the inertia of the plating in either direction. The additional term in the shear stress boundary condition corresponds to the extensional stiffness. The boundary conditions to be fulfilled at the surface of the half space are written explicitly in equations 3.26-27.

$$\left[\mu_L\left(\frac{\partial u_1}{\partial x_2}+\frac{\partial u_2}{\partial x_1}\right) + 8\,\overline{\mu_L}\bar{h}\left(\frac{\overline{\lambda_L}+\overline{\mu_L}}{\overline{\lambda_L}+2\overline{\mu_L}}\right)\frac{\partial^2 u_1}{\partial {x_1}^2} - 2\bar{h}\bar{\rho}\ddot{u}_1\right]_{x_2=0} = 0 \tag{3.26}$$

$$\left[\lambda_L\left(\frac{\partial u_1}{\partial x_1}+\frac{\partial u_2}{\partial x_2}\right) + 2\mu_L\frac{\partial u_2}{\partial x_2} - 2\bar{h}\bar{\rho}\ddot{u}_2\right]_{x_2=0} = 0 \tag{3.27}$$

The general solution within the plated region (eqs. 3.28-31) can be deduced from the un-plated solution (eqs. 3.16-17) and the knowledge that the plated region trial solution will have unique wavenumbers and wave-speed. Where the use of an over-bar to distinguish parameters belonging to the plated substrate has been continued.

$$\overline{u_1} = \left(\overline{A_1}e^{-\overline{\alpha}\,\overline{\gamma}\,x_2} + \overline{A_2}e^{-\overline{\beta}\,\overline{\gamma}\,x_2}\right)e^{i\overline{\gamma}(x_1-\overline{c_R}t)} \tag{3.28}$$

$$\overline{u_2} = \left(\bar{\alpha}^{-1}\overline{A_1}e^{-\bar{\alpha}\,\bar{\gamma}\,x_2} + \bar{\beta}\,\overline{A_2}e^{-\bar{\beta}\,\bar{\gamma}\,x_2}\right)ie^{i\bar{\gamma}(x_1-\overline{c_R}t)} \tag{3.29}$$

$$\bar{\alpha} = \left(1 - \frac{\overline{c_R}^2}{{c_T}^2}\right)^{\frac{1}{2}} \tag{3.30}$$

$$\bar{\beta} = \left(1 - \frac{\overline{c_R}^2}{{c_L}^2}\right)^{\frac{1}{2}} \tag{3.31}$$

In an identical fashion to the un-plated substrate derivation, the trial solution is inserted into the boundary conditions yielding a determinantal expression, the derivation of which is provided in reference [42] for an isotropic substrate and [38], [43] for an anistropic substrate. Subsequent expansion of the determinantal equation yields a polynomial in $\bar{\gamma}$ and $\overline{c_R}$. Any real positive $\bar{\gamma}$ will provide the values of $\overline{c_R}$ that correspond to the dimensionless phase velocities for the modes extant in the plated substrate region [42]. It is noted that negative or complex values of $\bar{\gamma}$ are inadmissible as only real positive wavelengths are considered. The validity of obtaining the dispersion curves using this method is discussed in reference [42], it is necessary that the thin plate assumption is adhered to. Dispersion curves for various material combinations of interest are available in the literature, including for anisotropic substrates such a Lithium Niobate [38].

3.2.4 Reduction to one-dimension

It is common to consider the propagation of SAW as a quasi-one-dimensional problem. A normal modes expansion method has been presented by Auld in reference [44] and utilised to calculate the reflection from a single strip in reference [45]. In addition, the prevalent coupling of modes method assumes a loaded wave equation as its starting point [46] with the parameters to be found through experiment or simulation. The solution to be utilised here however was presented in references [38], [43] where Sinha and Tiersten derived the equivalent equations of motion for the surface displacement in a partially plated substrate.

Sinha and Tiersten used a variational principle and inserted a solution of the form shown in equations 3.6-7, where the depth behaviour is known from the derivations discussed in sections 3.2.2 and 3.2.3.

$$u_j(x_1, x_2, t) = \varphi_j(x_2)\psi(x_1, t) \tag{3.32}$$

Where $j = 1,2$ and $\varphi_j(x_2)$corresponds to the depth behaviour, displayed explicitly in equations 3.16 and 3.17 for the example of an unplated substrate. The solution is then inserted into the variational indicator and integrated through the depth to eliminate the x_2 dependence. After the variations are performed the result is the equations of motion and the boundary conditions for both the plated, and free, substrates. The equations of motion are found to be of the form presented in equation 3.33 for the example of an un-plated region.

$$C_1 \frac{\partial^2 \psi}{\partial {x_1}^2} + C_2 \frac{\partial \psi}{\partial x_1} + C_3 \psi = C_4 \rho \frac{\partial^2 \psi}{\partial t^2} \tag{3.33}$$

The parameters C_k are constants, consisting of sums of products of components of the elasticity matrix and the integrals of the depth behaviour, provided in detail in references [38], [43]. The edge conditions between a plated and un-plated region take the form given in equations 3.34-35.

$$\psi = \bar{\psi} \tag{3.34}$$

$$T^s{}_1 = \bar{T}^s{}_1 + 2\bar{h}\overline{\mu_L}\left(1 + \frac{3\overline{\lambda_L} + 2\overline{\mu_L}}{\overline{\lambda_L} + 2\overline{\mu_L}}\right)\overline{\varphi_1}(0)\overline{\varphi_1}^*(0)\frac{\partial \bar{\psi}}{\partial x_1} \tag{3.35}$$

Where $T^s{}_k$ are surface stresses, they correspond to the tractions at the surface, after the depth integrals have been performed. The first boundary condition therefore specifies continuity of the surface displacement. The second boundary condition equated the stress state at the surface in both regions, however, there is an additional term from the plated region. This arises due to the discontinuity in the surface, and corresponds to a point load at each discontinuity. This is discussed in depth in references [45], [47]–[49]

The preceding system of equations is solved by a solution of the form of equation 3.36 in the un-plated region and equation 3.37 in the plated region.

$$\psi(x_1, t) = (Ae^{i\gamma x_1} + Be^{-i\gamma x_1})e^{-i\omega t} \tag{3.36}$$

$$\bar{\psi}(x_1, t) = (\bar{A}e^{i\bar{\gamma}x_1} + \bar{B}e^{-i\bar{\gamma}x_1})e^{-i\omega t} \tag{3.37}$$

Where $\omega = \gamma c_R$.The dispersion relations in the one-dimensional theory have been shown to agree favourably with that of the three-dimensional theory presented in the opening sections [38], [43].

3.3 Excitation and transduction

The previous sections have discussed free wave motion. These solutions described the form of Rayleigh surface waves as well as providing the wave speed with which they propagate in a given substrate. In practise, the device will undergo sustained oscillation due to a time harmonic load. It is therefore necessary to determine the force-displacement relationship due to such a load. This section begins by discussing the classic solution to 'Lamb's problem' of a time harmonic line load. Following this is a description of the interdigitated transducer and the models that describe it.

3.3.1 Response of an elastic half-space to a time harmonic line load

Lamb [50] first investigated the response of an elastic body to both time harmonic and impulsive line loads. Since this work the method and results have become a staple of textbooks on elastic waves [39], [40]. The problem is posed as the solution of the plane strain equation of motion, defined in equations 3.4-5, with the boundary conditions described below in equations 3.38 and 3.39.

$$\tau_{22_{x_2=0}} = -P\delta(x_1)e^{-i\omega t} \tag{3.38}$$

$$\tau_{21_{=0}} = 0 \tag{3.39}$$

Where P has dimensions N/m and $\delta(x_1)$ is the Dirac delta function. Their product describes a distributed load applied along a straight line running along the x_3 direction, as depicted in Figure 3.2.

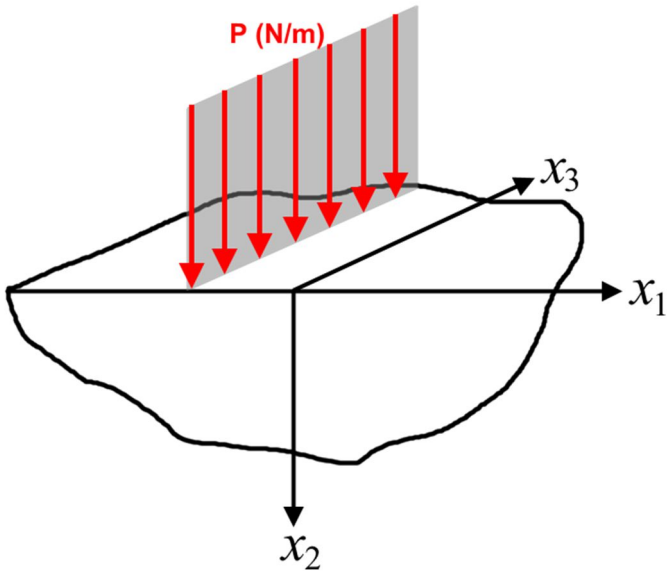

Figure 3.2 Orientation of time harmonic line load with respect to the coordinate system and free surface.

It is convenient for the solution process to employ the Helmholtz decomposition and represent the equations of motion in terms of two potentials separately defining the divergence and curl of the vector field, $\underline{u}$. The potentials are defined in equations 3.40 and 3.41. The displacement components u_1 and u_2 can be defined in terms of the potentials by equations 3.42 and 3.43 [39].

$$\nabla \cdot \underline{u} = \frac{\partial u_1}{\partial x_1} + \frac{u_2}{\partial x_2} \tag{3.40}$$

$$\nabla \times \underline{u} = \left(\frac{\partial u_1}{\partial x_2} - \frac{u_2}{\partial x_1}\right)\mathbf{k} \tag{3.41}$$

$$u_1 = \frac{\partial(\nabla \cdot \underline{u})}{\partial x_1} + \frac{\left|(\nabla \times \underline{u})\right|}{\partial x_2} \tag{3.42}$$

$$u_2 = \frac{\partial(\nabla \cdot \underline{u})}{\partial x_2} - \frac{\partial\left|(\nabla \times \underline{u})\right|}{\partial x_1} \tag{3.43}$$

The equations of motion in terms of the potentials become equations 3.44 and 3.45.

$$\frac{\partial^2(\nabla \cdot \underline{u})}{\partial {x_1}^2} + \frac{\partial^2(\nabla \cdot \underline{u})}{\partial {x_2}^2} = {c_L}^{-2}\frac{\partial^2(\nabla \cdot \underline{u})}{\partial t^2} \tag{3.44}$$

$$\frac{\partial^2(\nabla \times \underline{u})}{\partial {x_1}^2} + \frac{\partial^2(\nabla \times \underline{u})}{\partial {x_2}^2} = {c_T}^{-2} \frac{\partial^2(\nabla \times \underline{u})}{\partial t^2} \tag{3.45}$$

The set of equations can be solved by employing a standard integral transform technique, the exponential Fourier transform [39], as defined by equation 3.46. The inverse transform is defined in equation 3.47.

$$f^{(F)}(\gamma) = \mathcal{F}[f(x_1)] = \int_{-\infty}^{\infty} e^{i\gamma x_1} f(x_1) dx_1 \tag{3.46}$$

$$f(x_1) = \mathcal{F}^{-1}[f^{(F)}(\gamma)] = \frac{1}{2\pi} \int_{-\infty}^{\infty} e^{-i\gamma x_1} f^{(F)}(\gamma) d\gamma \tag{3.47}$$

The appropriate forms of the potential function solutions in Fourier space are given in equations 3.48-49, with the time harmonicity omitted. The stress equations 3.18 and 3.19 are first represented using the potentials and then transformed yielding equations 3.50 and 3.51.

$$\mathcal{F}\big[(\nabla \cdot \underline{u})\big] = \widehat{\Phi}(\gamma) e^{-(\gamma^2 - \omega^2 {c_L}^{-2})^{\frac{1}{2}} x_2} \tag{3.48}$$

$$\mathcal{F}\big[(\nabla \times \underline{u})\big] = \widehat{\theta}(\gamma) e^{-(\gamma^2 - \omega^2 {c_T}^{-2})^{\frac{1}{2}} x_2} \tag{3.49}$$

$$\tau_{22_{x_2=0}} = \mu_L \left(-\omega^2 {c_T}^{-2} \mathcal{F}\big[(\nabla \cdot \underline{u})\big] - 2 \frac{\partial^2 \mathcal{F}\big[(\nabla \cdot \underline{u})\big]}{\partial {x_2}^2} + i\gamma^2 \frac{\partial \mathcal{F}\big[(\nabla \times \underline{u})\big]}{\partial x_2} \right) \tag{3.50}$$

$$\tau_{21_{=0}} = \mu_L \left(i\gamma 2 \frac{\partial \mathcal{F}\big[(\nabla \cdot \underline{u})\big]}{\partial x_2} - \omega^2 {c_T}^{-2} \mathcal{F}\big[(\nabla \times \underline{u})\big] + 2\gamma^2 \mathcal{F}\big[(\nabla \times \underline{u})\big] \right) \tag{3.51}$$

Equations 3.40-41 and 3.48-49 are inserted into equations 3.50-51 yielding equations for $\mathcal{F}\big[(\nabla \cdot \underline{u})\big]$ and $\mathcal{F}\big[(\nabla \times \underline{u})\big]$.

$$(2\gamma^2 - \omega^2 {c_T}^{-2}) \mathcal{F}\big[(\nabla \cdot \underline{u})\big] - 2i\gamma(\gamma^2 - \omega^2 {c_T}^{-2})^{\frac{1}{2}} \mathcal{F}\big[(\nabla \times \underline{u})\big] = -\frac{P}{\mu_L} \tag{3.52}$$

$$2i\gamma(\gamma^2 - \omega^2 {c_L}^{-2})^{\frac{1}{2}} \mathcal{F}\big[(\nabla \cdot \underline{u})\big] - (2\gamma^2 - \omega^2 {c_T}^{-2}) \mathcal{F}\big[(\nabla \times \underline{u})\big] = 0 \tag{3.53}$$

These are solved by equations 3.54-55.

$$\mathcal{F}\left[(\nabla \cdot \underline{u})\right] = -\frac{2\gamma^2 - \omega^2 {c_T}^{-2}}{\mathcal{H}(\gamma)} \frac{P}{\mu_L} \tag{3.54}$$

$$\mathcal{F}\left[(\nabla \times \underline{u})\right] = \frac{2i\gamma(\gamma^2 - \omega^2 {c_L}^{-2})^{\frac{1}{2}}}{\mathcal{H}(\gamma)} \frac{P}{\mu_L} \tag{3.55}$$

$$\mathcal{H}(\gamma) = (2\gamma^2 - \omega^2 {c_T}^{-2})^2 - 4\gamma^2(\gamma^2 - \omega^2 {c_L}^{-2})^{\frac{1}{2}}(\gamma^2 - \omega^2 {c_T}^{-2})^{\frac{1}{2}} \tag{3.56}$$

Using equations 3.42-43, these solutions can be put in terms of the displacement fields, as shown in equations 3.57 and 3.58.

$$\mathcal{F}[u_1] = -i\gamma\mathcal{F}\left[(\nabla \cdot \underline{u})\right] - (\gamma^2 - \omega^2 {c_T}^{-2})^{\frac{1}{2}}\mathcal{F}\left[(\nabla \times \underline{u})\right] \tag{3.57}$$

$$\mathcal{F}[u_2] = -(\gamma^2 - \omega^2 {c_L}^{-2})^{\frac{1}{2}}\mathcal{F}\left[(\nabla \cdot \underline{u})\right] + i\gamma\mathcal{F}\left[(\nabla \times \underline{u})\right] \tag{3.58}$$

Inversion of equations 3.57-58 back into the spatial domain yields expressions 3.59-64.

$$u_1 = (I_{u11} + I_{u12})\frac{P}{\mu_L} \tag{3.59}$$

$$u_2 = (I_{u21} + I_{u22})\frac{P}{\mu_L} \tag{3.60}$$

$$I_{u11} = \frac{i}{2\pi}\int_{-\infty}^{\infty} \frac{\gamma(2\gamma^2 - \omega^2 {c_T}^{-2})}{\mathcal{H}(\gamma)} e^{-i\gamma x_1 - (\gamma^2 - \omega^2 {c_L}^{-2})^{\frac{1}{2}} x_2} d\gamma \tag{3.61}$$

$$I_{u12} = \frac{-i}{\pi}\int_{-\infty}^{\infty} \frac{\gamma(\gamma^2 - \omega^2 {c_T}^{-2})^{\frac{1}{2}}(\gamma^2 - \omega^2 {c_L}^{-2})^{\frac{1}{2}}}{\mathcal{H}(\gamma)} e^{-i\gamma x_1 - (\gamma^2 - \omega^2 {c_T}^{-2})^{\frac{1}{2}} x_2} d\gamma \tag{3.62}$$

$$I_{u21} = \frac{1}{2\pi}\int_{-\infty}^{\infty} \frac{(\gamma^2 - \omega^2 {c_L}^{-2})^{\frac{1}{2}}(2\gamma^2 - \omega^2 {c_T}^{-2})}{\mathcal{H}(\gamma)} e^{-i\gamma x_1 - (\gamma^2 - \omega^2 {c_L}^{-2})^{\frac{1}{2}} x_2} d\gamma \tag{3.63}$$

$$I_{u22} = \frac{-1}{\pi}\int_{-\infty}^{\infty} \frac{\gamma^2(\gamma^2 - \omega^2 {c_L}^{-2})^{\frac{1}{2}}}{\mathcal{H}(\gamma)} e^{-i\gamma x_1 - (\gamma^2 - \omega^2 {c_T}^{-2})^{\frac{1}{2}} x_2} d\gamma \tag{3.64}$$

The problem now falls to the evaluation of the integrals in equations 3.61 to 3.64 by contour integration. A contour integral describes a line integral in the complex plane. Evaluation of such integrals is achievable by the fact that, for an analytic function as

determined by the Cauchy-Reimann equations, the line integral of any closed loop on the complex plane is equal to zero. For the example at hand, there exists discrete points in the function that are not analytic, these are the poles that occur when $\mathcal{H}(\gamma) = 0$ in equations 3.61-64. Such points can usually be accounted for by computing the residual, as is common practise. However, in the current case, such computations are difficult and additional methods are required [39]. Full detail of the computation of the integrals in equations 3.61-64 is off-topic for the current discussion and will add little. Details of the computations can be found in references [51], [52]. The solutions relating to the surface waves, found in references [39], [40], [53] are quoted here.

$$u_{1_{x_2=0}} = -\frac{P}{\mu_L}\mathrm{K}_1 e^{i(\omega t-\gamma x_1)} \tag{3.65}$$

$$u_{2_{x_2=0}} = -\frac{iP}{\mu_L}\mathrm{K}_2 e^{i(\omega t-\gamma x_1)} \tag{3.66}$$

$$\mathrm{K}_1 = \frac{-\omega^3 c_R\left(2{c_R}^2 - {c_T}^2 - 2({c_R}^2 - {c_L}^2)^{\frac{1}{2}}({c_R}^2 - {c_T}^2)^{\frac{1}{2}}\right)}{\mathcal{H}'(\omega c_R)} \tag{3.67}$$

$$\mathrm{K}_2 = \frac{-\omega^3 {c_T}^2({c_R}^2 - {c_L}^2)^{\frac{1}{2}}}{\mathcal{H}'(\omega c_R)} \tag{3.68}$$

$$\mathcal{H}'(\omega c_R) = \left.\frac{d\mathcal{H}(\gamma)}{d\gamma}\right|_{\gamma=\omega c_R} \tag{3.69}$$

With reference to the reduced one-dimensional representation given in eq. 3.32, this solution would be represented as in equations 3.70-72.

$$\varphi_1(x_2) = \mathrm{K}_1 \tag{3.70}$$

$$\varphi_2(x_2) = i\mathrm{K}_2 \tag{3.71}$$

$$\psi(x_1, t) = -\frac{P}{\mu_L}e^{i(\omega t-\gamma x_1)} \tag{3.72}$$

3.3.2 The Interdigitated Transducer (IDT)

Transduction of surface acoustic waves in a piezoelectric substrate is efficiently accomplished by the use of interdigitated transducers. The basic geometry, as shown in Figure 3.3, consists of two parallel bus bars with electrode 'digits' protruding perpendicular to both the bus bars and the direction of wave travel. In the simplest arrangement alternating electrodes attach to alternating bus bars. An alternating current is applied across the two bus bars which in turn excites an alternating stress field in the substrate through the reverse piezoelectric effect.

Piezoelectricity is the accumulation of charge in a solid, and hence a voltage, through the application of a mechanical stress. Conversely, the reverse piezoelectric effect is the generation of a mechanical stress, due to the application of an electric field. With reference to Figure 3.3, through the reverse piezoelectric effect, the field lines in the substrate are directly related to a stress (and hence strain) within the substrate. The magnitude of this effect is described through the equations of linear piezoelectricity and in particular the constitutive equations coupling the stress and charge fields. The piezoelectric constitutive equations are shown in equations 3.73-74 [54].

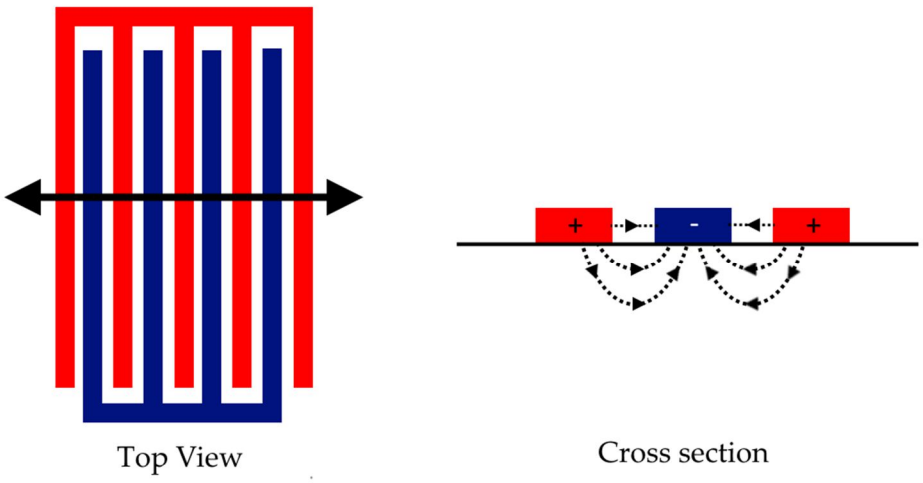

Figure 3.3 Top view and cross section of the basic interdigitated transducer geometry. The double headed arrow on the top view representation displays the direction of wave propagation. The dotted arrow lines on the cross section represent the field lines between the electrodes.

$$\underline{D} = \mathbf{e}\underline{E} + \mathbf{d}\underline{\tau} \tag{3.73}$$

$$\underline{\tau} = -(\mathbf{dC})^{\mathbf{T}}\underline{E} + \mathbf{C}\underline{\varepsilon} \tag{3.74}$$

Where $\mathbf{d}$ is the piezoelectric coefficient matrix, $\underline{D}$ is the charge density vector, $\mathbf{e}$ is the dielectic permittivity matrix, $\underline{E}$ is the electric field vector, $\mathbf{C}$ is the elasticity matrix, $\underline{\tau}$ is the stress vector and $\underline{\varepsilon}$ is the strain vector**.** It can be seen that if one knows the piezoelectric coefficient matrix for a material and the applied electric field, then the resultant mechanical loading on the material can be found.

For device design, transduction using an IDT is typically modelled using phenomenological equations, such as in the coupling of modes method (COM). A transduction coefficient is found, through experiment or simulation, for a material. This is used within a reduced order model to directly couple the voltage directly to the wave amplitude [46].

The simplest model for IDT design is the delta function model [55], [56]. This is widely used, and although simplistic, can produce useful results. As displayed in Figure 3.4 it represents the IDT excitation as a series of delta functions. Commonly these are located two per IDT finger, one at each edge. However, it is stated in reference [56] that this can be simplified to one per IDT finger, located in the centre, with little loss of information, as depicted in Figure 3.5.

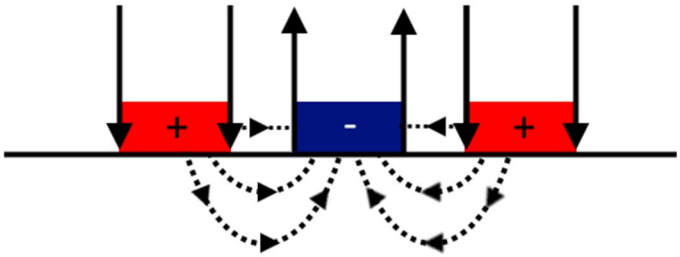

Figure 3.4 Schematic of the delta function representation of IDT forcing.

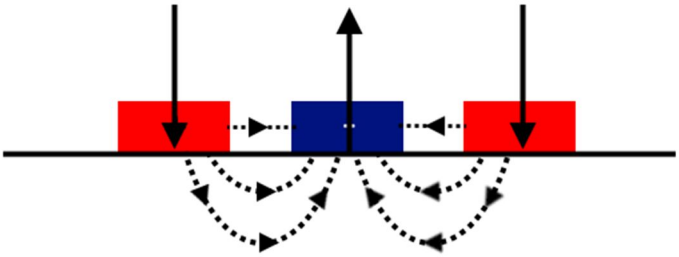

Figure 3.5 Schematic of the reduced delta function model.

In the device discussed within this thesis, an IDT will sit adjacent to each cavity, injecting waves into the device. On the other side of the IDT will lie the reflector array, bounding the device (see Figure 2.1). The analysis presented here will simplify each IDT to be represented by a single line load of the type presented in Figure 3.5. The simplification is displayed graphically in Figure 3.6.

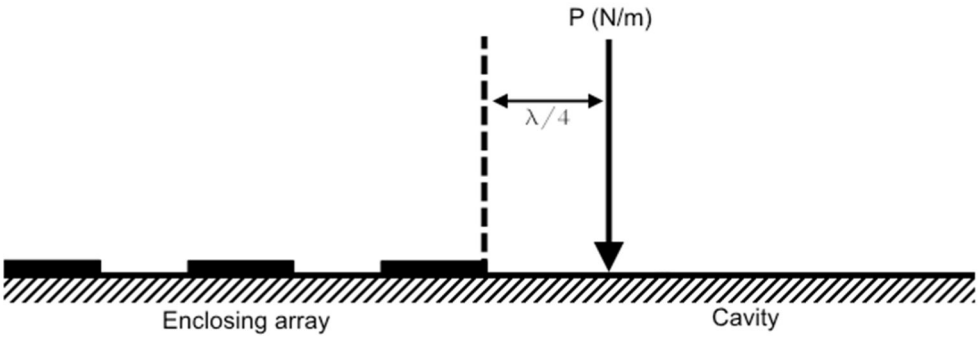

Figure 3.6 Positioning of the single line load in relation to the enclosing array and cavity.

3.4 The transfer matrix for locally periodic media

The transfer matrix for locally periodic media has been found in references [14], [15], [17]. This is to be used to provide the change in amplitude and phase for a reflected or transmitted wave incident upon an array. Contrary to many transfer matrix methods, this makes no reference to Floquet or Bloch theory; instead it finds closed form solutions for the recursive application of the single cell transfer matrix. Consequently it is valid for any length of repeating structure, unlike the Floquet-Bloch methods, which are rigorously valid only for infinite periodic arrays [12], [14], [15]. For completeness and because of its central role in the solutions yielded later in this chapter, the derivation and solutions yielded by Griffiths and Steinke [14] and Pereyra and Castillo [15] are

transcribed here in the context of the SAW system. A schematic of a general array geometry is presented in Figure 3.7.

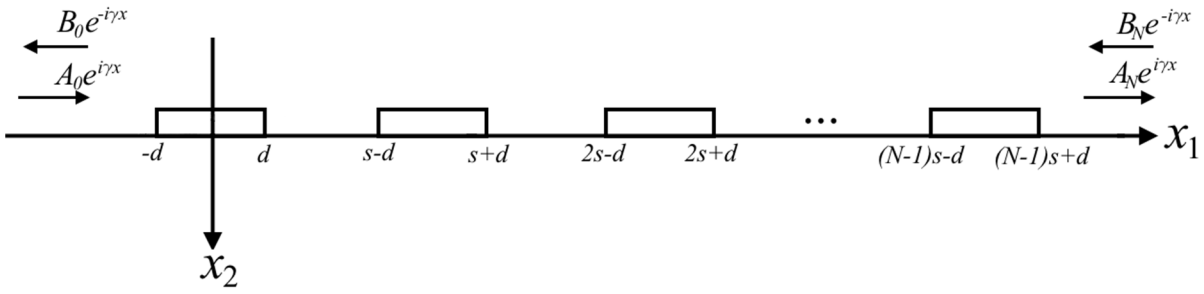

Figure 3.7 Schematic and coordinate system for derivation of the TM

It can be seen that each period consists of three regions and that there are two internal boundaries per period. The incident wave is described by equation 3.75. The waves in the subsequent plated and un-plated regions are then described by equations 3.76 and 3.77 respectively.

$$\psi_0(x_1) = A_0e^{i\gamma x_1} + B_0e^{-i\gamma x_1} \quad x_1 < -d \tag{3.75}$$

$$\overline{\psi_n}(x_1) = \overline{A_n}e^{i\overline{\gamma}(x_1-ns)} + \overline{B_n}e^{-i\overline{\gamma}(x_1-ns)} \quad -d + (n-1)s < x_1 < d + (n-1)s \tag{3.76}$$

$$\psi_n(x_1) = A_ne^{i\gamma(x_1-ns)} + B_ne^{-i\gamma(x_1-ns)} \quad d + (n-1)s < x_1 < -d + ns \tag{3.77}$$

The 'state vector', $\underline{\psi_n}(x_1)$, contains information on the displacement and its derivative at a point in the structure (equation 3.78). This information can be represented as the product of an amplitude vector, a phase matrix and a matrix representing the differential operation on the displacement. These are shown in equations 3.79, 3.80 and 3.81 respectively, for the un-plated regions.

$$\underline{\psi_n}(x_1) = \begin{Bmatrix} A_ne^{i\gamma x_1} + B_ne^{-i\gamma x_1} \\ i\gamma\left(A_ne^{i\gamma x_1} - B_ne^{-i\gamma x_1}\right) \end{Bmatrix} = \mathbf{D}.\mathbf{P}(x_1)\underline{\phi_n} \tag{3.78}$$

$$\underline{\phi_n} = \begin{Bmatrix} A_n \\ B_n \end{Bmatrix} \tag{3.79}$$

$$\mathbf{P}(x_1) = \begin{bmatrix} e^{i\gamma x_1} & 0 \\ 0 & e^{-i\gamma x_1} \end{bmatrix} \tag{3.80}$$

$$\mathbf{D} = \begin{bmatrix} 1 & 1 \\ i\gamma & -i\gamma \end{bmatrix} \tag{3.81}$$

With this terminology prescribed, the transfer matrix can be formulated. Referring to Figure 3.7, the transfer matrix from region ψ_0 to region ψ_1 will first be constructed. Considering first the boundary at $x_1 = -d$, continuity of the state vectors must be enforced; this results in equations 3.82-84.

$$\underline{\psi_0}(-d) = \overline{\underline{\psi_0}}(-d) \tag{3.82}$$

$$\mathbf{D}.\mathbf{P}(-d)\underline{\phi_0} = \overline{\mathbf{D}}.\overline{\mathbf{P}}(-d)\overline{\underline{\phi_0}} \tag{3.83}$$

$$\underline{\phi_0} = \mathbf{D^{-1}}.\mathbf{P^{-1}}(-d).\overline{\mathbf{D}}.\overline{\mathbf{P}}(-d)\overline{\underline{\phi_0}} \tag{3.84}$$

And identically, when considering the boundary at $x_1 = d$.

$$\overline{\underline{\psi_0}}(d) = \underline{\psi_0}(d) \tag{3.85}$$

$$\overline{\mathbf{D}}.\overline{\mathbf{P}}(d)\overline{\underline{\phi_0}} = \mathbf{D}.\mathbf{P}(d)\underline{\phi_1} \tag{3.86}$$

$$\overline{\underline{\phi_0}} = \overline{\mathbf{D}}^{-1}.\overline{\mathbf{P}}^{-1}(d).\mathbf{D}.\mathbf{P}(d)\underline{\phi_1} \tag{3.87}$$

Substituting 3.87 into 3.84 gives equation 3.88.

$$\underline{\phi_0} = \mathbf{D^{-1}}.\mathbf{P^{-1}}(-d).\overline{\mathbf{D}}.\overline{\mathbf{P}}(-d)\overline{\mathbf{D}}^{-1}.\overline{\mathbf{P}}^{-1}(d).\mathbf{D}.\mathbf{P}(d)\underline{\phi_1} \tag{3.88}$$

Evaluation of the matrix product yields the transfer matrix across one period of the array. Therefore, equation 3.88 is expressed at equations 3.89-91.

$$\underline{\phi_0} = \mathbf{T}\underline{\phi_1} \tag{3.89}$$

$$\begin{Bmatrix} A_0 \\ B_0 \end{Bmatrix} = \mathbf{T}\begin{Bmatrix} A_1 \\ B_1 \end{Bmatrix} \tag{3.90}$$

$$\mathbf{T} = \mathbf{D^{-1}}.\mathbf{P^{-1}}(-d).\overline{\mathbf{D}}.\overline{\mathbf{P}}(-d)\overline{\mathbf{D}}^{-1}.\overline{\mathbf{P}}^{-1}(d).\mathbf{D}.\mathbf{P}(d) \tag{3.91}$$

Once $\mathbf{T}$ is evaluated it is found to be hermitian with the components as given below in equations 3.92-95.

$$\mathbf{T} = \begin{bmatrix} w & z \\ z^* & w^* \end{bmatrix} \tag{3.92}$$

$$w = (Cos(2\overline{\gamma}d) - i\epsilon_{+}Sin(2\overline{\gamma}d))e^{2i\gamma d} \tag{3.93}$$

$$z = i\epsilon_{-}Sin(2\overline{\gamma}d) \tag{3.94}$$

$$\epsilon_{\pm} = \frac{1}{2}\left(\frac{\gamma}{\overline{\gamma}} \pm \frac{\overline{\gamma}}{\gamma}\right) \tag{3.95}$$

It is explained in references [14], [15] that the form of the transfer matrix is enforced due to the physical laws of time reversal invariance and conservation of energy. The transfer matrix takes this form for any distribution of wavenumber. In addition, it is shown that the transfer matrix is unimodular, that is,$|\mathbf{T}| = \mathbf{1}$. These properties are employed to apply the transfer matrix recursively. The relationship between the n^{th} un-plated region to the $(n+1)^{th}$ un-plated region can be written from equations 3.96.

$$\begin{Bmatrix} A_n e^{i\gamma(x_1 - ns)} \\ B_n e^{-i\gamma(x_1 - ns)} \end{Bmatrix} = \mathbf{T}\begin{Bmatrix} A_{n+1} e^{i\gamma(x_1 - (n+1)s)} \\ B_{n+1} e^{-i\gamma(x_1 - (n+1)s)} \end{Bmatrix} \tag{3.96}$$

This simplifies to equations 3.97-98.

$$\begin{Bmatrix} A_n \\ B_n \end{Bmatrix} = \mathbf{T}\begin{Bmatrix} A_{n+1} e^{-i\gamma s} \\ B_{n+1} e^{i\gamma s} \end{Bmatrix} = \mathbf{T}.\mathbf{P}(-s)\begin{Bmatrix} A_{n+1} \\ B_{n+1} \end{Bmatrix} = \mathbf{Z}\begin{Bmatrix} A_{n+1} \\ B_{n+1} \end{Bmatrix} \tag{3.97}$$

$$\mathbf{Z} = \begin{bmatrix} we^{-i\gamma s} & ze^{i\gamma s} \\ z^* e^{-i\gamma s} & w^* e^{i\gamma s} \end{bmatrix} \tag{3.98}$$

Applying $\mathbf{Z}$ recursively can provide the transfer matrix for N periods (equation 3.99).

$$\begin{Bmatrix} A_0 \\ B_0 \end{Bmatrix} = \mathbf{Z}^N \begin{Bmatrix} A_N \\ B_N \end{Bmatrix} \tag{3.99}$$

The problem is now reduced to the evaluation of $\mathbf{Z}^N$, the N^{th} power of a unimodular, hermitian matrix. This is performed in references [14], [15] by exploiting the Cayley-Hamilton theorem. The method is detailed here. First the characteristic equation of $\mathbf{Z}$ is considered.

$$|\mathbf{Z} - m.\mathbf{I}| = m^2 - m\,Tr(\mathbf{Z}) + |\mathbf{Z}| = 0 \tag{3.100}$$

Using the fact that $\mathbf{Z}$ is unimodular, this reduces to equation 3.101, where m is a scalar.

$$m^2 - 2\zeta m + 1 = 0 \tag{3.101}$$

$$\zeta = \frac{1}{2} Tr(\mathbf{Z}) \tag{3.102}$$

The Cayley-Hamilton theorem states that any matrix will satisfy its own characteristic equation[14], [15],therefore m can be set as equal to **Z.**

$$\mathbf{Z}^2 - 2\zeta \mathbf{Z} + \mathbf{I} = 0 \tag{3.103}$$

This implies that any power of **Z** can be written as a linear combination of **Z** and **I**. This can be reasoned by first rearranging eq. 3.103 to an expression for $\mathbf{Z}^2$, and then multiply through by **Z**, providing an equation for $\mathbf{Z}^3$ in terms of $\mathbf{Z}^2$ and **Z**. The original equation (eq.3.103) for $\mathbf{Z}^2$ can be substituted back in, providing a linear expression for $\mathbf{Z}^3$, in terms of **Z** and **I**. This process can be repeated for any power of **Z**, thus eq, 3.103 can be written as below.

$$\mathbf{Z}^N = \mathbf{Z}.U_{N-1}(\zeta) - \mathbf{I}.U_{N-2}(\zeta) \tag{3.104}$$

It is shown in references [14], [15] that the polynomial $U_N(\zeta)$ is the N^{th} Chebyshev polynomial of the second kind. This can be expressed explicitly as in eq 3.105.

$$U_N(\zeta) = \frac{Sin[(N+1)Cos^{-1}(\zeta)]}{Sin[Cos^{-1}(\zeta)]} \tag{3.105}$$

Therefore, finally the transfer matrix for the N cell array can be stated explicitly in equation 3.106.

$$\mathbf{Z}^N = \begin{bmatrix} we^{-i\gamma s}U_{N-1}(\zeta) - U_{N-2}(\zeta) & zU_{N-1}(\zeta)e^{i\gamma s} \\ z^*U_{N-1}(\zeta)e^{-i\gamma s} & w^*e^{i\gamma s}U_{N-1}(\zeta) - U_{N-2}(\zeta) \end{bmatrix} \tag{3.106}$$

Therefore the complex amplitudes of the transmitted and reflected portions of a wave incident on the left hand end of the array, can be stated as equations 3.107 and 3.108 respectively.

$$T_N = \left(\frac{A_N}{A_0}\right)_{B_N=0} = \left(we^{-i\gamma s}U_{N-1}(\zeta) - U_{N-2}(\zeta)\right)^{-1} \tag{3.107}$$

$$R_N = \left(\frac{B_0}{A_0}\right)_{B_N=0} = z^* U_{N-1}(\zeta) e^{-i\gamma s}\left(we^{-i\gamma s}U_{N-1}(\zeta) - U_{N-2}(\zeta)\right)^{-1} \tag{3.108}$$

For the purposes of the analysis presented within this thesis, a negative phase shift equal to one of the un-plated regions in the array is applied to equations 3.107 and 3.108. This is to account for the termination of the cavity at the end of the last plated region, as will be defined in the model in the following section. The necessity of this phase shift is depicted in Figure 3.8.

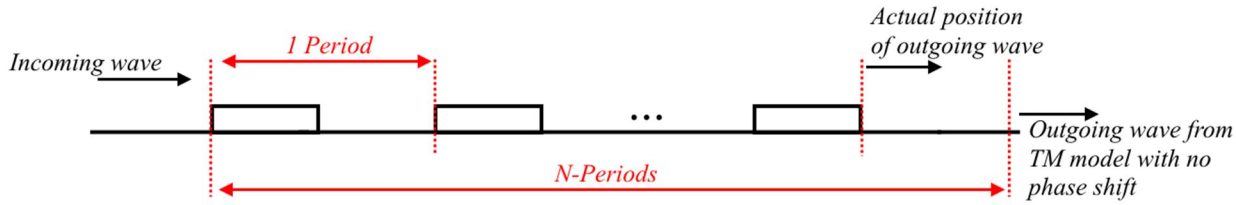

Figure 3.8 Illustration of reason for phase shift

After the application of the phase shift the expressions of equations 3.107 and 3.108 are non-dimensionalised and shown in equations 3.109-114.

$$\widetilde{T_N} = \left(\tilde{w}e^{-i\pi\tilde{\Omega}}U_{N-1}(\tilde{\zeta}) - U_{N-2}(\tilde{\zeta})\right)^{-1} e^{-i\pi r\tilde{\Omega}} \tag{3.109}$$

$$\widetilde{R_N} = \tilde{z}^*\, U_{N-1}(\tilde{\zeta})\left(\tilde{w}e^{-i\pi\tilde{\Omega}}U_{N-1}(\tilde{\zeta}) - U_{N-2}(\tilde{\zeta})\right)^{-1} e^{-i\pi r\tilde{\Omega}} \tag{3.110}$$

$$\tilde{z} = -i\epsilon_{-} Sin\left(\frac{\pi r\tilde{\Omega}}{\widetilde{c_R}}\right) \tag{3.111}$$

$$\tilde{w} = \left(Cos\left(\frac{\pi r\tilde{\Omega}}{\widetilde{c_R}}\right) - i\epsilon_{+} Sin\left(\frac{\pi r\tilde{\Omega}}{\widetilde{c_R}}\right)\right) e^{i\pi r\tilde{\Omega}} \tag{3.112}$$

$$\tilde{\zeta} = Re(\tilde{w})Cos(\pi\tilde{\Omega}) + Im(\tilde{w})Sin(\pi\tilde{\Omega}) \tag{3.113}$$

$$\epsilon_{\pm} = \frac{1}{2}\left(\widetilde{c_R} \pm \frac{1}{\widetilde{c_R}}\right) \tag{3.114}$$

The non-dimensional parameters used are defined in equations 3.115-3.118.

$$\widetilde{\Omega} = \frac{2sf}{c_R} \qquad (3.115)$$

$$\widetilde{c_R} = \frac{\overline{c_R}}{c_R} \qquad (3.116)$$

$$\tilde{s} = \frac{sf}{c_R} \qquad (3.117)$$

$$r = \frac{d}{s} \qquad (3.118)$$

Where f is the operating frequency, c_R is the substrate Rayleigh wave-speed, $\overline{c_R}$ is the Rayleigh wave-speed within the plated regions. The relationship between the period within the array and the incident wavelength, λ_i, is therefore $\lambda_i = 2s/\widetilde{\Omega}$.

A representative plot of the frequency dependence of the transmission and reflection amplitude coefficients is shown in Figure 3.9. The stop band can be seen clearly on both plots, emerging as a dip in the transmission coefficient spectrum. With increasing periods it is shown that the transmitted amplitude moves towards zero. Within the pass bands, peaks occur that relate to the position of the resonant frequencies of the structure if it was finite. It is shown in reference [14], [15] that as the number of periods grows towards infinity the pass band response tends towards a straight line.

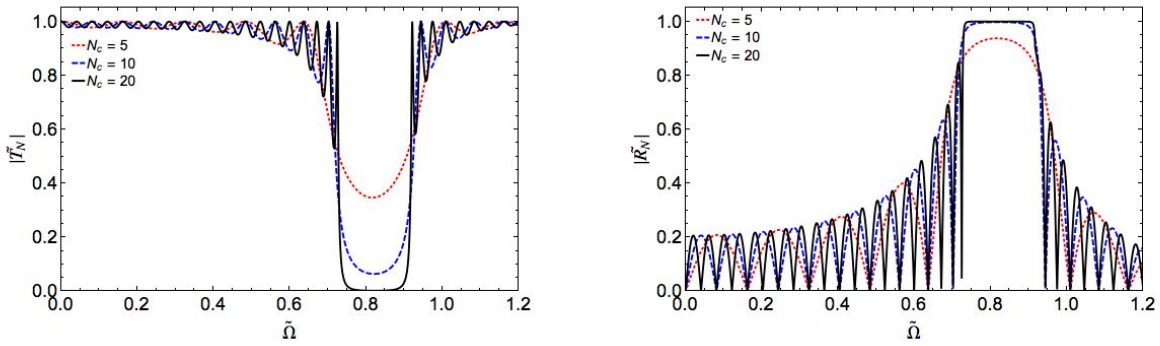

Figure 3.9 Transmission and reflection coefficients.

3.5 Generalised solution of the reduced one-dimensional problem

This section utilises the results from the literature presented previously in this chapter and combines them in a novel way. The analysis yields a closed form analytical solution for the displacement fields within the each cavity of the SAW system. To the author's knowledge, this is the first example of such a solution in the literature.

3.5.1 Solution of cavity displacement fields

A schematic of the device is shown in Figure 3.10, it can be seen that five main sections define the device: the two cavities and the three arrays. In the general case, excitation can occur in either cavity, or both cavities. Regardless of the excitation method, one cavity is deemed the reference and the other the sense cavity.

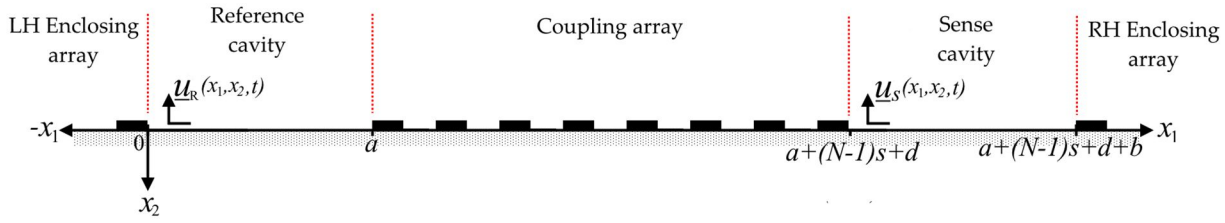

Figure 3.10 Device schematic

The transmission and reflection due to the arrays has been defined by the transfer matrix solution of the preceding section. Therefore, these can now each be represented as a single boundary, simplifying the representation of the device (Figure 3.11).

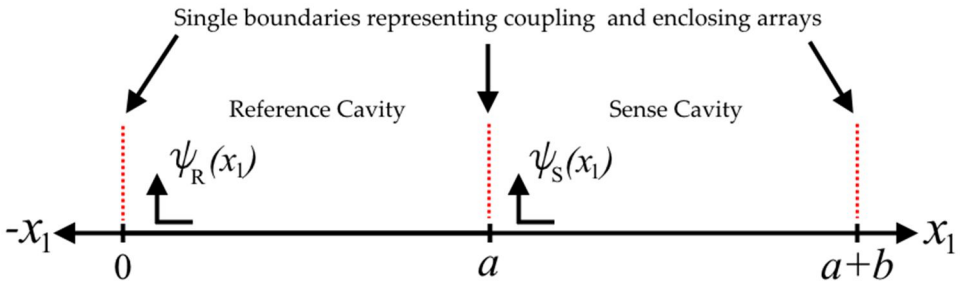

Figure 3.11 Reduced schematic in which he coupling array is replaced with a single boundary at point 'a'. This point represents both the right hand end of the reference cavity and the left hand end of the sense cavity.

The free-wave solution in the cavities was described in sections 3.2.2-3.2.4 and the forced solution of a semi-infinite half-space was found in section 3.31. Within this section the forced response of the two coupled cavities will be found utilising a ray tracing method. In a manufactured device, transduction would be realised using an IDT. As previously described, to simplify and approximate this forcing type, an IDT will be represented as single delta function source. This will radiate a sinusoid in either direction. The displacement fields in a forced and un-forced cavity, neglecting reflections, are defined in equations 3.119-3.121, where x_F is the location of the source.

$$\psi_F(x_1)_{x_1<x_F} = F_L e^{-i\gamma x_1} \tag{3.119}$$

$$\psi_F(x_1)_{x_1>x_F} = F_R e^{i\gamma x_1} \tag{3.120}$$

$$\psi_{UF}(x_1) = Ae^{i\gamma x_1} + Be^{-i\gamma x_1} \tag{3.121}$$

It can be seen that the field within the sense and forcing cavities will be described by the sum of a leftwards and a rightwards propagating wave, the amplitudes of which are to be determined.

The physics of this solution are such that there is both a leftward and rightward propagating plane wave originating at each forcing location. With reference to the schematic in Figure 3.10, it can be seen that each of these will propagate until they reach either an enclosing array or the coupling array. Upon reaching an array, the wave will be partially transmitted and partially reflected. The reflected portion of the wave will then traverse the same cavity again before undergoing partial reflection/transmission at the opposing boundary. The transmitted portion will either propagate away from the structure or traverse the neighbouring cavity, dependent on which array it is incident upon. This will continue in a manner demonstrated by Figure 3.12,

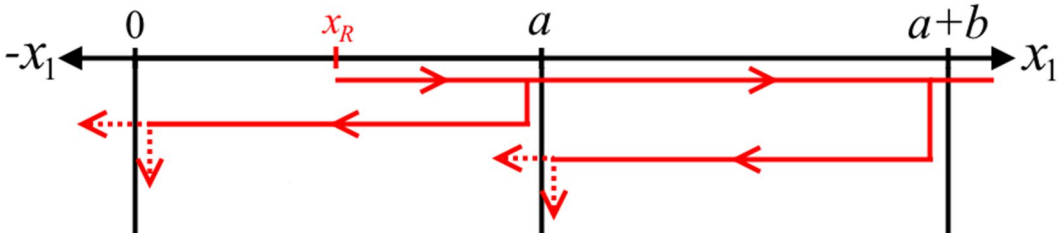

Figure 3.12 Illustration of path taken in initial stages of wave propagation.

Following this reasoning allows for the construction of the solutions within the cavities. It is clear however, that the solutions will be fairly extensive considering the multiple reflections to be accounted for. However, it can be simplified somewhat by noticing that there are only three unique paths any wave can traverse before arriving back at its starting point. These will be termed the 'fundamental paths' and are (a) internal reflection within the reference cavity, (b) internal reflection traversing both cavities and (c) internal reflection within the sense cavity. These are depicted in Figure 3.13.

Considering a wave propagating away from any boundary, any future wave originating at the same boundary due to that wave is made up of the product of the original wave and some combination of these paths.

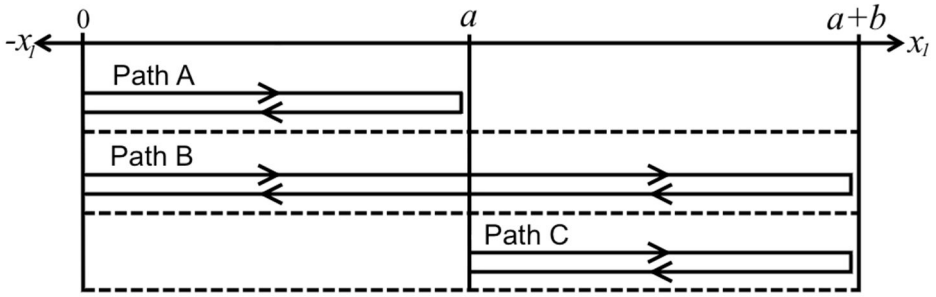

Figure 3.13 Loci of the fundamental reflection paths.

Each path is represented mathematically by a phase change due to distance travelled, and a complex amplitude coefficient due to the partial reflections and transmissions. The expressions for the paths are given in equations 3.122-124, each path expression will be denoted as χ_α.

$$Path\ A = \chi_A = R_R R_C e^{i2\gamma a} \tag{3.122}$$

$$Path\ B = \chi_B = R_S {T_C}^2 R_R e^{i2\gamma(a+\eta b)} \tag{3.123}$$

$$Path\ C = \chi_C = R_S R_C e^{i2\eta\gamma b} \tag{3.124}$$

Where R_R and R_S are the reflection coefficients for the enclosing arrays of the reference and sense cavities respectively. T_C and R_C are the transmission and reflection coefficients of the coupling array and $\eta = \gamma_{SENSE}/\gamma$.

The solution within each cavity can therefore be said to be some product of the initial waves at each of its boundaries and a combination of the path expressions. The initial waves are defined as the excited or reflected waves that have not yet traversed one full fundamental path. These are most easily found by graphically tracing the initial propagation stages. Figure 3.14 shows the first stages of wave propagation, up until each ray has travelled 3 cavity lengths in distance, only the unique initial waves are displayed.

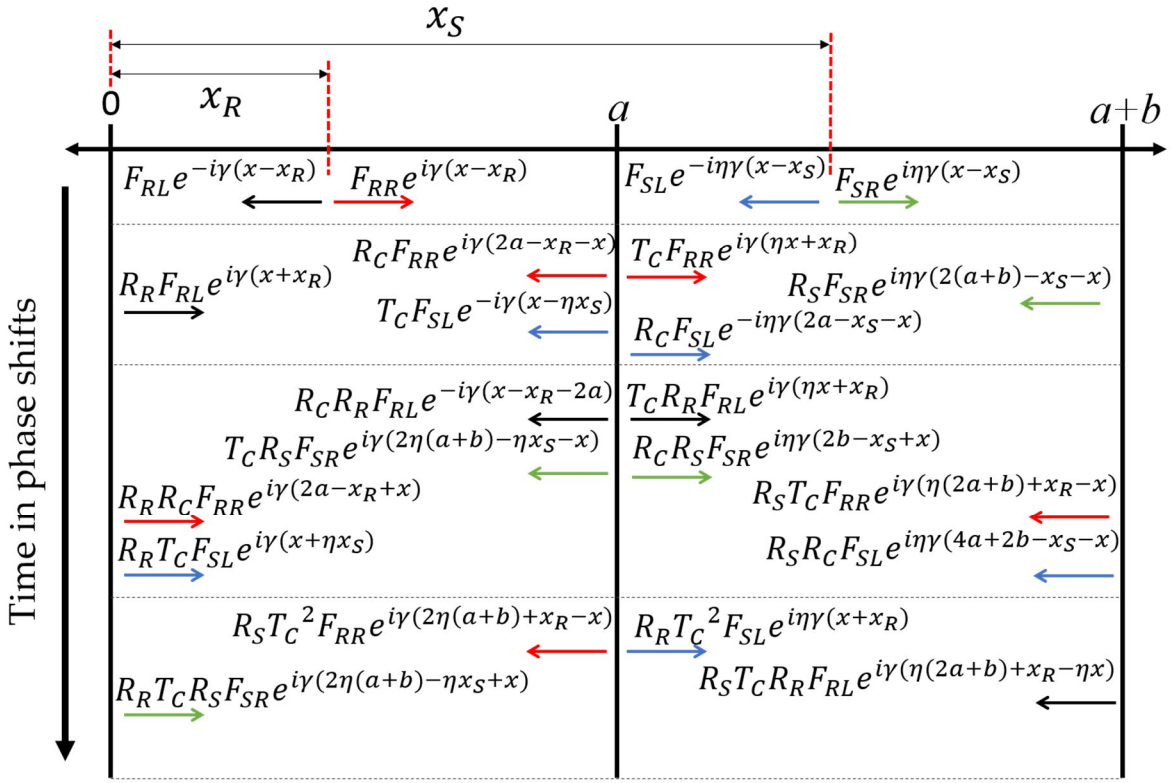

Figure 3.14 Graphical ray tracing method used to define the initial waves that multiply the infinite summations. The x-axis represents the cavity distance in the device and the y-axis is the time in phase shifts. The waves are collected vertically into initial wave

Three path expression combinations (PECs) can be defined. These represent every possible combination of routes an initial wave can take as it is repeatedly internally reflected and transmitted between the two cavities along the fundamental paths. These take the forms shown in equations 3.125-127.

$$\Gamma = \sum_{i=0}^{\infty}\sum_{j=0}^{\infty}\sum_{k=0}^{\infty}\left(\frac{(i+j)!}{i!\,j!}\right)\left(\frac{(j+k)!}{j!\,k!}\right){\chi_A}^i{\chi_B}^j{\chi_C}^k \tag{3.125}$$

$$\Gamma_R = \sum_{i=0}^{\infty}\sum_{j=0}^{\infty}\sum_{k=0}^{\infty}\left(\frac{(i+j)!}{i!\,j!}\right)\left(\frac{(j+k)!}{j!\,k!}-\frac{(j+k-1)!}{j!\,(k-1)!}\right){\chi_A}^i{\chi_B}^j{\chi_C}^k \tag{3.126}$$

$$\Gamma_S = \sum_{i=0}^{\infty}\sum_{j=0}^{\infty}\sum_{k=0}^{\infty}\left(\frac{(i+j)!}{i!\,j!}-\frac{(i+j-1)!}{i!\,(j-1)!}\right)\left(\frac{(j+k)!}{j!\,k!}\right){\chi_A}^i{\chi_B}^j{\chi_C}^k \tag{3.127}$$

Equation 3.125 is the sum of every possible combination of the three fundamental paths. Equation 3.126 is necessary for waves that originate from excitation within the

reference cavity. Equation 3.126 is the same as Equation 3.125 less all combinations in which path χ_C occurs before at least one incidence of path χ_B. The initial waves cannot traverse path χ_C without this path occurring after path χ_B has begun. In other words, this enforces the requirement that reflections within the sense cavity can only occur post-transmission across the coupling array. The same reasoning is used for equation 3.127; however, in relation to initial waves due to an excitation in the sense cavity.

It is of note that the path expressions have all been placed within an infinite sum. This is due to the fact that, neglecting damping effects, the waves will repeat each reflection and transmission pattern indefinitely. It is necessary to simplify the expressions so that they can be analytically inspected and numerically evaluated. The summations are combinations of infinite arithmetico-geometric progressions. These can be evaluated using equation 3.128.

$$\sum_{n=0}^{\infty} \frac{(n+m-1)!}{n!} {\chi_\alpha}^n = \frac{(m-1)!}{(1-\chi_\alpha)^m} \qquad for\ m = 1, 2, 3 \ldots \tag{3.128}$$

Utilising linear combinations of equation 3.128 equations 3.125-127 simplify to equations 3.129-131 respectively.

$$\Gamma = \Lambda^{-1} \tag{3.129}$$

$$\Gamma_R = (1-\chi_C)\Lambda^{-1} \tag{3.130}$$

$$\Gamma_S = (1-\chi_A)\Lambda^{-1} \tag{3.131}$$

$$\Lambda = 1 - \chi_A - \chi_B - \chi_C + \chi_A\chi_C \tag{3.132}$$

This result of equations 3.129-132 is of particular significance to the current work. The reduction of equations 3.125-127 to simple, finite, exact expressions enables numerical simulation of the problem to become practical. Depending on the parameters chosen, between 500-1000 terms in the summations of equation 3.125 are required to provide an accurate representation of the frequency response. In equation 3.132, the same

function is described by only 5 terms. The utility of this reduction with regards to numerical modelling will be discussed in more detail in chapter 4.

It can be seen that the path expression products share a common denominator, Λ. As one of the PECs multiply every initial wave, the roots of Λ can be used to find the conditions for resonance.

The amplitude and phase of the leftward and rightward propagating waves are found for each cavity by summing the initial waves and multiplying them by their respective PEC. For the reference cavity, the rightward and leftward wave amplitudes are denoted as A_R and B_R respectively and are given in equations 3.133-134. In the following equations the first subscript of a variable refers to the cavity it is in reference to and the second subscript (where necessary) is in reference to the direction of travel. For example F_{RL} is the amplitude coefficient of the leftward travelling wave originating from the excitation source within the reference cavity.

$$A_R = \Lambda^{-1}\{(1-\chi_C)\big(F_{RR}e^{-i\gamma x_R} + R_R F_{RL} e^{i\gamma x_R}\big) + R_R T_C\big(F_{SL}e^{i\eta\gamma x_S} + R_S F_{SR} e^{i\gamma(2a+\eta(2b-x_S))}\big)\} \tag{3.133}$$

$$B_R = \Lambda^{-1}\{(1-\chi_C)\big(F_{RL}e^{i\gamma x_R} + R_C F_{RR} e^{i\gamma(2a-x_R)}\big) + T_C\big(F_{RL}e^{i\eta\gamma x_S} + R_S\big[F_{SR}e^{i\eta\gamma x_S} + T_C F_{RR} e^{i\gamma x_R}\big]e^{i2\gamma(a+\eta b)}\big)\} \tag{3.134}$$

Similarly, the rightward and leftward wave amplitudes for the sense cavity are given in equations 3.135 and 3.136 respectively.

$$A_S = \Lambda^{-1}\{(1-\chi_A)\big(F_{SR}e^{-i\eta\gamma x_S} + R_C F_{SL} e^{-i(2\gamma a-\eta\gamma x_S}\big) + T_C\big(e^{i\gamma x_R}[F_{SR} + R_R F_{RL}] + R_R T_C F_{SL} e^{i\eta\gamma x_S}\big)\} \tag{3.135}$$

$$B_S = \Lambda^{-1}\{(1-\chi_A)\big(F_{SL}e^{i\eta\gamma x_S} + R_S F_{SR} e^{i\gamma(2a+\eta(2b-x_S))}\big) + R_S T_C (F_{RR} + R_R F_{RL}) e^{i\gamma((2a+x_R)+2\eta b)}\} \tag{3.136}$$

The displacement fields in each cavity are therefore described by equations 3.137 and 3.138.

$$\psi_R(x) = \begin{cases} \big|A_R + |B_R - F_{RL}|e^{-i(\gamma x_R + \angle(B_R - F_{AL}))}\big|e^{i\gamma x} & x > x_R \\ \big|A_R + |B_R|e^{-i\angle B_R} - F_{RR}e^{-i\gamma x_R}\big|e^{i\gamma x} & x < x_R \end{cases} \tag{3.137}$$

$$\psi_S(x) = \begin{cases} \left|A_S + |B_S - F_{SL}|e^{-i(\eta\gamma x_S + \angle(B_S - F_{SL}))}\right| e^{i\eta\gamma x} & x > x_S \\ \left|A_S + |B_S|e^{-i\angle B_S} - |F_{SR}|e^{-i\eta\gamma x_S}\right| e^{i\eta\gamma x} & x < x_S \end{cases} \tag{3.138}$$

3.5.2 A special case

A special case of this solution can be written for the device currently under investigation. The excitation arrangement described by Figure 3.6 is asserted, and the response to a line load presented in section 3.3.1 is utilised. As the forcing is effectively located at the boundary, which is designed to be highly reflective, a simplifying assumption is made that all the excited energy initially propagates into the cavity. This scenario is described by the following substitutions.

$$F_{RR} = 2\,P_{REF}/\mu_L \tag{3.139}$$

$$F_{RL} = 0 \tag{3.140}$$

$$F_{SR} = 0 \tag{3.141}$$

$$F_{SL} = 2\,P_{SENSE}/\mu_L \tag{3.142}$$

$$x_R = \lambda/4 \tag{3.143}$$

$$x_S = a + b - \lambda/4 \tag{3.144}$$

Using the above substitutions and recalling that $\gamma = \omega/c_R$, the frequency response functions for the cavity amplitudes can be written as linear combinations of the contributions from each forcing location.

$$|\psi_S(\omega)| = |G_{\mathrm{SR}}(\omega)|P_{REF}(\omega) + |G_{\mathrm{SS}}(\omega)|P_{SENSE}(\omega) \tag{3.145}$$

$$G_{\mathrm{SR}}(\omega) = \frac{R_S T_C e^{i(2\gamma a + 2\eta\gamma b - \gamma x_R)}}{\mu_L(1 - \chi_A - \chi_B - \chi_C + \chi_A\chi_C)} \tag{3.146}$$

$$G_{\mathrm{SS}}(\omega) = \frac{(1 - \chi_A)e^{i\eta\gamma x_S}}{\mu_L(1 - \chi_A - \chi_B - \chi_C + \chi_A\chi_C)} \tag{3.147}$$

$$|\psi_R(\omega)| = |G_{\mathrm{RR}}(\omega)|P_{REF}(\omega) + |G_{\mathrm{RS}}(\omega)|P_{SENSE}(\omega) \tag{3.148}$$

$$G_{\mathrm{RR}}(\omega) = \frac{(1-\chi_C)e^{-i\gamma x_R}}{\mu_L(1-\chi_A-\chi_B-\chi_C+\chi_A\chi_C)} \tag{3.149}$$

$$G_{\mathrm{RS}}(\omega) = \frac{R_R T_C e^{i\eta\gamma x_S}}{\mu_L(1-\chi_A-\chi_B-\chi_C+\chi_A\chi_C)} \tag{3.150}$$

3.5.3 Incorporation of dissipation

This section will briefly address the incorporation of loss into the model. Further details of the specific physical mechanisms of loss and quantification will be addressed in chapter 5. The types of energy dissipation present in the system can be separated into two categories: radiative losses and viscous losses. One form of loss, radiation from the ends of the arrays, is already determined in the model by the reflection coefficients of the enclosing arrays. The effect of all other forms of loss will be included using a complex wavenumber. The general form of the wavenumber is given in equation 3.151.

$$\gamma = 2\pi/\lambda - i\alpha_L \tag{3.151}$$

Where α_L is an attenuation coefficient specified in Nepers/m. Substituting a wavenumber of this form into equations 3.137 and 3.138 can account for all dissipation that takes place within the cavities. However, this does not account for losses occurring whilst waves traverse the coupling array. To account for this, the transmission coefficient must be replaced by the 'lossy transmission coefficient' , T_{CL} ,defined in equation 3.152.

$$T_{CL} = e^{-\alpha_L L_{CA}} T_C \tag{3.152}$$

Where $L_{CA} = (N-1)s + 2d$ is the length of the coupling array.

3.6 Finite element model

An equivalent one-dimensional acoustic problem was constructed using Comsol Multiphysics in the Pressure Acoustics module. This amounts to a steady-state solution of a one-dimensional Helmholtz equation with variable parameters. In this case the variable parameter is the wave-speed, which is perturbed periodically in the arrays as well as uniformly across the sense cavity. This model will serve to validate the derived

displacement field expressions, with the use of the one-dimensional wave equation transfer matrix derived in section 3.4.

The geometry of the finite element model was simply a line split into sections reflecting the geometry shown in Figure 3.10. An overview of the 1D geometry, mesh and an example of the displacement field output is presented in Figures 3.15-3.19.

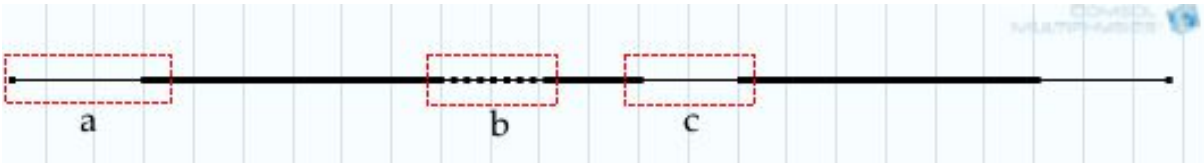

Figure 3.15 Full 1D geometry used in the finite element model. The reference and sense cavities are highlighted as 'b' and 'c' respectively. To the outside of the sense and reference cavities are the enclosing arrays and between cavities is the coupling array. Radiating boundary conditions were imposed at each end approximately 10 wavelengths from the end of the enclosing arrays.

Figure 3.16 Enlarged view of section 'a' highlighted in Figure 3.15. The end of the left-hand enclosing array is depicted along with the external region. The blue and black alternating regions in the array indicated sections of differing wave speed.

Figure 3.17 Enlarged view of section 'b' highlighted in Figure 3.15. The reference cavity is depicted with the regions of in-phase excitation highlighted in blue and the regions of out-of-phase excitation shown in black.

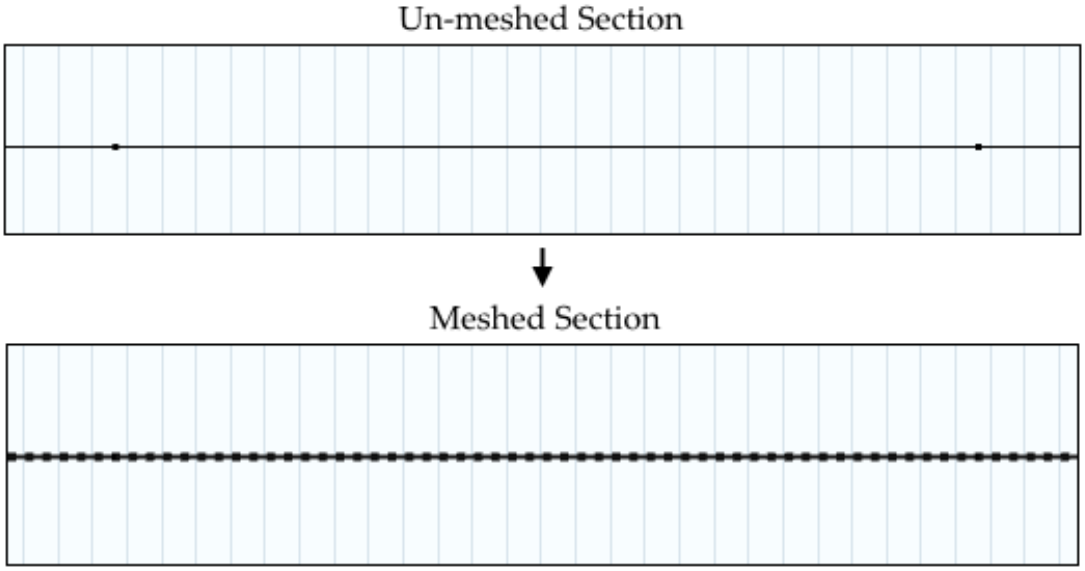

Figure 3.18 1D mesh of approximately 15 elements per wavelength.

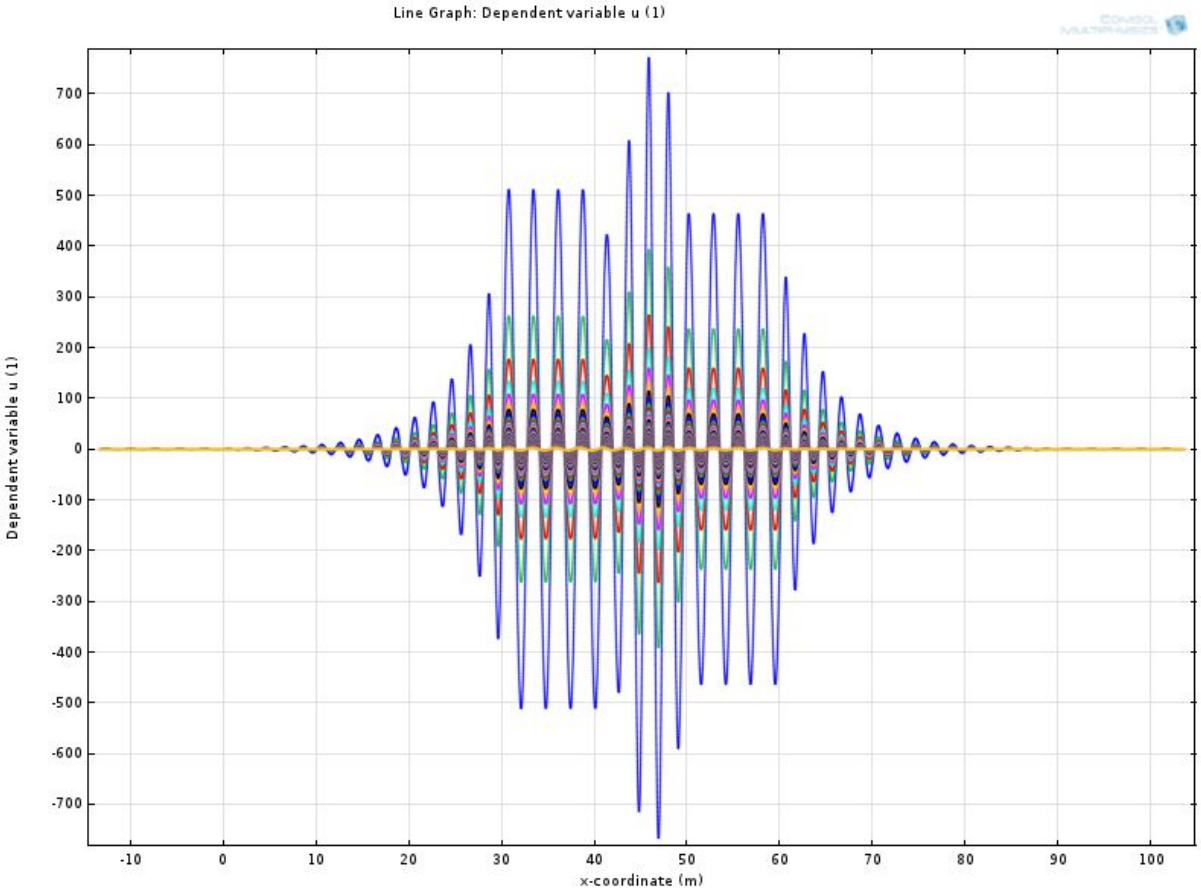

Figure 3.19 Example displacement field outputs from a sweep of the wave speed within the sense cavity.

In the frequency domain, each section was governed by equation 3.153. The parameter c was set equal to unity for all sections. Ω is the excitation frequency and v is the section wave-speed, which varied between sections according to Figure 3.10.

$$\nabla \cdot \left(-c\nabla u_1(x_1)\right) - \frac{\Omega^2}{v^2} u_1(x_1) = 0 \tag{3.153}$$

The length of the cavities was set to four wavelengths and the structure was terminated one wavelength after the enclosing arrays. Radiating boundary conditions were imposed at the terminations of the structure, as had been assumed in the analytical model. An excitation source was located in the centre of each cavity; a dipole acoustic source was selected, radiating two sinusoids of opposite phase in opposite directions, the amplitudes of which were tuned to unity. The numerical parameters were found from the non-dimensional parameters (equations 3.115-118) with s and v_1 also set equal to unity. With these parameter choices made, $\widetilde{\Omega} = 2f$. A mesh refinement investigation was performed, and due to the single dimension and simplicity of the model the critical parameter, cavity amplitude, was found to have negligible dependence on the mesh for meshes finer than 15 elements per wavelength.

3.7 Contrast of analytical and numerical solutions

Comparison to the FEM model is presented here as a means of validation of the model derived in section 3.5. In order to include all of the terms in the model, it will include excitation in both cavities. The comparison parameter will be the cavity amplitudes. This was evaluated from the FEM output as the maximum value within the displacement vector output from the respective cavity. The cavity amplitudes will be compared in terms of frequency response and variation of parameters η, x_R, x_S, a and $\widetilde{c_R}$. Both models use identical boundary conditions and forcing conditions. The frequency response and parameter dependence plots are shown in Figure 3.20. The plots depict the agreement between the two models.

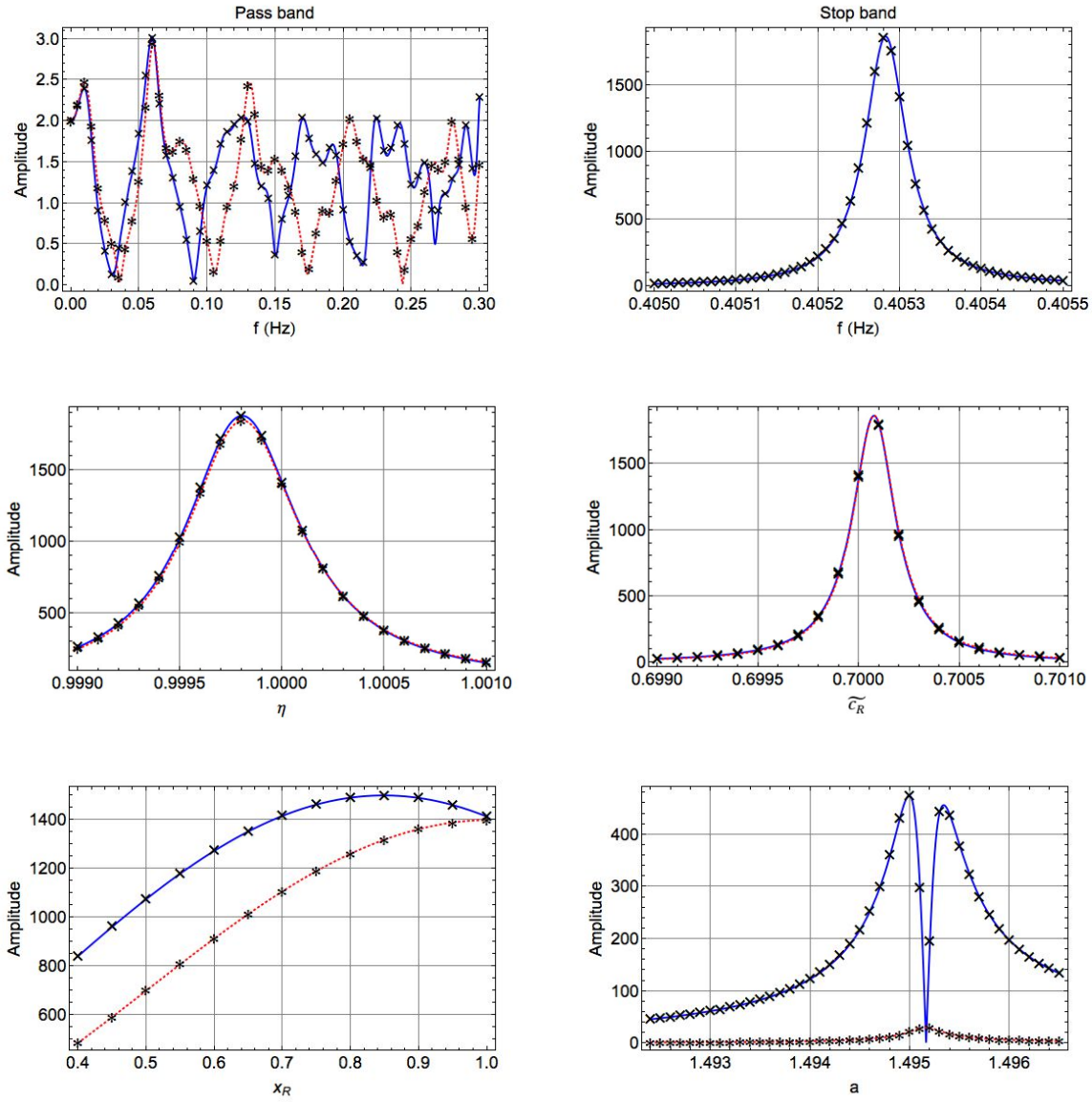

Figure 3.20 Validation plots showing cavity amplitudes expanded in various parameters. The full blue line depicts the sense cavity displacement amplitude and the dotted red line is that of the reference cavity. The plot markers represent data points from the FEM solution.

3.8 Discussion

3.8.1 Validity of the model to SAW devices: Reflection and transmission coefficients

The accuracy of the solution of section 3.5 for SAW devices is determined solely by the accuracy of the complex reflection and transmission coefficients. The remainder of the model is completely general and applicable to all types of linear plane wave motion, and has been validated in section 3.7. Much attention has been given to analytical determination of the transmission and reflection of SAW from periodic arrays. The

problem has been tackled successfully using variational methods [38], [43], perturbation methods [47]–[49], [53], [57] and most commonly by combining phenomenological methods with experimental or numerical results [46], [58]. This section serves to discuss the methods of determining the reflection and transmission coefficients. Once obtained, by whichever means, these can be substituted into the model, yielding accurate results for the device behaviour.

Within this chapter, and throughout the rest of this thesis, the reflection and transmission coefficients are determined using the transfer matrix of section 3.4. This form was found to be the most convenient and insightful for the current analysis. Additionally, this has been experimentally proven to provide accurate results in relation to SAW devices in references [17], [59]. However, the parameter $\widetilde{c_R}$ used to account for the wave speed mismatch in the two regions is usually determined to a higher accuracy from experiment.

An alternative to the TM method used here is the coupling of modes method (COM). Similarly to the method presented here, it assumes that surface waves can be described by a scalar wave equation and yields a transfer matrix of the same form as presented in section 3.4 [58]; however, rather than being presented purely in terms of the array parameters, the parameters are found from either experiment or simulation. It has been found to provide results with a great degree of accuracy when compared to experimental results, particularly in the case of Rayleigh waves [46]. This can be said to further validate the assumption used here that no crucial information is lost by representing the wave motion by a scalar wave equation. This implies that any error produced by using the transfer matrix here will not have an effect on the phenomena of device operation, and is therefore sufficient for the purposes required.

The source of the inaccuracy in $\widetilde{c_R}$ when using the scalar wave equation model is evident from the one-dimensional equations of motion (eq's. 3.32-3.37). In particular equation 3.35, the second continuity condition at the separation between a plated and un-plated region. This highlights the effect of the surface discontinuity introduced by the plating. This has been addressed separately in references [38], [57]. The effect of the discontinuity can be inserted as a point load [57], or be present in the boundary conditions as in equation 3.35 [38]. Again, in relation to the device under discussion,

the effect of this will be quantitative rather than phenomenological, in that the amount of energy transmitted and reflected will differ from this model, but will not affect device operation. It is of note that the one-dimensional transfer matrix for Rayleigh waves through a grating on a piezoelectric substrate has been derived in [38]. Similarly to the COM results, the results of this method can be easily inserted into the present model yielding a valid result. In fact, with adjustment of the coordinate system used, direct substitution of the components of the single cell transfer matrix within the aforementioned reference can be substituted directly into equation 3.106 for numerical evaluation. The derivation is, however, in depth and it does not add anything to be reproduced here. The most accessible course of action for specific device design is to obtain an accurate adjustment to $\widetilde{c_R}$ from literature, numerical simulation [60] or from experiment using methods such as those outlined in [59] and input these into the model presented here.

3.8.2 A note on the COM method

The COM method is used prolifically in the design of SAW filters and resonators and is arguably the most commonly used design tools for SAW devices. A comprehensive review on the topic was presented in reference [46]. An extension of the COM method is the P-matrix formalism, and the conclusions drawn herein are true for both methods. A reasonable question that could be posed by someone familiar with SAW design is: why not use the COM method to model the whole device? The answer is subtle but, to the authors mind, significant. COM based methods are powerful and useful tools, however they fail to capture and fully describe the phenomena of interest to the present device. Recalling that the variable of interest in the current work is the surface displacement field, and specifically the spatial distribution of amplitude. This is not commonly sought in SAW analysis and much more consideration is given to the frequency domain behaviour. This is reasonable considering the main application of SAW resonators as a bandpass filter. Accurate determination of the surface amplitude is far less significant than the selectivity in frequency space and much less the spatial distribution of the amplitude across coupled SAW resonators. The COM method was used in reference [58] for a very similar geometry to that of interest here. The analysis concerned application as a multipole filter. The frequency response was found for a symmetric structure of acoustically coupled cavities. The analysis however does not

yield access to the spatial distribution of the amplitude, furthermore, the analysis dismisses some of the fundamental physics of wave propagation that cause the effects of interest here, such as superposition of waves and separate cavity resonances. This determined the need for the development of a bespoke solution, as presented within this chapter. The solution presented here aimed to focus predominantly on the mechanics of wave motion. The ray tracing method employed, aimed to capture as much of the physics across as wide a range of the geometry as possible. Furthermore, as discussed in the previous section, this model can be used in conjunction with the COM method. It may then be reasonably thought of as an extension of the COM method to make it more amenable to the design and analysis of mode localization SAW devices.

3.9 Conclusions

Preliminary discussions have been presented covering results for the reduction of the three-dimensional elastodynamic equations of motion for Rayleigh waves to an equivalent one-dimensional model. In addition, the transfer matrix for locally periodic media was presented, non-dimensionalised and adapted for use in the current problem.

A general model for the device of interest has been derived aiming to provide insight into the wave dynamics of localization within the coupled resonant system. This employed a ray tracing method to define initial waves and reduction of their future propagation paths to closed form expressions. This yielded expressions for the displacement fields within each cavity of the device. The model incorporated generalities in the geometry, excitation method and wave type.

The validation of the model to SAW devices was discussed. Variations and substitutions of the result for the transmission coefficient were presented. Furthermore, the limitations of the COM model were outlined, highlighting the necessity for derivation of the model presented here. The model has been shown to exhibit excellent agreement with a separate numerically evaluated solution, providing a significant form of validation of the method and derived expressions. This deems the model as sufficient for use in the succeeding chapter as an analysis tool for use in evaluation of the envisioned devices described in the opening chapters.

Chapter 4. Numerical Modelling: Device Characteristics and Sensitivity Analysis

4.1. Introduction

The general model of the previous chapter provides access to a wealth of information about the system of interest. This chapter looks to explore the main characteristics of the device utilising the general model, before detailing and analysing the specifics of device operation. The chapter follows a similar structure to chapter 2; to aid with the transferral of concepts from the simplified discretized model, concepts from the second chapter are frequently recounted.

The chapter opens by discussing characteristics that are general to the device regardless of the chosen mode of operation. Specifically, the frequency response, and response to selective forcing are examined. The frequency response is discussed initially, examining the conditions for resonance as well as certain parametric sensitivities of the localized mode resonant frequencies. The analysis of the device response to selective forcing follows, defining the forcing parameters for coupling strongly into one mode whilst rejecting unwanted modal superposition.

The second half of the chapter looks specifically into device operation as a sensor, with the end goal of presenting the calibration curves of the device and assessing how the sensitivity of can be adjusted. These will be used in the following chapter in combination with a noise analysis to assess the potential signal-to-noise ratio (SNR) and dynamic range of the sensor protocol. On route to this end goal, the model derived in the previous chapter will be utilised firstly to provide a qualitative overview of the device operation. This will be followed by a quantitative analysis of both the natural frequencies and mode shapes. The movement of the natural frequencies in response to the cavity wave speed ratio, η, will be plotted and briefly discussed. The behaviour of the mode shapes in response to η governs the sensitivity of the device. Therefore this is discussed in the context of device sensitivity, yielding the calibration curves. The aims of the analysis as a whole is to inform device design covering geometry,

transduction and excitation and to provide a quantitative assessment of the potential device performance, measured by the achievable sensitivity.

4.2 Numerical model

A Matlab code was constructed to perform device modelling, design and analysis. An example of the code is shown in appendix C or available for permanent download at https://1drv.ms/u/s!Av2Ut-dHxCMA_VgyF2LN6_hoUqpb. The code first calculates the non-dimensional frequency dependent transmission and reflection coefficients given by equations 3.109-3.110. These are utilised to calculate the cavity amplitude frequency responses given by equations 3.146 and 3.149. The code then calculates and outputs the expected sensitivity and noise performance for a device described by the input parameters.

The tractability of the code is achieved by the reduction of the infinite sum shown in the previous chapter (equations 3.125-3.127). The time saved by this reduction is substantial, as is quantified in the following. Convergence of the truncated summation to the analytically found exact solution was found to vary dependent on the numerical values used, particularly for higher numbers of periods in the coupling array. This creates a rapidly varying solution in frequency space, requiring a higher frequency resolution to resolve adequately, thus increasing computation time. It was found that, for a reasonable selection of numerical values, acceptable convergence occurred with approximately 500 terms in each summation. Noting that equation 3.125 is the product of three summations, this amounts to $500^3 = 125{,}000{,}000$ terms. The reduced expression yields the exact solution whilst only requiring the evaluation of a single term. This was found to decrease the required computing time by a factor of 10^{-8}, the same as the increase in terms to be evaluated. This computational saving allows for fast and iterative design of a SAW mode localisation transducer without the requirement for a high powered computer.

4.3 Frequency Response

4.3.1 Overview

If the device is considered as truncated after the cavities, removing the enclosing arrays, it can then be considered as a continuous equivalent of the LPM presented in chapter 2. Considering the frequency response of such a device, it was shown that the majority of the modes reside in the pass band, with the localized modes within the stop band. In addition, there is the potential for local resonances to present themselves within the stop band in the presence of localized excitation. This can be seen to hold true in the analytical SAW model from the frequency response plot, overlaid on the coupling array transmission spectrum as shown in Figure 4.1. The outer reflection coefficients have been set to -1. This mimics the behaviour of a hard boundary condition allowing clearer visualisation of the position of the modes in frequency space.

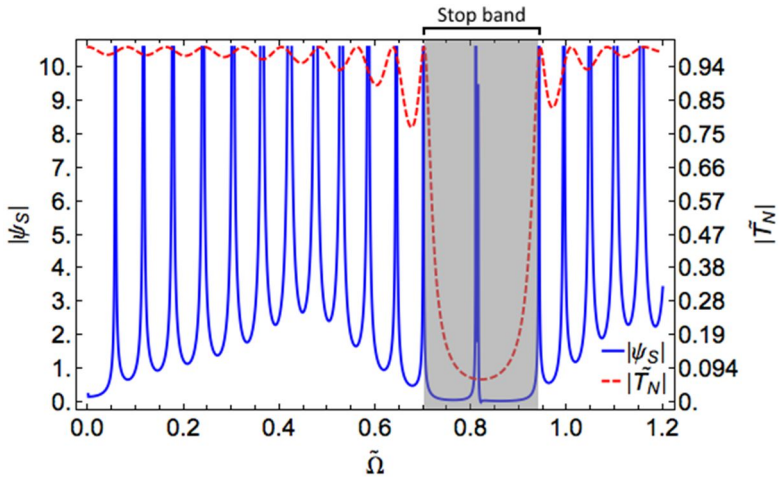

Figure 4.1 Sense cavity amplitude frequency response overlaid with the transmission amplitude coefficient. Assuming perfect reflection from enclosing cavities Parameters chosen as 10 periods in the coupling array, in-phase excitation, $\widetilde{c_R} = 0.7, \mu = 0.5, s = 1$

The non-dimensional coupling array parameters used for the transmission plot in Figure 4.1 will be used throughout this chapter. Therefore, for the rest of the discussion the stop band resides between the values $\widetilde{\Omega} = 0.7 - 0.95$.

4.3.2 Conditions for resonance

It was noted in the derivation of the chapter 3 that all the terms contributing to the displacement field share a common denominator, Λ (Section 3.5 Equation 3.132). When the denominator goes to zero, the displacement amplitude will grow towards infinity.

This is the condition for resonance that will be addressed in this section. Some initial characteristics of the denominator, Λ, will be discussed before the expression is inspected and a condition on $\widetilde{\Omega}$ yielded.

Figure 4.2 depicts two plots of Λ alongside one of the transmission spectrum. A general similarity can be seen when contrasting the plot shown in 4.2b to that of 4.1, the amplitude frequency response. This demonstrates the fact that the denominator governs the position of the resonant peaks. The numerator in equations 3.137 and 3.138 bears the initial waves. The numerator dictates the effect of the forcing on the response and can be used to strategically superpose wave amplitudes. This has the effect of cancellation or amplification resonances, as will be addressed in the next section. However, the total absolute value of displacement in the cavity, which could also be thought of as the total energy remaining within the cavity, is governed solely by the denominator. The next characteristic of note is the two different behaviour types occurring separately in the pass and stop band. It can be seen that the pass band peaks are evenly spaced and of a similar width. Two peaks occur within the stop band which can be seen in the scaled view of plot 4.2c. As previously indicated these will be the modes of interest to the device.

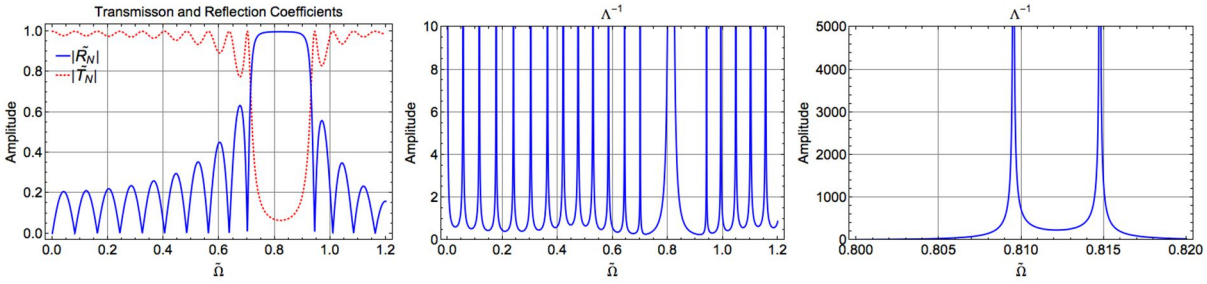

Figure 4.2 From left to right: (a) Transmission and reflection coefficients using standard parameters.(b) Inverse of the cavity amplitude denominator, Λ, across the pass and stop band. (c) As (b), zoomed to stop band.

The denominator expression, Λ (eq. 3.132), is expanded below in terms of the non-dimensional coefficients introduced in section 3.4.

$$\Lambda = 1 - \chi_A - \chi_B - \chi_C + \chi_A\chi_C \tag{4.1}$$

$$\Lambda = 1 - R_R R_C e^{i2\pi\tilde{\Omega}a} - R_S R_C e^{i2\pi\tilde{\Omega}\eta b} + R_R R_S\left(R_C{}^2 - T_C{}^2\right)e^{i2\pi\tilde{\Omega}(a+\eta b)} \tag{4.2}$$

The case of zero loss will be considered to determine the resonant condition, that is R_S and R_R are equal to -1. The substitutions listed in equations 4.3-7 are made to introduce the amplitude and phase components of the complex coefficients explicitly and simplify. The identity in equation 4.5 is presented in reference [61], and comes about from two factors. Firstly, due to the conservation of energy one can state equation 4.3, enforcing the total energy in the scattered waves to match the energy in the incident wave. Secondly due to the fact that the reflected and transmitted waves are always $\frac{\pi}{2}$ radians out of phase, as shown by Figure 4.3, one can write equation 4.4 from 4.3. This defines the amplitude and phase of the reflected wave relative to the transmitted wave, rather than the incident wave. Equation 4.5 follows from equation 4.4 and equation 4.6 defines the general expression for the amplitude and phase of the reflected wave (i.e. relative to the incident wave).

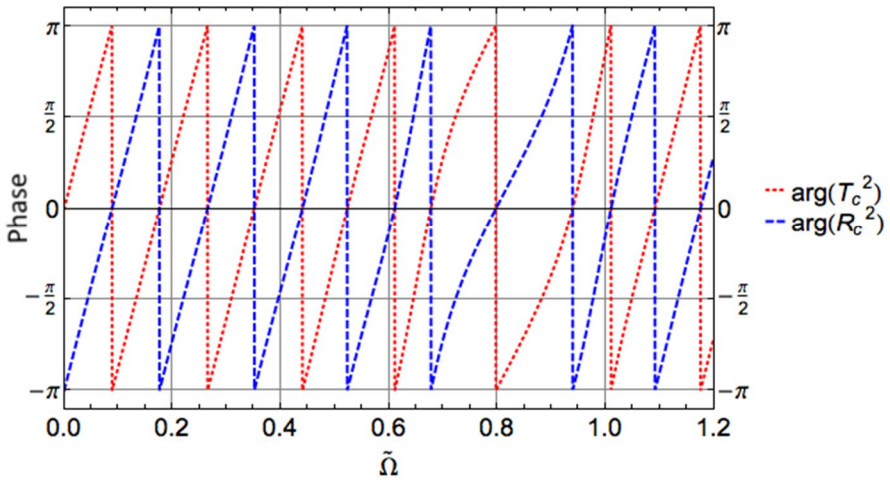

Figure 4.3 Phase spectrum of the square of the scattered waves.

$$|R_C|^2 + |T_C|^2 = 1 \tag{4.3}$$

$$R_C{}^2 = \left(1 - T_C{}^2\right)e^{i\pi} = T_C{}^2 - 1 \tag{4.4}$$

$$\left| R_C{}^2 - T_C{}^2 \right| = 1 \tag{4.5}$$

$$R_C = |R_C|e^{i\phi} \tag{4.6}$$

$$Arg[R_C{}^2 - T_C{}^2] = \vartheta \tag{4.7}$$

Insertion of the above substitutions, use of the identity [61] and adapting the expression to explicitly show the periodicity yields equation 4.8.

$$\Lambda = 1 + |R_C| e^{i(\phi \pm 2n\pi)} \left(e^{i2\pi\widetilde{\Omega}a} + e^{i2\pi\widetilde{\Omega}\eta b} \right) + e^{i(2\pi\widetilde{\Omega}(a+\eta b)+\vartheta \pm 2n\pi)} \tag{4.8}$$

As stated previously, resonance occurs when this expression is minimised, or in the 'no loss' case, equal to zero. It can be seen clearly now why there are two distinct behaviours, within the pass band and within the stop band. Within the pass band the transmissibility of the coupling array is close to unity (Figure 4.1) and therefore $|R_C| \approx 0$, with increasing validity as the number of periods in the coupling array goes to infinity. Observing equation 4.8, this condition will cause the central term to vanish. Conversely, within the stop band $|R_C|$ approaches unity (Figure 4.1) and all terms contribute to the resonant condition. Considering the pass band resonance initially, as described, setting $|R_C| = 0$ in equation 4.8, yields equation 4.9.

$$e^{i(2\pi\widetilde{\Omega}(a+\eta b)+\vartheta \pm 2n\pi)} = -1 \tag{4.9}$$

This constitutes the approximate condition for resonance within the pass band. This will be solved for $\widetilde{\Omega}$ to yield the natural frequencies. Taking the natural logarithm of both terms and simplifying and rearranging for $\widetilde{\Omega}$ yields equation 4.10.

$$\widetilde{\Omega}_n = \frac{\pi(2n+1) - \vartheta}{2\pi(a + \eta b)} \tag{4.10}$$

The parameter, ϑ, accounts for the phase shift due to the waves passing through the array. However, this is a function of $\widetilde{\Omega}$. It is linear and can be approximated by equation 4.11.

$$\vartheta = 2\pi\widetilde{\Omega}\left(N + r - Nr - 1 + (Nr/\overline{c_R})\right) \tag{4.11}$$

Substituting in yields the approximate equation for the natural frequencies within the pass band.

$$\widetilde{\Omega}_n = \frac{n}{\widetilde{L_{eq}}} \tag{4.12}$$

$$\widetilde{L_{eq}} = a + \eta b + N + r - Nr - 1 + (Nr/\overline{c_R}) \tag{4.13}$$

With a and b defined in terms of multiples of the coupling array period,s, $\widetilde{L_{eq}}$is the dimensionless equivalent cavity length. This accounts for wave travel across both cavities and the coupling array. Equation 4.12 states that a resonant frequency will occur when the non-dimensional natural frequency is any multiple of the inverse of $\widetilde{L_{eq}}$. Recalling that $\widetilde{\Omega} = 2s/\lambda$, this can be rewritten in terms of the wavelength and the dimensional equivalent cavity length as shown in equation 4.14.

$$L_{eq} = \frac{n\lambda}{2} \tag{4.14}$$

$$L_{eq} = s\big(a + \eta b + N + r - Nr - 1 + (Nr/\overline{c_R})\big) \tag{4.15}$$

Showing that, within the pass band, resonance occurs whenever the equivalent cavity length is equal to a multiple of half the wavelength. Figure 4.4 shows how the validity of this expression decreases as the frequencies approach the stop band, and the $|R_C| \approx 0$ becomes increasingly less valid. Displaying $\left|{R_C}^2\right|$ (black-dashed line), the true value of the denominator, Λ, (full-blue), the pass-band natural frequency expression of equation 4.9, without the phase approximation (green-dotted), and the approximate pass band natural frequency expression of equation 4.9 with 4.11 (red-dashed). The natural frequencies occur when the expressions are equal to zero. It can be seen that far away from the stop band the roots of the expressions are all well matched, but the root of the approximation drifts away as the frequency approaches the stop band.

Within the stop band the converse assumption can be made, that $|R_C| \approx 1$, reducing the condition for resonance to equation 4.16.

$$e^{\pm i2n\pi}\left(\left(e^{i2\pi\widetilde{\Omega}a} + e^{i2\pi\widetilde{\Omega}\eta b}\right)e^{i\phi} + e^{i(2\pi\widetilde{\Omega}(a+\eta b)+\vartheta)}\right) = -1 \tag{4.16}$$

Evaluation of this condition yields the stop band natural frequencies. The validity of the expression can be seen in Figure 4.5, contrasting it to Λ. Analytical evaluation of this expression is hindered as ϑ can no longer be approximated by equation 4.11, due to the nonlinear nature of the phase in the stop band. In addition, a closed form solution

for both ϕ and ϑ is not forthcoming from the transfer matrix solution. Therefore, this will be evaluated numerically to track the stop band modes in the analysis.

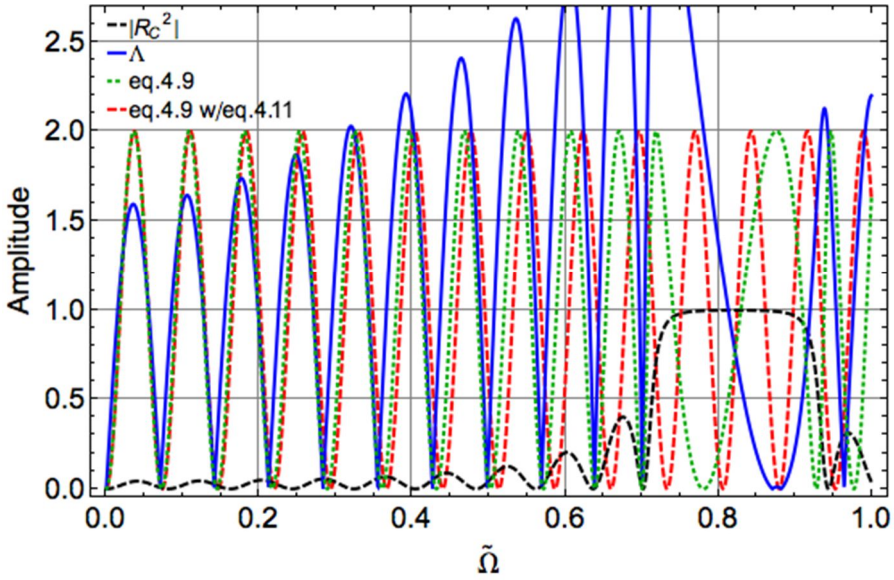

Figure 4.4 Comparison of resonant condition expressions. Highlighting reduction in validity of the expression in equation 5.9 as the frequency approaches the stop band.

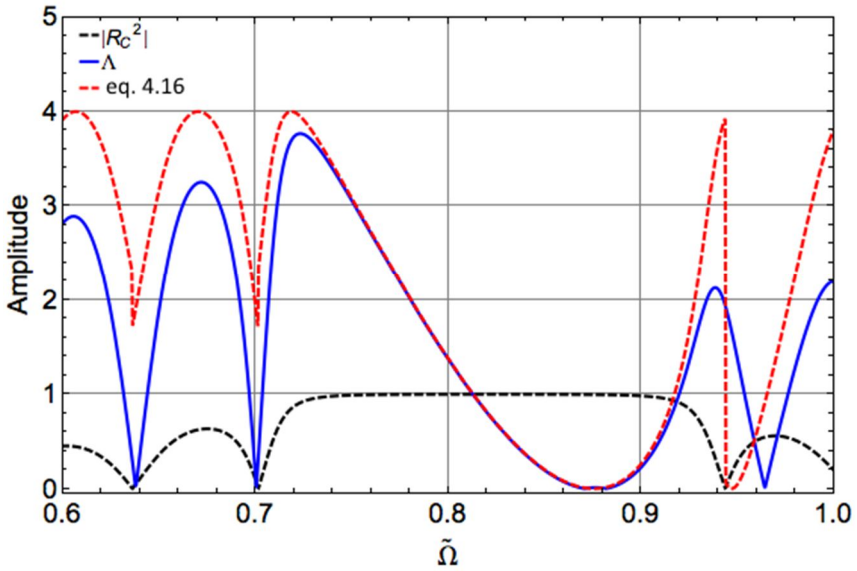

Figure 4.5 Comparison of condition for resonance functions in the stop band.

4.3.3 Effect of cavity length on stop band resonances

It is observed that the eigenvalues of the localized modes move within the stop band as the cavities are identically changed in length. Figure 4.6 plots the loci of the stop band natural frequencies as the cavity length is extended in integer multiples of the

wavelength. The modes are seen to drift upwards in frequency, asymptotically approaching the centre of the stop band. The separation between the modes is seen to reduce as cavity length is extended.

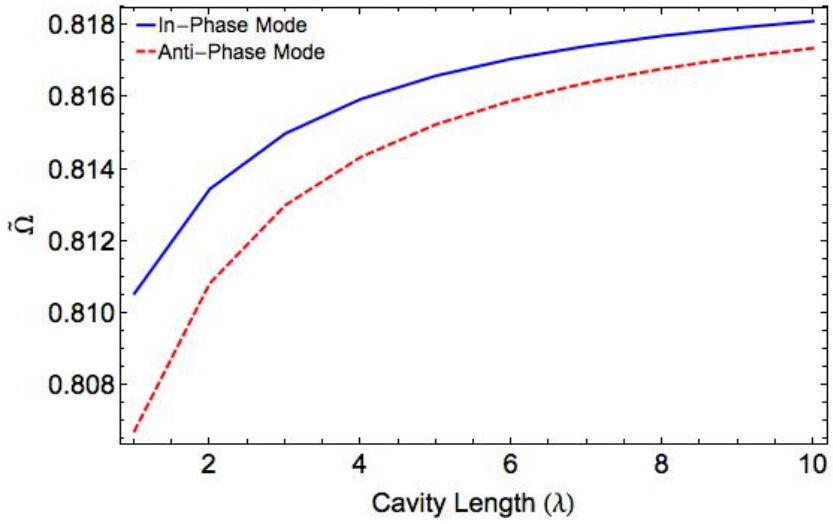

Figure 4.6 Localized mode frequency loci. Plotted for standard transmission properties with Nc=10.

4.3.4 Coupling array tuning

The effect of the coupling array parameters on the dispersion was introduced in section 2.5.1; it was shown that the upper and lower bounds of a stop band are a function of the array parameters. Furthermore, tuning the two expressions (eqs. 2.32-2.33) allowed for alteration of the stop band width and, when the expression were equal, the disappearance if the stop band. In the SAW case, the parameter available for stop band tuning is $\widetilde{c_R}$, the ratio of the wave-speeds within the plated and un-plated regions. The condition for nullification of the stop band is therefore $\widetilde{c_R} = 1$. It is unlikely that this limit will be practicable, but the effect of varying $\widetilde{c_R}$ around unity is discussed briefly here. The plots in Figure 4.7 show how the transmission spectrum varies as $\widetilde{c_R}$ is varied around unity.

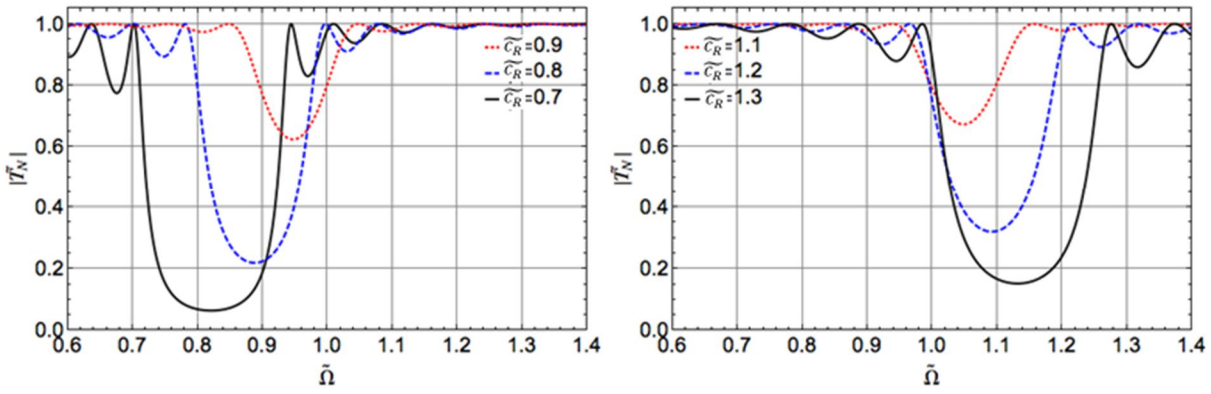

Figure 4.7 Variation of the transmission spectrum for a change in the wave speed within the plated region.

The stop band depth and breadth is reduced as $\widetilde{c_R}$ moves away from a value of 1. In addition, the stop band drifts in opposite directions for positive and negative values of $\Delta\widetilde{c_R}$. The effect of this on the localized modes is depicted in Figure 4.8.

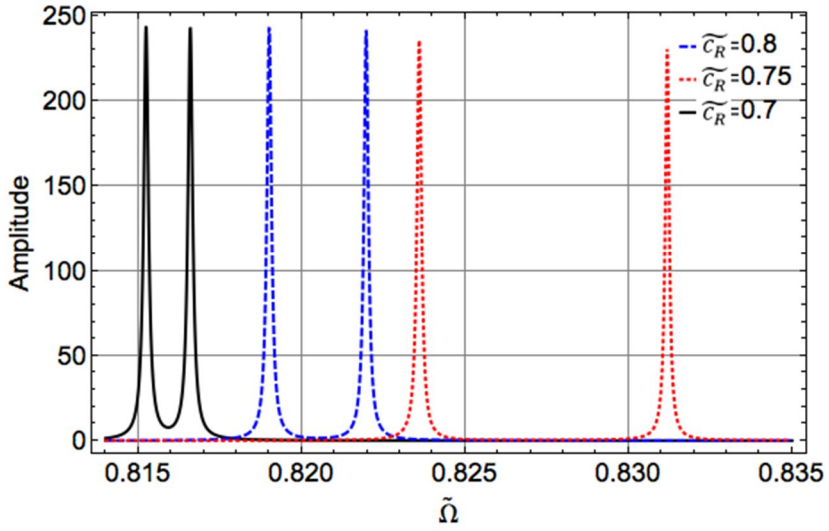

Figure 4.8 Effect of change in transmission spectrum on the localized modes.

The modes move in frequency space in the same direction as the stop band, however, at a slower rate. The modes drift towards the lower limit of the stop band, and are submerged within the pass band by the time $\widetilde{c_R}$=0.9. The separation between the modes is also increased as the coupling strength is increased.

4.4 Selective forcing

As discussed in chapter 2, the device will be operated in one mode. It was suggested that the excitation be chosen so as to couple strongly into one mode and weakly into

the other in order to facilitate this. This will be discussed here in relation to the SAW device. Considering the case where the central point of each cavity is a node, this is equivalent to the initial wave field being made up of a leftwards and rightwards propagating waves. Figure 4.9 depicts the three forcing scenarios to be considered: in-phase, anti-phase and asymmetric.

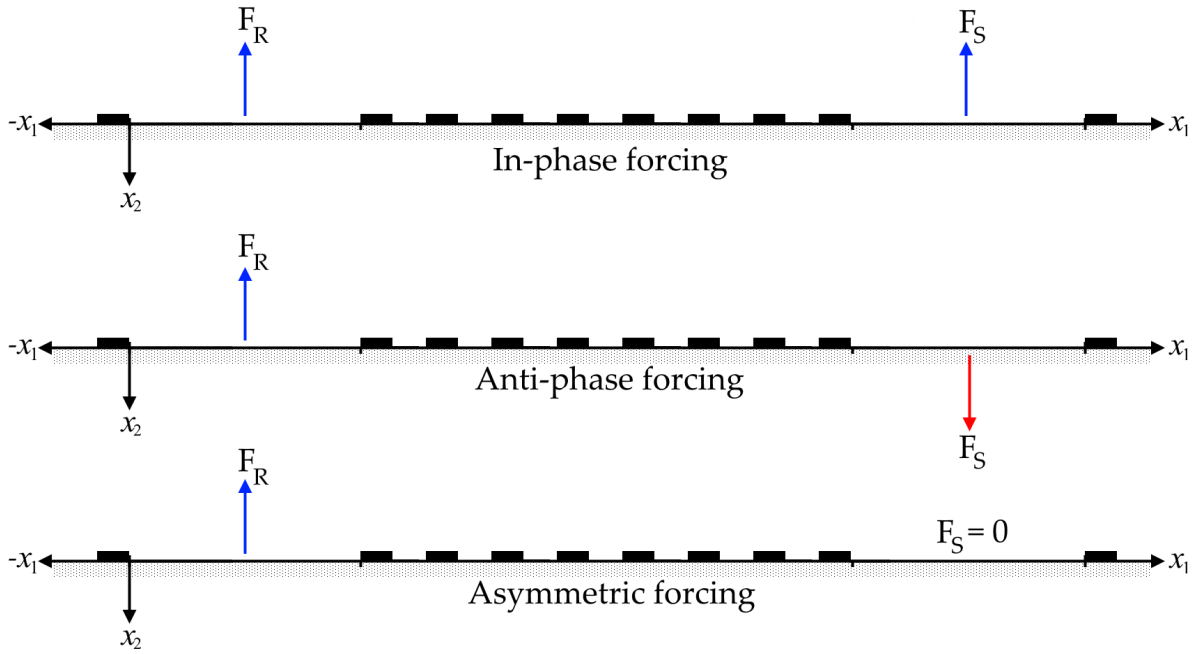

Figure 4.9 Graphical representation of the three forcing scenarios to be considered in the analysis. The forcing arrangements are shown on the device schematic presented and annotated initially in Figure 3.10.

For in-phase selective forcing of unit amplitude, the forcing coefficients of equations 3.133-136 take the values given below.

$$F_{RL} = \frac{P}{\mu_L} \qquad (4.17) \qquad F_{RR} = -\frac{P}{\mu_L} \qquad (4.18)$$

$$F_{SL} = \frac{P}{\mu_L} \qquad (4.19) \qquad F_{SR} = -\frac{P}{\mu_L} \qquad (4.20)$$

For the case of anti-phase selective forcing the reference cavity coefficients remain as in equations 4.17 and 4.18, and the sense cavity coefficients take the values given in equations 4.21-22.

$$F_{SL} = -\frac{P}{\mu_L} \qquad (4.21) \qquad\qquad F_{SR} = \frac{P}{\mu_L} \qquad (4.22)$$

The case of asymmetric loading will also be considered, in which both modes are coupled into equally. In this case the coefficients F_{SL} and F_{SR} are equal to zero and for this section of the analysis the ratio $\frac{P}{\mu_L}$ was set to unity. The effects of these forcing conditions are demonstrated in the plots of Figure 4.10. Where the reference and sense cavity amplitude and phase frequency responses are plotted for a reasonably well damped system ($Q{\sim}10^2$). The dissipation in the model is controlled by the length of the enclosing arrays, in this case they have been set to 5 periods.

The first conclusion to draw is the similarity of these plots with the selective forcing frequency response provided for the LPM, demonstrating consistent behaviour between the two models. It is clear that the frequency dependent behaviour changes dependent on the forcing condition. Addressing the asymmetric loading first, the amplitude response within both cavities resemble a damped bimodal system. The phase plots indicate that the cavities are resonating out-of-phase over the first resonance. As the frequency increases the phase within the sense cavity swings into phase with the reference cavity for the second resonant peak. It is of note that the phase shift normally associated with a resonant peak are suppressed by the heavy damping. When the damping is reduced the phase shifts for all resonance peaks are visible and pronounced.

The order of the modes is consistent for the selectively forced responses as is evident from the relative phases in each cavity. The observation that the phases are consistent over the frequency range of interest indicates that the selective forcing has allowed one mode to dominate across the entire range.

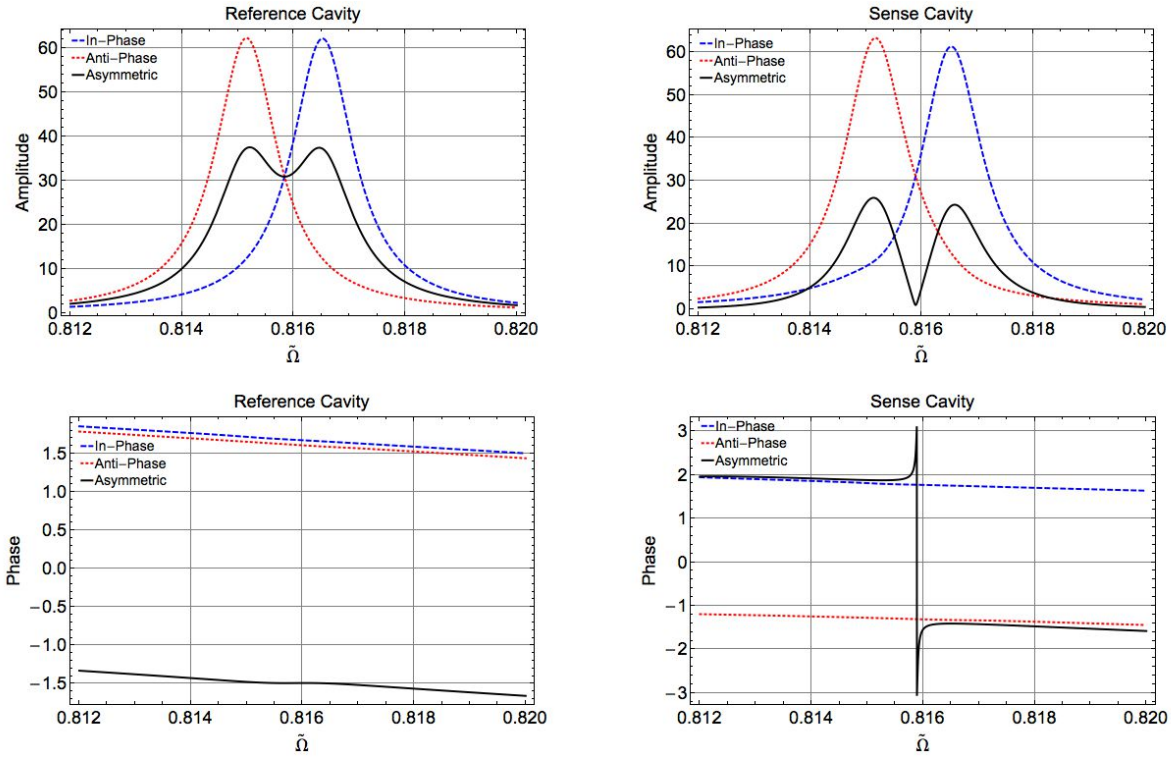

Figure 4.10 Amplitude and phase response to selective forcing.

It is implied in the analysis of chapter two, the geometry has an effect on the order of the modes. If the cavities are an integer number of wavelengths long, then the anti-phase mode occurs at a lower frequency than the in phase mode. As seen above for the case of 5 wavelength long cavities. Conversely, if the cavity lengths are a non-integer multiple of half a wavelength, then the order of the modes is switched in frequency space. This implies that when the cavities are a integer number of wavelengths long the ratio of strain energy to inertial energy in the anti-phase mode is lower than when the cavity lengths are a non-integer multiple of half a wavelength. The converse being true for the in-phase mode. Evidence of this is given in Figure 4.11, when the cavity lengths have been shortened by half a wavelength. In this case the centre of the cavity is an anti-node, and the initial waves originate a quarter of a wavelength off-centre.

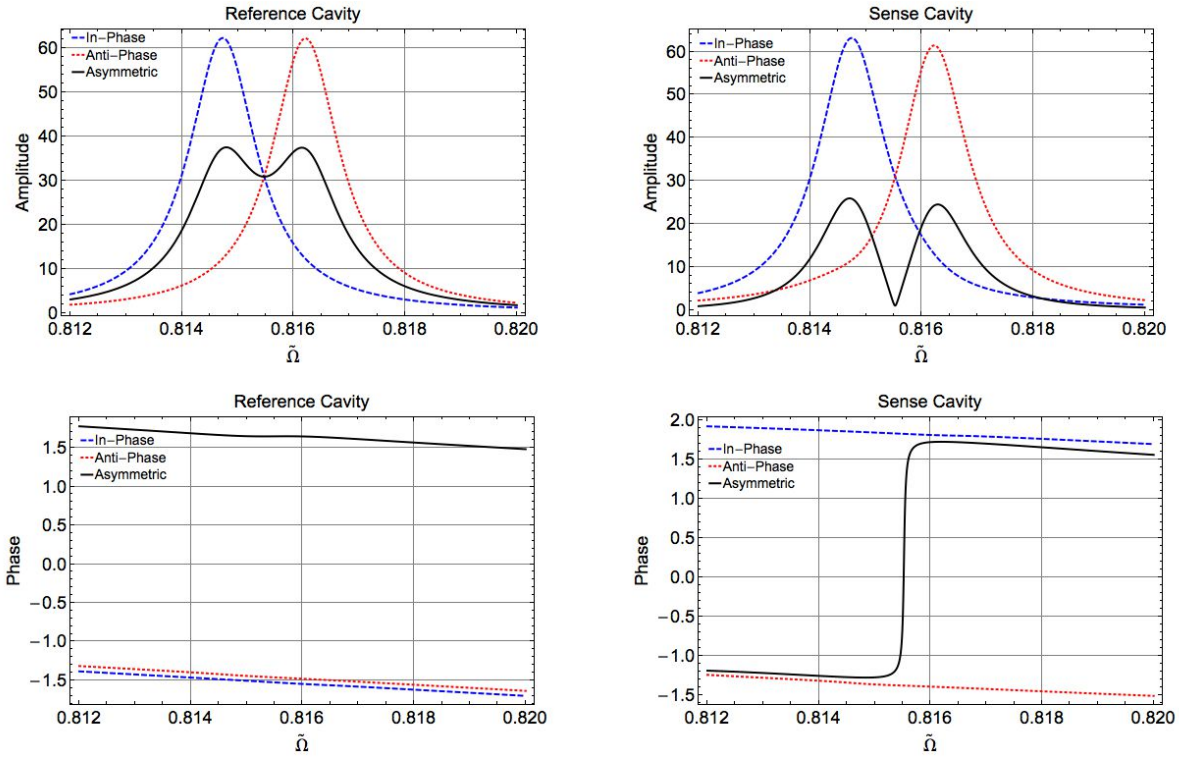

Figure 4.11 Response to selective forcing with cavity length equal to a non-integer number of wavelengths (4.5λ).

4.5 Device operation

4.5.1 Qualitative overview

For the symmetry breaking mode of operation, it is intended that the device be selectively forced, and the mode shape of interest tracked. Localization within the mode is induced by altering the parameter η, the wave-speed ratio, shown in equation 4.23 where γ_0 and c_0 represent the substrate wavenumber and wave speed respectively.

$$\eta = \frac{\gamma_{SENSE}}{\gamma_0} = \frac{c_0}{c_{SENSE}} \tag{4.23}$$

The desired behaviour can be seen qualitatively utilising similar frequency plots to above. In Figure 4.12, the loss from the system has been reduced by increasing the periods in the enclosing arrays to 9 per array. This has no effect on the amplitude ratio, but aids with visualisation. The device is forced asymmetrically to display the behaviour of both modes.

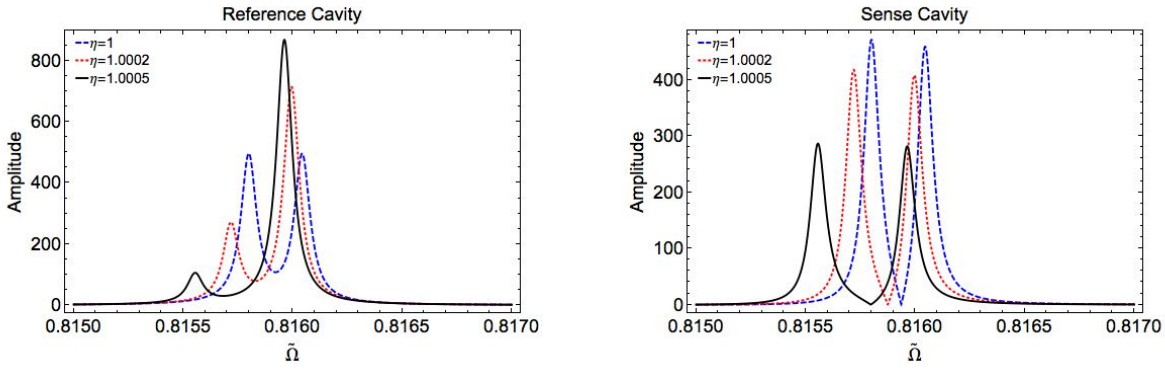

Figure 4.12 Plots illustrating the effect of η on cavity amplitudes.

The plots in Figure 4.12 overlay the behaviour in the separate cavities as η is incrementally increased. The effect of this on both the resonant frequencies and mode shapes is evident. Frequency drift is observed in that both peaks are drifting downwards in frequency space, with the lower mode moving at a faster rate than the higher. Localization is seen in the mode shapes by comparing the relative amplitude of the peaks in each cavity as η is varied. This can be seen more clearly by observing the same event from a different perspective as displayed in Figure 4.13. By overlaying both cavity amplitudes on the same plot for fixed η, the asymmetry in the cavity amplitudes is clearly visible. It can be seen that when $\eta = 1$ the cavity amplitudes are well matched in both modes. As η is increased the amplitudes of both modes decrease identically in the sense cavity. However, in the reference cavity the high mode's amplitude grows, indicating localization of energy in the reference cavity. Within the lower frequency mode, the amplitude shrinks, however, there is still an asymmetry with the sense cavity, with the mode favouring the reference cavity. Furthermore, the plots in in Figure 4.14 show that when η is reduced, a similar natural frequency drift is observed as well as the amplitude asymmetry in both modes. The same effects detailed for the previous case are observed, however the modal behaviours are switched.

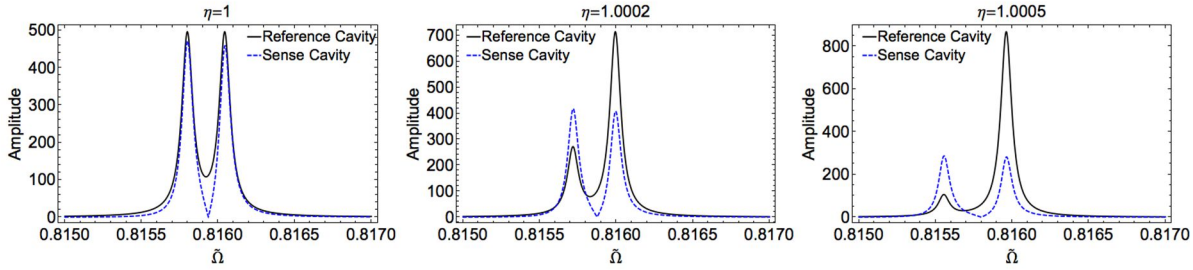

Figure 4.13 Plots detailing effect of increasing η on amplitude ratio.

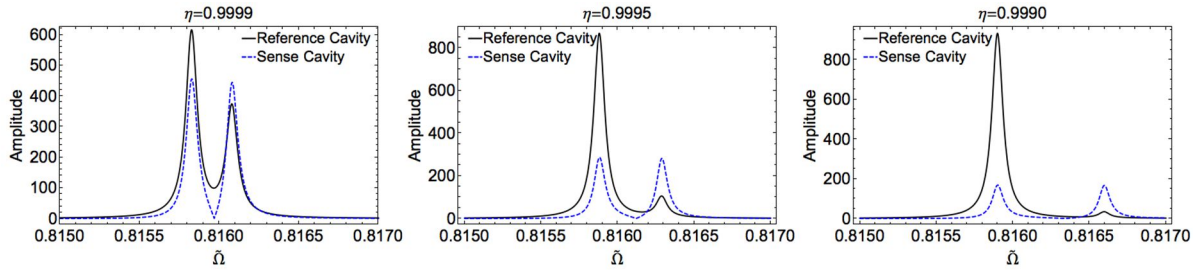

Figure 4.14 Plots detailing effect of decreasing η on amplitude ratio.

4.5.2 Behaviour of Natural Frequencies

It was observed qualitatively that the natural frequencies drift away from one another as the asymmetry is increased. By plotting this behaviour in both directions around $\eta = 1$ (Figures 4.13-14), it can be seen that the behaviour observed is the phenomenon of eigenvalue loci veering. This has been well documented in the fields of MEMS [62], [63], periodic structures [26], [64], as well as mode localization sensors [25]. Because of this, and as this is not the primary behaviour of interest in the current investigation, it will only be discussed here in brief.

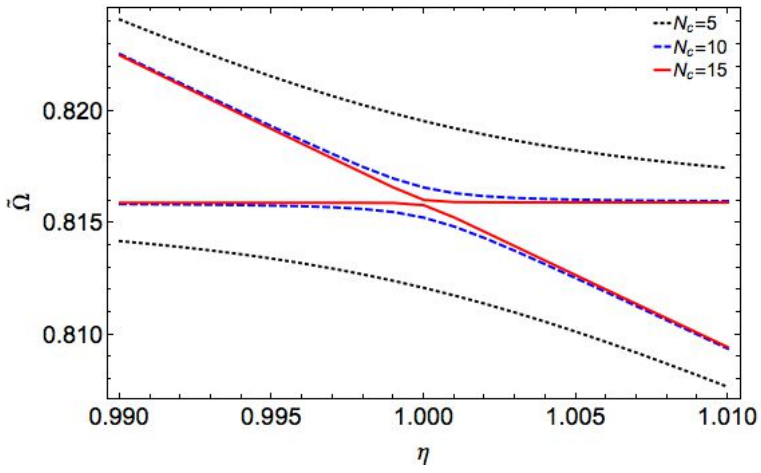

Figure 4.15 Eigenvalue loci veering.

The plot in Figure 4.15 is a typical example of loci veering as can be seen by comparing it to plots in references [26], [64]. In reference [26] it is stated that loci veering and mode localization are two manifestations of the same phenomenon, and one predicts the other. Of note is the asymmetry of the veering, as is more prominent in the higher coupling period plots, when η is increased, the higher frequency mode remains fairly stationary as the lower frequency mode veers to a greater extent. The converse being true for decreasing η. In addition, it is seen that when the coupling periods are increased, the symmetric modes ($\eta = 1$) are drawn closer together.

4.5.3. Sensitivity

The sensitivity, S, is defined at the change in the amplitude ratio per unit change in η, as given in equation 4.24.

$$S = \frac{d}{d\eta}(|\psi_S|/|\psi_R|) \tag{4.24}$$

The modes can be tracked in frequency space by setting $\widetilde{\Omega}$ equal to the condition for resonance (*c.f.* section 4.2.2). Substituting this into the cavity amplitude expressions allows for calculation of the change in cavity amplitudes with varying parameters. To begin, forcing was prescribed solely in the reference cavity in order to couple into both modes. The enclosing arrays were chosen to be 9 periods long to provide some dissipation ($Q \approx 8000$). Both the number of periods in the coupling array and η were varied, with the results reported for the cavity amplitudes and amplitude ratios for each mode case, in Figure 4.16.

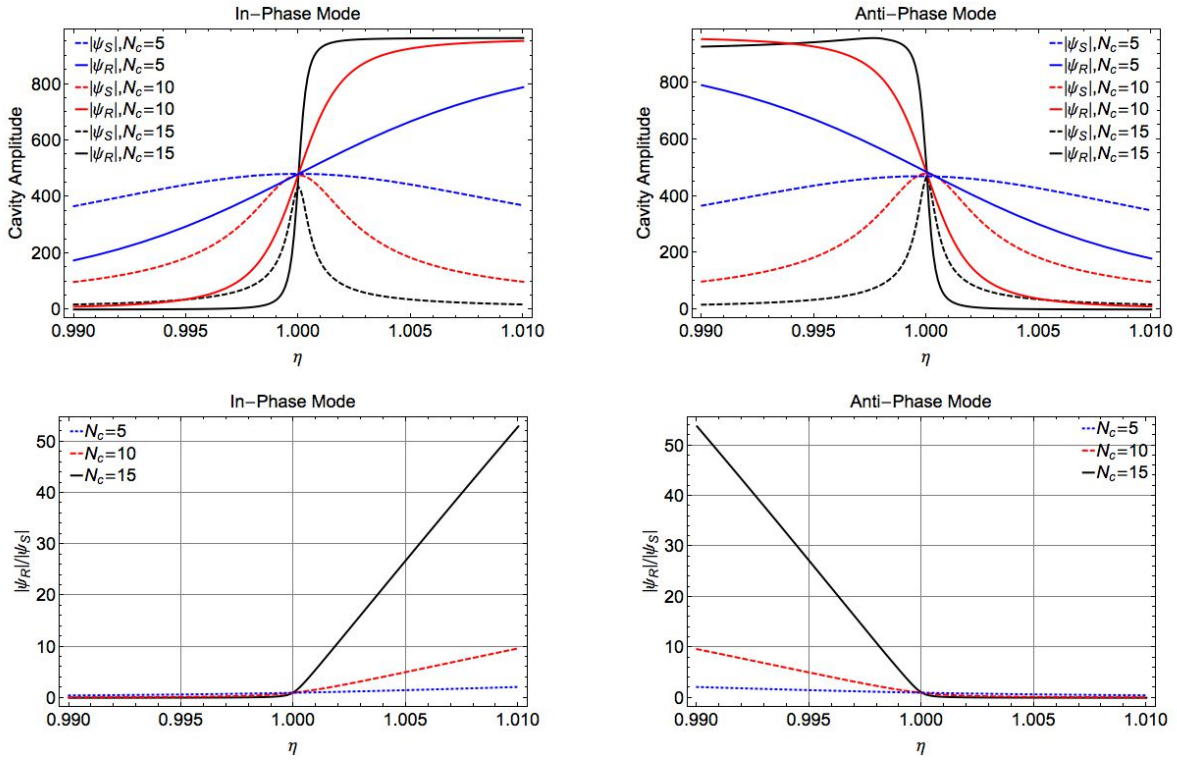

Figure 4.16 Cavity amplitudes and amplitude ratio against η for asymmetrically forced device.

It is evident that there is a remarkable symmetry between the behaviour in the modes, the cavity amplitudes and amplitude ratio plots are almost a mirror image of each other. There is a shift in behaviour across the line $\eta = 1$, and the point of intersection of all cavity amplitudes lies upon this line. This denotes an amplitude ratio of unity occurring in all cases when $\eta = 1$. The sense cavity amplitudes are symmetric about $\eta = 1$, however, the reference cavity undergoes a sharp change in amplitude, inverting the amplitude ratio. It is of note at this point that the intensity of the behaviour is modulated by the number of periods in the coupling array. It can be seen that as N_C is increased the cavity amplitude distributions in η-space become more localised. The effect is more explicit in the amplitude ratio plots, from which the sensitivity can be found, in that the gradient (S) is increasing with increasing N_C. This shows implicitly the relationship between the coupling strength and the sensitivity. It has been shown that the coupling strength is reduced exponentially by increasing the lengths of the coupling array, and now that this will in turn increase the sensitivity. The amplitude ratio response appears linear for amplitude ratios greater than unity. The sub-unity behaviour is displayed in greater detail in Figure 4.17.

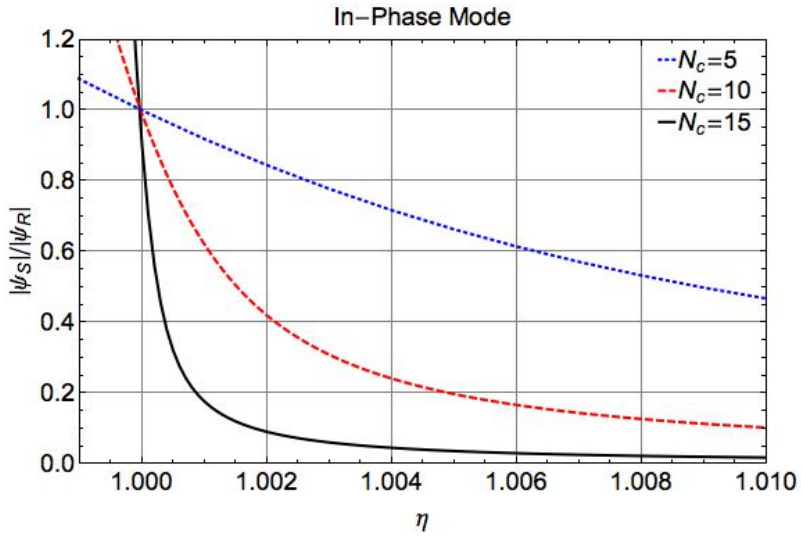

Figure 4.17 Sub-unity amplitude ratio behaviour.

The amplitude ratio asymptotically approaches zero, as would be expected from the evident symmetry of the cavity amplitude plots, providing non-linear behaviour. Considering the case of selective forcing, the plots in Figure 4.18 depict the amplitude responses of the forced and un-forced mode similarly to the asymmetric forcing case. The responses are identical for the in-phase and anti-phase modes, so are shown here as general plots to encompass both cases. Other than a change in the forcing condition, the parameters are as used for Figure 4.18.

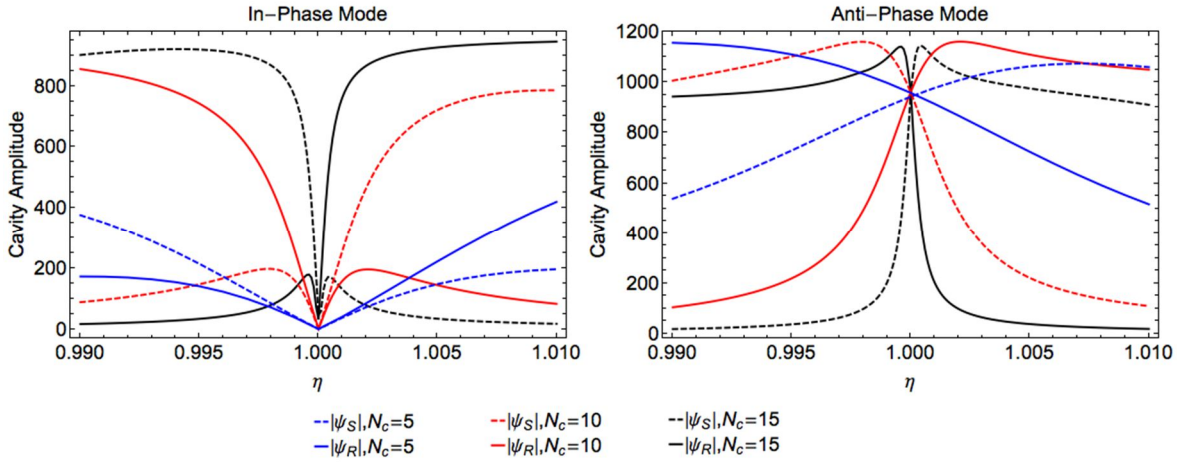

Figure 4.18 Cavity amplitudes against η for the symmetrically forced case.

The symmetry of behaviour in the cavities is immediately evident, showing the same amplitude ratio switch across $\eta = 1$. In the case of the forced mode, the point of intersection of all lines still occurs on $\eta = 1$, indicating unity amplitude ratio as desired.

In the un-forced case however, all cavity amplitudes reduce to zero, as expected from section 4.3. The amplitude ratio plots to compliment the above forced and un-forced cavity responses are provided in Figure 4.19. Somewhat surprisingly, the sensitivity in either mode is not effected by the forcing condition, even if that mode has zero amplitude at $\eta = 1$.

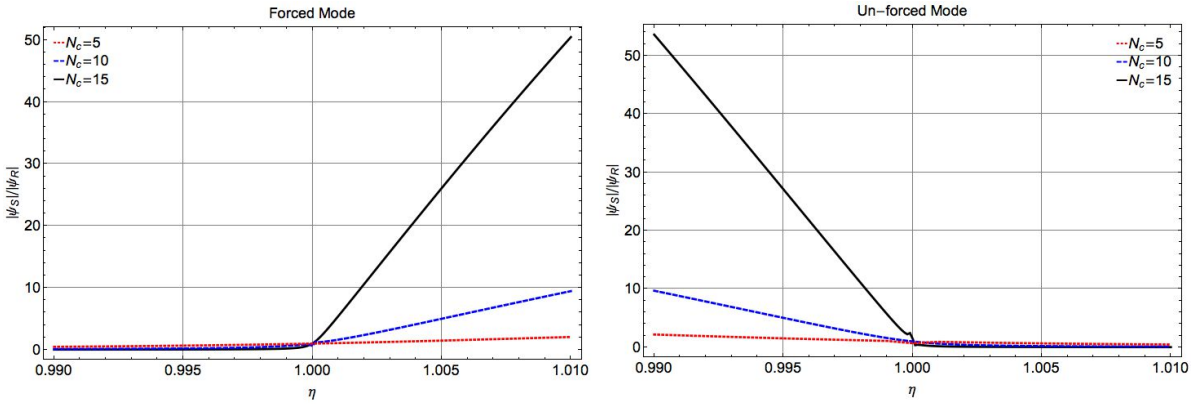

Figure 4.19 Amplitude ratio against η for symmetrically forced case.

It has been shown in Figures 4.16-19 that, in line with previous qualitative analyses, the sensitivity is increased by growing the coupling array, hence lowering the coupling strength. The effect can be found to be exponential as is depicted in linear and log-linear plots of Figure 4.20.

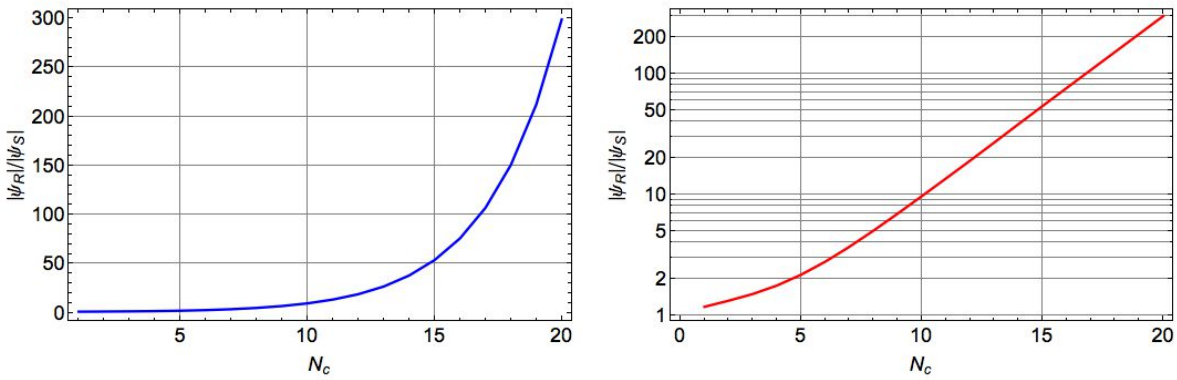

Figure 4.20 Effect of number of periods in coupling array on device response (η=0.99).

The exponential behaviour fits well with the fundamentals of transmission through periodic arrays, back to the definition of the propagation constant. The propagation constant was defined as a complex exponent that was multiplied by the number of periods in the array. The real part provided spatial decay, therefore the transmitted

force is described by $e^{N_C\mu}$, where μ is a real constant. This concept held true in a similar form for continuous systems, and has manifested in an exponential relationship between sensitivity and periods in the coupling array. It is noted that the log-linear plot is not completely linear as N_C approaches zero, more specifically, this is seen below $N_C \approx 5$. This is expected as the array is moving into a region where it can no longer be validly described as periodic, and the above argument no longer holds.

The first plot in Figure 4.21 constitutes an example of a calibration curve of the sensor, for a stimulus that would reduce the wave-speed within the sense cavity. A potential example of this would be adsorption of biological analytes in operation as a mass sensor. The gradient of this curve is the device sensitivity as is also plotted in Figure 4.21. The response will likely reach a limiting maxima (saturation) when the growing cavity amplitude is limited by non-linearity. The limit of detection is likely to be due to intrinsic thermal noise processes and will be evaluated in chapter 5.

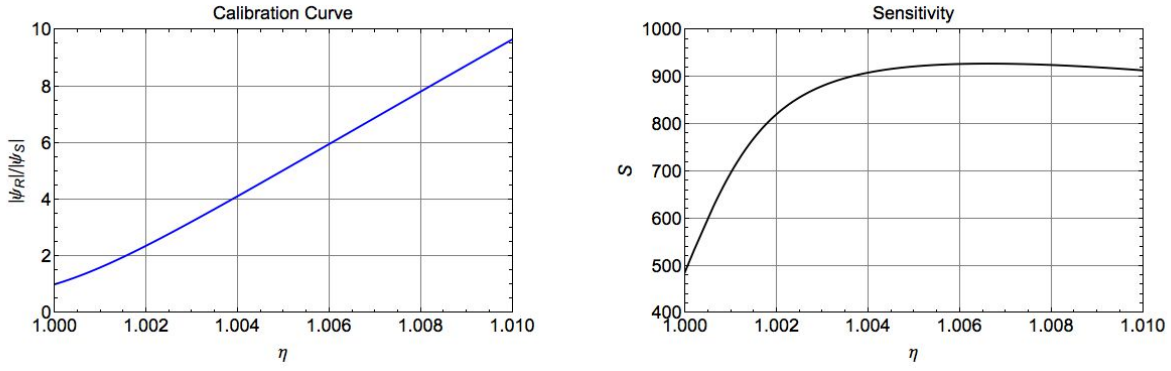

Figure 4.21 Calibration curve and sensitivity of the device ($N_C = 10$).

It can be deduced that the response is not linear due to the variable sensitivity. The main nonlinearity in the sensitivity is due to the change in behaviour across the $\eta = 1$ line. This is accentuated in Figure 4.22, also detailing the sensitivity increase due to increased periods in the coupling array.

Away from the $\eta = 1$ line the sensitivity plateaus, and although still not constant, it is agreeable to a linear approximation. Figure 4.23 exemplifies a linear approximation of the form given in equation 4.25.

$$\frac{|\psi_S|}{|\psi_R|} = -(C_1 - C_2) + C_1\eta \tag{4.25}$$

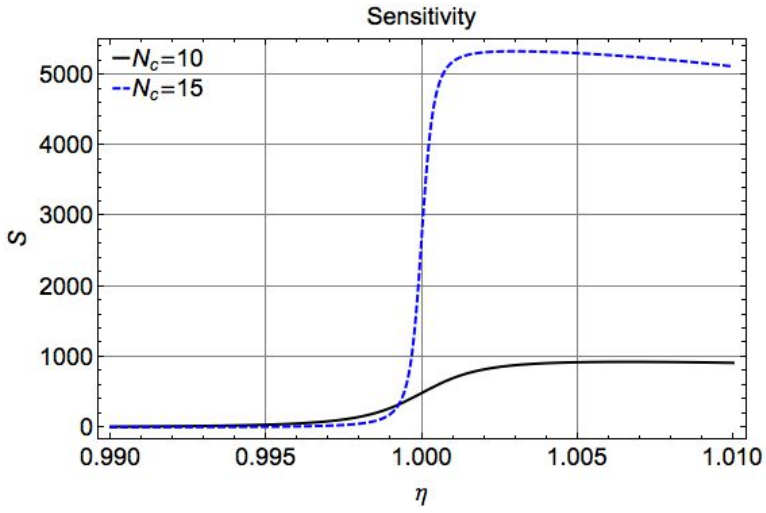

Figure 4.22 Sensitivity against η

For the case of ten coupling periods the parameters were chosen as $C_1 = 930$ and $C_2 = 0.4$, this clearly gives a 60% error at $\eta = 1$, however away from this point it can be seen the error is much smaller. This suggests for implementation of the device it may be useful to have some initial asymmetry, enough to move the response into the quasi-linear region.

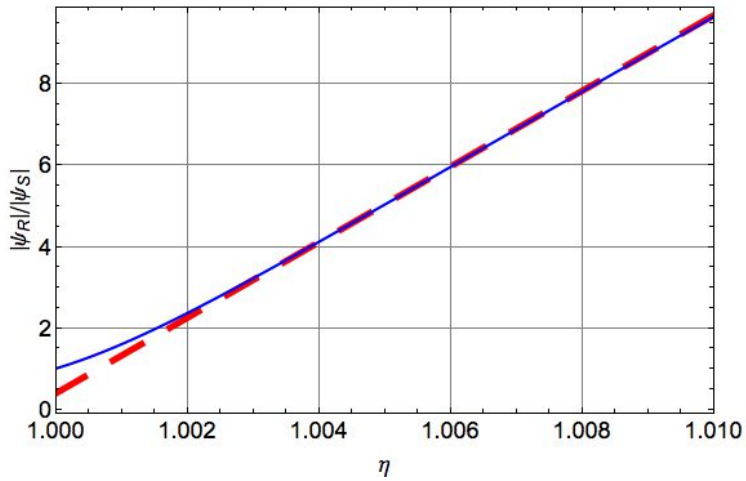

Figure 4.23 Linear approximation of device response.

4.6 Conclusions

The general model derived in chapter 3 has been applied to the specific structure of interest in the context of exploitation as a mode localization sensor. The frequency response was explored in some depth. Conditions for resonance have been outlined and an expression found for the pass band natural frequencies. The effects of alteration of cavity length and changes to the array dispersion on the frequency response were detailed. Selective forcing was investigated and parameters found, for the symmetric case, to couple strongly into one mode whilst rejecting the other.

Device operation was discussed in depth. The mode of operation was described qualitatively with the aid of selected results provided by the general model. It was found that the device exhibits the phenomenon of eigenvalue loci veering. The response of the mode shapes and the sensitivity of the device was addressed in detail. It was found that although the amplitude ratio response appears linear with respect to η, there is in fact some non-linearity present. However, a linear approximation was found to fit well, with the highest error close to the symmetric case, where a change in behaviour occurs. It was suggested that this could be accounted for by having some initial asymmetry designed into the device.

Valuable extensions and continuations of the work presented within this chapter can be found through further analytical scrutiny of the model of chapter 3. One particular example is the lack of a closed form solution for the natural frequencies within the stop band (c.f. section 4.2.2). Due to the complex frequency dependence of the phase components, derivation of this was found to be intractable. However, with further time and sufficient simplifying assumptions, this result can potentially be yielded. This would also allow derivation of further expressions, in particular one for device sensitivity. This would give valuable insight into device design and tuning, as well as indicating the source of the non-linearity present in the sensitivity. In the same vein, quantification of the size of the aforementioned initial asymmetry would be of value, if it was found to be a necessary parameter of device design.

An additional extension is presented from the discussion of section 4.2.4. regarding coupling array tuning. It was shown that adjustment of $\widetilde{c_R}$ can smoothly transition a

mode into the pass band, where it will become a fully distributed mode, with an amplitude ratio of approximately unity. This opens up the possibility of an alternate sense regime, where the output is triggered by an alteration of $\widetilde{c_R}$, with a 'designed-in' asymmetry. Initial investigation of this method proved to be inferior in sensitivity to mode localization sensing. Predominantly as it relies on a large frequency shift, which is known to occur more slowly than the change in the amplitude ratio through symmetry breaking [2], [25]. However, this approach may provide practical benefits of some form and may warrant further investigation.

Chapter 5. Loss Quantification and Thermal Noise

5.1 Introduction

This chapter serves to quantify the main loss mechanisms that contribute towards the Q-degradation and intrinsic noise within the device. The total intrinsic noise will be quantified and used in conjunction with the results of the previous chapter to provide the limit of detection (LOD) and signal-to-noise ratio (SNR). The quantification of the loss and noise acts as a first step in assessing the feasibility of the device functioning once manufactured. The analysis will also look for ways to minimise each noise contribution to yield the highest SNR.

5.2 Loss Mechanisms and Q quantification

The main contributors to the intrinsic loss of SAW resonators are listed in [65] as: viscous material propagation loss (Q_{mat}), gas or fluid damping (Q_{fluid}), surface propagation loss (due to an imperfect surface finish) (Q_{surf}), bulk wave scattering (Q_{bulk}), radiation from ends of the enclosing arrays (Q_{rad}) and diffractions from the sides of the cavities and reflectors (Q_{diff}). The total Q is the inverse of the sum of the inverse of these quantities as shown in equation 5.1.

$$\frac{1}{Q_{total}} = \frac{1}{Q_{mat}} + \frac{1}{Q_{fluid}} + \frac{1}{Q_{surf}} + \frac{1}{Q_{bulk}} + \frac{1}{Q_{rad}} + \frac{1}{Q_{diff}} \tag{5.1}$$

In the following, each loss form will be discussed separately in brief before being considered in combination using equation 5.1 to determine the overall Q-factor of the device. It is implied in the experimental results in reference [66] that the surface loss can be reduced to an insignificant level. It will be assumed that the surfaces are sufficiently smooth so that surface loss can be neglected. In addition, electrical losses such as resistive dissipation in the IDT fingers will not be considered.

5.2.1 Radiation Loss

Within this section the different forms of radiative energy loss are discussed in turn, considering first the energy loss from the ends of the enclosing arrays Q_{rad}. This can

be easily quantified by recasting the problem of chapter 3 to solve for the displacement fields outside of the enclosing arrays. The ratio of the energy retained to the energy lost per cycle would provide a measure to quantify Q_{rad}. It is quoted in reference [67] that it can be quantified by equation 5.2.

$$Q_{rad} = \frac{n\,\pi}{1 - R^2} \tag{5.2}$$

Where R is the amplitude reflection coefficient of the enclosing arrays. However, the energy lost through these arrays is easily tuned towards zero simply by increasing their length. This loss mechanism therefore becomes vanishingly small, so that it can be considered to not contribute to the overall Q of the device. Furthermore, it has been shown experimentally in reference [66] that a sufficiently long array can be found to reflect as much as 98% of the incident wave back in the form of a surface wave. Considering some wave energy will be lost through other means, this can be considered experimental verification that this form of loss is inconsequential to the system.

The obvious trade-off for maintaining a high Q_{rad} by extension of the enclosing arrays is the limitations imposed on minimum device size. The interplay of this, the factors determining cavity length (such as SNR) and the minimum lithographic resolution will impose the hard limit on device length.

5.2.2 Diffraction Loss

Diffraction loss can be considered another radiative loss form with waves leaving the device in the transverse direction. This loss form has been quantified in reference [68] for a device where the arrays are created from grooves in the substrate. By considering the diffraction of the beam as it traverses the cavity, the diffraction loss is proportional to the square of the beam width and can be described by equation 5.3 [68].

$$Q_{diff} = \frac{5\,\pi}{|1 + \zeta_a|}\left(\frac{b_w}{\lambda}\right)^2 \tag{5.3}$$

Where b_w is the beam width and ζ_a is the material anisotropy coefficient. It is shown in reference [68] that for $LiNbO_3$, considering an anisotropy coefficient of $\zeta_a = -0.75$, equation 5.3 reduces to equation 5.4.

$$Q_{diff}^{LiNbO3} = 20\,\pi\left(\frac{b_w}{\lambda}\right)^2 \tag{5.4}$$

When the device is constructed in this way, the equations 5.3 and 5.4 show that this loss form can be removed as the limiting factor by increasing the beam width. It is stated in reference [68] that, in ST cut quartz or Y-Z lithium niobate, a width of 50λ is sufficient to remove this as the limiting factor in the total- Q.

When the enclosing arrays are constructed from metal strips deposited on top of the substrate, it is stated in reference [68] that one must also consider diffraction loss from out of the edges of the array. It is suggested, however, that matching the incident beam width to the reflector width allows it to act like a wave guide, reducing the loss. Additionally, curved reflectors may be used to focus reflections such that they remain within the cavity.

5.2.3 Bulk wave scattering

Bulk wave generation from discontinuities on the surface is in fact another form of loss through radiation. This is vanishingly small when $h/\lambda \ll 1$ [67], [68], where h is the strip height. In the context of a resonator enclosed by grooved arrays, this has been quantified in both theory and experiment to be kept vanishingly small when the strip height satisfies $h/\lambda < 0.02$ [68]. In addition, the experimental result of reference [66], recalled previously in the context of radiation loss provides further evidence that this is also the case for arrays constructed of metal strips. Due to these considerations, the contribution of bulk wave generation will be neglected from the total- Q, so long as the strip height to wavelength ratio is adhered to.

5.2.4 Fluid damping

Energy is lost to the surrounding environment due to work being done by the out of plane component of displacement field on the environmental fluid, be that a liquid or a gas. The energy is both converted to heat through viscous friction and radiated away as acoustic waves. This has the potential to be a dominant form of loss from the system and a limit on the maximum achievable Q. The quantification of this loss form will not be considered; instead, two ways of mitigation will be considered, at least one of should be applicable to any device.

Firstly, a commonly used method for many MEMS devices is operation under vacuum. The degree to which this reduces the loss depends on the degree to which the surrounding area has been evacuated. However, assuming a suitable level of vacuum has been achieved, this has been stated in references [67] to eliminate this a form of loss.

For certain applications, operation under vacuum will not be feasible. The obvious example of this is mass sensing, where the device must be immersed in the carrier fluid in order to sense the presence or absence of the particle under consideration. For applications such as this, it is proposed that the device be operated using a wave type with purely in-plane displacement field. Surface skimming bulk waves and Love waves present two examples which could be utilised to this end.

5.2.2 Material loss

It is stated in references [65], [67], [68] that the viscous dissipation occurring within the substrate material corresponds to the ultimate limit on the maximum achievable Q.This form of loss is generally quantified through experiment and fitted to models representing its effect. Commonly, a complex modulus [69] or wavenumber [68] is employed to represent the attenuation of wave motion. One such model for quantifying Q_{mat} is provided in reference [68] and shown in equation 5.5.

$$Q_{mat} = \frac{\pi}{\alpha_d \lambda} \tag{5.5}$$

Where α_d is a frequency dependent dissipation parameter found from experiment. This has been found for Y-Z lithium niobate in reference [68] as $29.1 \times (10^{-9} f)^2 \left(\frac{nepers}{m}\right)$. Inserting this parameter into equation 5.5 allows for the calculation of the frequency dependent Q_{mat}.

With the considerations outlined in this section, for a chosen material, the value of Q_{mat} can be used for the assumed Q_{total} of the device and the other contributors imposed as design rules and limitations on device size.

5.3 Mechanical-thermal noise

Thermal noise was originally discussed in relation to electrical circuits. Now well established and commonly used, it is known eponymously due to the original treatise as Johnson-Nyquist noise. The basis of the argument for noise generation is that each source of dissipation creates a path for thermal excitation of the system - the so-called fluctuation-dissipation theorem. In the case of resistors in an electrical circuit the excitation relates to thermal agitation of electrons. Energy lost through the resistor is converted to heat; this in turn causes voltage fluctuations in the resistor due to the equipartition theorem, turning each resistor in the circuit into a voltage generator, introducing noise into the system. The equipartition theorem states that each variable in the system has a thermal energy equal to $k_B T/2$ where k_B is the Boltzmann constant and T is the temperature. Thus for a mechanical system in thermal equilibrium, both the kinetic and potential energies must separately equate to the equivalent thermal energy expression. In the context of a mechanical system, the noise can be due to Brownian motion of particles external to the elastic solid or internal frictions within the deforming elastic solid, causing fluctuations in force rather than voltage. A typical example is particle bombardment on the mass of a simple spring-mass-damper accelerometer. The particles in the atmosphere surrounding the mass are undergoing motion proportional to the atmospheric temperature, this will lead to particle bombardment on the mass of the system, causing excitation and introducing noise into the system. An expression for the spectral density of the mechanical-thermal noise has been presented in references [70], [71] as equation 5.6.

$$F_{mech-therm} = \sqrt{4k_B T c_d}\ N\sqrt{Hz}^{-1} \tag{5.6}$$

Where c_d is the damping coefficient (equation 5.7) inserting this into equation 5.6 yields equation 5.8.

$$c_d = \frac{m_{eq}\omega_n}{Q} \tag{5.7}$$

$$F_{mech-therm} = \sqrt{\frac{4k_B T m_{eq}\omega_n}{Q}}\ N\sqrt{Hz}^{-1} \tag{5.8}$$

This is the square root of the spectral density of the input force due to thermal excitation. To utilise this in the context of a SAW system, first an equivalent mass of the system must be derived, then the displacement due to this force will be found in order to determine the SNR and resolution. The equivalent mass will be found from the maximum inertial energy in one cavity, given by equation 5.9.

$$\mathrm{E_I} = \frac{1}{2}\rho \int_V \dot{\underline{u}}^2 \mathrm{dV} \tag{5.9}$$

Taking the square as the scalar product of $\underline{u}$ with itself, and recalling that $\underline{u}$ is a 2D elastic field thus constant in the x_3-direction. Equation 5.9 becomes Equation 5.10 where the time derivative has been performed assuming harmonic motion.

$$\mathrm{E_I} = \frac{1}{2}\omega^2 \rho L_w \int_A ({u_1}^2 + {u_2}^2)\mathrm{dA} \tag{5.10}$$

Where L_w is the width of the device in the x_3-direction. The free wave solution of equations 3.22 and 3.23 is substituted in. Integrating over one wavelength in the x_1-direction and from 0 to infinity in the x_2-direction yields the energy in one wavelength. The maximum inertial energy per cycle in one wavelength is written in equation 5.11.

$$\mathrm{E_{I-MAX}} = 0.09875\frac{\lambda^2}{2}\omega^2 \rho L_w A^2 \tag{5.11}$$

Equating this expression to the maximum kinetic energy of a spring-mass resonator $m_{eq}v^2/2$ yields an equation that can be solved for the equivalent mass of one wavelength.

$$m_{eq-\lambda} = 0.09875\lambda^2 \rho L_w \tag{5.12}$$

The number of wavelengths in a cavity is equal to L_C/λ, substitution into 5.12 gives the equivalent mass of one cavity.

$$m_{eq} = 0.09875\lambda\rho L_w L_C \approx 0.1\lambda\rho l_w L_C \tag{5.13}$$

The mechanical-thermal noise force can now be written directly in terms of the device parameters.

$$F_{mech-therm} = \sqrt{\frac{4k_B T\omega_n \lambda \rho L_w L_C}{10Q}} N\sqrt{Hz}^{-1} \tag{5.14}$$

The excitation force is kept constant during device operation and the amplitude changes independently due to the external stimulus. Therefore, to calculate the SNR and LOD, it is necessary to calculate the displacement amplitude due to the thermal noise excitation and evaluate it alongside the sensor response amplitude. This mean square displacement due to this force can be found using the frequency response function derived in chapter 3. Taking the square of equations 3.148 and 5.13 and integrating over the response bandwidth yields equations 5.15-16.

$$\langle|\psi_{noise}|^2\rangle = \frac{1}{2\pi}\int_{-\Delta\omega/2}^{\Delta\omega/2} |G_{\mathrm{RR}}(\omega)|^2 P_{\mathrm{mech-therm}}\, d\omega \tag{5.15}$$

$$P_{\mathrm{mech-therm}} = \left(\frac{F_{mech-therm}}{L_w}\right)^2 (N/m)^2 Hz^{-1} \tag{5.16}$$

This can be written explicitly as equation 5.17, where due to the loss considerations stated in the first section of this chapter, the cavity width is asserted as 50λ.

$$\langle|\psi_{noise}|^2\rangle = \frac{4k_B T\omega_n \rho L_C}{1000\pi\mu^2 Q}\int_{-\Delta\omega/2}^{\Delta\omega/2} \frac{(1-\chi_C)^2}{(1-\chi_A-\chi_B-\chi_C+\chi_A\chi_C)^2}\, d\omega \tag{5.17}$$

The term within the integrand redistributes the noise power within the device bandwidth, producing a gain at the operating frequency. This gain can be evaluated numerically, or more conveniently for a rough calculation it can be approximated as $Q\Delta\omega$. Multiplying by the bandwidth provides the total noise power around the resonant frequency, further multiplication by the Q-factor gives the resonant displacement amplitude due to this input force. Using this approximation the root mean square displacement amplitude in one cavity is given below, where the relationship $\omega_n = Q\Delta\omega$ has been utlised.

$$\sqrt{\langle|\psi_{noise}|^2\rangle} = \sqrt{\frac{4k_B T{\omega_n}^2 \rho L_C}{1000\pi\mu^2 Q}} \tag{5.18}$$

Although it may seem to appear as though against intuition noise grows with increasing mass, the $\omega_n{}^2$ term is classically classically is equal to k/m, and physically represents the ratio of strain energy to inertial energy. In this particular scenario the stiffness, or strain energy is proportional to μ, the shear modulus. The inertial energy is proportional to ρL_C. The implications of this is that the noise amplitude is independent of device size and depends inversely on μ, the resistance to motion. However, this dependence neglects the effect of cavity size on Q which can be included by solving the integral in equation 5.17.

The response amplitude is defined by equation 5.19.

$$\Delta|\psi_S| = C_1 \Delta\eta |\psi_R| \tag{5.19}$$

Where C_1 is the linear approximation parameter introduced in equation 4.23. The SNR can be found as the ratio of the square of equation 5.19 to the square of equation 5.18.

$$SNR = \frac{1000\pi\mu^2 Q {C_1}^2 \Delta\eta^2 |\psi_R|^2}{4k_B T {\omega_n}^2 \rho L_C} \tag{5.20}$$

Defining the minimum detectable limit as the response yielding an SNR of unity, the limit of detection (LOD) can be described by equation 5.21.

$$\Delta\eta_{min} = \sqrt{\frac{4k_B T {\omega_n}^2 \rho L_C}{1000\pi\mu^2 Q {C_1}^2 |\psi_R|^2}} \tag{5.21}$$

5.4 Conclusions

The different forms of mechanical loss contributing to the overall Q of the device have been listed and, where appropriate, quantified. Methods of reducing loss have been discussed. It can be concluded that all forms of radiation loss can be made vanishingly small by making limitations on device size. The limit on achievable Q is determined by the propagation loss due to the material.

The mechanical-thermal noise has been discussed and the noise due to the total loss quantified in terms of the spectral density of the root mean square amplitude fluctuation within the cavities. This has been used in conjunction with the results of

the previous chapter to yield expressions for the SNR and LOD. This contextualises the limits imposed on the device function by the loss mechanisms present.

Chapter 6. Case Study: Application as a MEMS Magnetometer

6.1 Introduction

Previous chapters have described and analysed the SAW mode localization sensor in an abstract and general way. Little reference was given to any particular sensing application, but rather only to a perturbation of the wave-speed in the sense cavity by some external influence. This chapter aims to provide some context for the design by presenting a case study of one particular application of the SAW mode localization sensor: a MEMS magnetic field sensor. In addition to contextualising the work presented in the preceding chapters, the case study will assess the potential impact of the novel sensor implementation on the current landscape of MEMS sensors.

The chapter opens by providing a background and history of magnetic field sensors and their development. A specific example of a SAW MEMS magnetic field sensor, the delay line sensor, is subsequently presented. This utilises a similar architecture and operating principle to the SAW mode localization magnetometer, and therefore the literature can provide useful information for the analysis presented here. A description and evaluation of the SAW mode localization magnetometer is then presented before conclusions are drawn.

6.2 Background

6.2.1 Magnetic field sensors

Magnetic field sensors or 'Magnetometers' have wide ranging applications, prominently in the automotive, aerospace, medical, military and research fields [72], [73]. The sensors are of fundamental importance for the efficiency of operation of many devices, from cars to computers [72]. The types of use vary in sensitivity requirements; brain function mapping is an example of an application requiring a high-sensitivity sensor, whereas an application such as current sensing, requires a much lower sensitivity [72].

Magnetometers are commonly compared based on parameters such as minimum size, power consumption, resolution and noise. The development and improvement of magnetic field sensors has been gradual, with small steps in improvements of these

features with each advancement in technology [74]. Resonant MEMS magnetometers (RMMs) are mostly still in a developmental stage. These however show potential for low cost, small-size sensors with favourable noise and resolution capabilities [74].

The majority of proposed RMMs utilise the Lorentz force to deflect a sense structure. The deflection is amplified by exciting the structure at resonance, this has the added advantage of rejecting off-resonance noise [69]. A review of such devices is presented in reference [73]. A much smaller subset of these devices are those using the delta-E effect exhibited by giant magnetostrictive materials, as will be presented here.

Magnetostriction is the induction of a strain in a material in the presence of a magnetic field [75]. This effect is common to all ferromagnetic materials, although in most the effect is very small. Materials have been engineered in which the magnetostrictive effect is large, these are termed giant magnetostrictive materials [75] prominent examples include Terfenol-D and Galfenol. The delta-E effect [75] is a property of these materials, in addition to a strain, there is a large relative change in the Young's modulus of the materials. Some authors exploited this latter effect in the design of RMMs [76], [77].

Thin film platings of magnetostrictive materials have been shown to perturb the wave speed of surface acoustic waves in proportion to an external magnetic field [78]–[81]. Utilising this effect SAW magnetostrictive magnetometers have been presented in references [80], [81]. These use a delay line configuration to sense the change in local magnetic field strength. One such device presented in reference [81] consisted of an area of Galfenol thin film deposited between two IDTs and the change in the phase was correlated to magnetic field strength. The experimental results found in the aforementioned reference provide the exact parameters necessary to assess the SAW mode localization sensor as a magnetometer. Within this chapter this will be input into the models and expressions gained in the previous chapters to evaluate the potential for a SAW mode localization sensor.

To date, no attempt has been made in the literature to design or manufacture a magnetic field sensor using the phenomenon of localization. Such a device has the potential to achieve the much-desired properties of low-cost, high-resolution, low-noise and small package size. In addition, the device would benefit from the intrinsic

common-mode rejection associated with mode localization sensors. This work will seek to determine whether these advantages can be realised. Ripka and Janosek concluded in their review [74] that progress in miniaturisation will not occur without the use of new physical principles. It is believed by the author that localization is one physical principle worthy of investigation to benefit the field.

6.2.2 The SAW delay line magnetometer

This magnetostrictive effect has been utilised in the literature in a delay line configuration to create a SAW magnetometer [80], [81]. Examples of this are presented here in more detail in order to provide pertinent results that will be utilised in the following section for the evaluation of the mode localization magnetometer.

The basic layout of a SAW delay line sensor in presented in Figure 6.1. It can be seen that this is a standard two-port SAW device. A wave excited in the input IDT traverses the free space region producing an output at the sense IDT with a constant phase lag from the input. In the presence of a magnetic field, the magnetostrictive thin film perturbs the wave speed in the free space region, altering the phase lag in proportion.

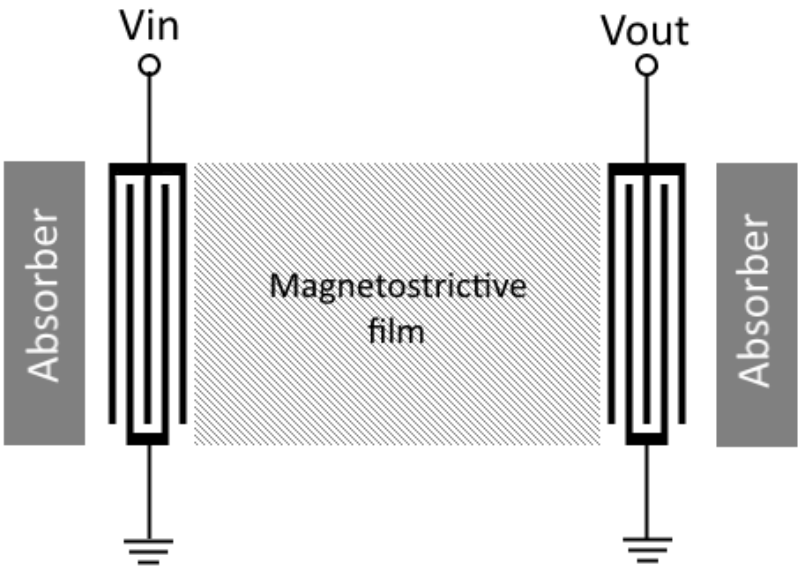

Figure 6.1 Schematic of a SAW delay line magnetometer.

This concept has been presented in references [55], [78], [82], although not explicitly applied to sensing the applied magnetic field. These references used thin films of nickel (Ni) [82], Terfenol ($TbFe_2$) [78] and cobalt-chrome (Co-Cr) [55] on lithium niobate

($LiNb0_3$) substrates. The wave speed perturbations achieved in these references are summarised in Table 6.1.

Other examples have been presented in references [80], [81], in which the design was target specifically at sensing the local magnetic field strength. Li *et al.* [81] used Galfenol (FeGa) on ST-cut quartz and it is the results of this study that will be used to assess the mode localization magnetometer. The experimentally yielded results from [81] are summarised in Table 6.1 alongside the results of the aforementioned references.

Table 6.1 Summary of literature values of SAW wave speed perturbation by a magnetic field

Substrate	**Substrate Rayleigh wave speed**	**Plating**	**Maximum wave speed perturbation**	**Max η**	**Reference**
ST cut quartz	3158 m/s	500nm Galfenol	0.64% over 0.1 Tesla	0.0064	[81]
Y-Z LiNbO3	3488 m/s	2.5um Terfenol-D (TbFe2)	-0.27% over 4KOe	-0.0027	[78]
Y-Z LiNbO3	3488 m/s	0.85um Nickel	0.07%	0.0007	[82]
Y-Z LiNbO3	3488 m/s	4um Cr-Co	0.03%	0.0003	[79]

6.3 Evaluation of the SAW mode localization magnetometer

Within this section a conservative estimate for the SNR achievable by reconfiguring the SAW delay line magnetometer of Li *et al.* [81] as a mode localization magnetometer. The substrate and plating construction will kept identical to that summarised in the top row of Table 6.1, however the geometry is altered to resemble the device presented within this these. A schematic is shown in Figure 6.2.

The SNR was first expressed in equation 5.20. In order to quantify SNR in the context of a magnetometer, the change in η due to the magnetostrictive effect must be related to the magnetic field strength. To enhance SNR, the sensitivity can be tuned by device design, altering the linear response coefficient C_1 (*c.f.* equation 4.23).

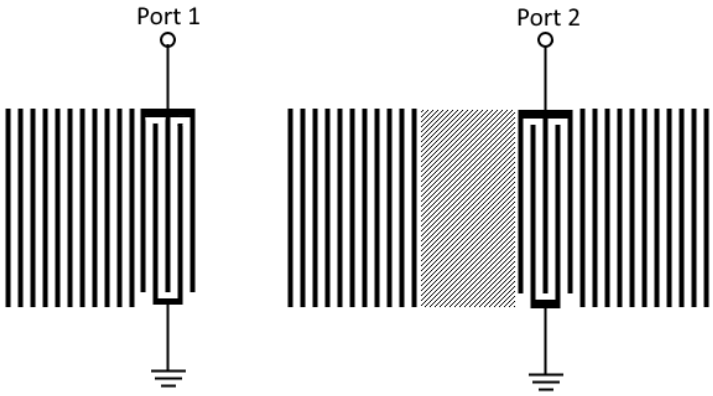

Figure 6.2 Schematic of a SAW mode localization magnetometer.

The change in η can be found from the result presented reference [81] and listed in the first row Table 1. This assumes a 500nm thick Galfenol film has been deposited across the sense cavity. Allowing a $\Delta\eta_{max}$ of 0.0064 over a range of 0-0.1T, assuming linearity of this change yields equation 6.1. By substituting this into equation 5.20, it can be approximately recast in terms of the field strength B in Tesla, this is shown in equation 6.2.

$$\eta = 0.064B \tag{6.1}$$

$$SNR \approx \frac{\pi\mu^2 Q {C_1}^2 B^2 |\psi_R|^2}{100 k_B T {\omega_n}^2 \rho L_C} \tag{6.2}$$

Defining the field sensitivity as the minimum detectable change in magnetic field strength in the presence of noise, the device sensitivity can be quantified as equation 6.3.

$$\Delta B_{min} \approx \sqrt{\frac{100 k_B T {\omega_n}^2 \rho L_C}{\pi\mu^2 Q {C_1}^2 |\psi_R|^2}} \tag{6.3}$$

Using equation 6.3, the SAW mode localization sensor will be compared to the current state-of-the-art in terms of field sensitivity in the presence of noise. Device size will also be addressed. For a base line comparison the material parameters and operating frequency from reference [81] will be used. This gives a starting point with parameters that are known to be manufacturable. Therefore, using an ST-quartz substrate, the reflectors will be made from sputtered 180nm thick aluminium. The device will operate

with a Rayleigh wavelength of 20um, which corresponds to an operating frequency around 158 MHz. Aluminium fingers on ST-quartz have been found to have a reflectivity equal to $0.507h/\lambda$ per finger [57] in the centre of the stop band. Therefore, using the prescribed thickness and wavelength, full reflectivity would be achieved with approximately 220 fingers array.

In chapter 5 it was stated that the radiative Q contributions can be made insignificant with restrictions on device size, and hence the total Q can be taken as equal to Q_{mat}. The propagation loss of ST-quartz was discussed in reference [65], reporting $Q_{mat} \approx 10^5$ at frequencies around 10^8Hz. This will be assumed as Q_{tot} for the device being considered here. A device width of 50λ is assumed, it was discussed in chapter 5 that this width should be sufficient to eliminate diffraction loss. The assumed parameters for the device are now summarised in Table 6.2.

Table 6.2 Parameters used for initial characterisation of the performance of a SAW mode localization magnetometer

Parameter	Symbol	Value
Angular frequency	ω_n	$2\pi \cdot 158 \times 10^6$ rad s^{-1}
Quality factor	Q	10^5
Boltzmann constant	k_B	1.38×10^{-23} J/K
Temperature	T	293 K
Substrate density	ρ	2650 kg/m^3
Substrate shear modulus	μ	29 GPa
Reference amplitude	$\lvert\psi_R\rvert$	10 pm
Cavity length	L_C	1 wavelength = 20 μm

Current MEMS magnetometers can achieve field sensitivities in the presence of noise ranging between 100-1000 $nT/\sqrt{Hz}$ [69]. Figure 6.3 shows the sensitivity dependence on increasing coupling array length for the mode localization magnetometer.

It can be seen that the transducer performance in the presence of noise improves as the number of periods in the coupling array are increased, however, diminishing returns

are found at larger device sizes. It is shown that the field sensitivity of sub-100 $nT/\sqrt{Hz}$ is achieved with a coupling array length of 360 periods. With the proposed parameter from Table 6.2, this would yield an overall device length of ~7mm. This presents the SAW mode localization magnetometer as a promising candidate for experimental prototyping and development.

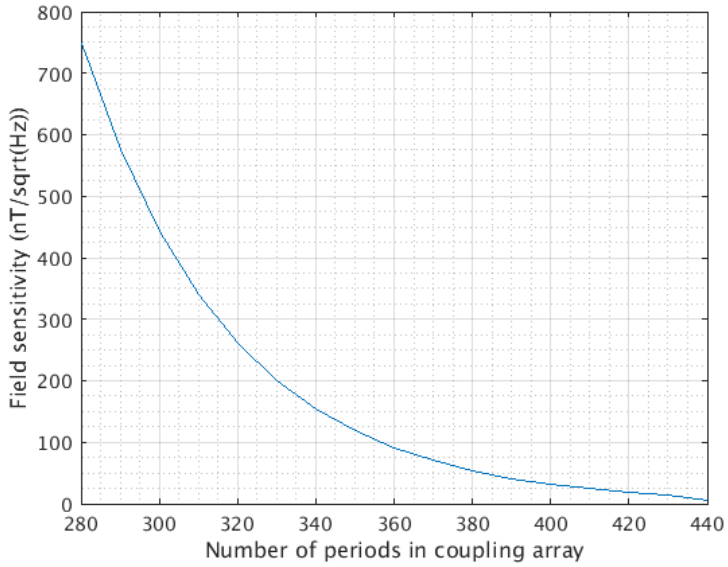

Figure 6.3 Change in minimum detectable magnetic field with length of coupling array.

6.4 Conclusions

A potential application for the SAW mode localization sensor has been presented in the form of a resonant MEMS magnetometer. The expressions found from previous chapters have been adapted to facilitate an analysis and comparison with the current capabilities of MEMS magnetometers. Specifically the resolution and size were addressed. This analysis will provide context to future experimental or theoretical calculations of the maximum achievable values of C_1 that can be achieved.

This analysis provides evidence for the potential performance that can be yielded by the SAW mode localization sensor. In addition, the device can be tuned further for increased sensitivity, albeit at the expense of device size.

Chapter 7. Prototype Design, Manufacture and Testing

7.1 Introduction

Two experimental prototypes were designed, manufactured and tested to provide evidence of the predicted phenomena as well as further validation of the model derived in chapter 3. The first device utilised an alternative geometry: a MEMS fixed-fixed beam with varying cross-section. This sought to demonstrate a high-Q, 'trapped' mode. The second device closely resembles that analysed in the preceding chapters, a SAW device consisting of two acoustically coupled cavities. It was intended to realise localization by tuning wave speed within the sense cavity using a variable external load.

No positive experimental results were found within the time constraints of the project, primarily due to damage to the experimental samples. Although no positive experimental results were achieved, experimental work is still ongoing within the team at Newcastle University. This chapter documents the prototype design, experimental set up and preliminary results produced as a result of the work within the previous chapters.

The chapter first details the design and analysis of the MEMS 'trapped mode' beam resonator. The SAW device is then addressed in terms of mask design, device manufacture and packaging. The experimental methodology is presented, detailing the measurement techniques and apparatus. The results of preliminary tests on the damaged die are the presented and discussed before conclusions are drawn in the closing section.

7.2 Design and analysis of a 'trapped mode' beam resonator

7.2.1 Introduction

As explored in detail in reference to the SAW mode localization sensor, the introduction of a disorder into a finite periodic oscillatory system induces the presence of a 'trapped mode': a mode in which the displacement field is localized to the region of the disorder. A main inhibitor to MEMS resonators achieving a high quality (Q) factor is energy

radiation through the support to the substrate. The trapped modes present a way to tune this support loss to a minimal value and thus are a good potential candidate for a high-Q geometry. An initial geometry is proposed and contrasted to a lumped-parameter model. Separate two-dimensional resonator and substrate COMSOL models are used in combination to determine an optimal geometry for a maximum support Q (Q_{SUPP}). The Q_{SUPP} is shown to be on the order of the highest currently available in the literature. The theoretical maximum achievable Q factor, due to other dominant Q contributions, is discussed.

The sensitivity of MEMS resonant sensors is dependent on a high quality (Q) factor. The Q factor can be described as the sum of the forms of dissipation that contribute to it (Equation 7.1). In MEMS devices, the most prominent of these are surface loss (Q_{SURF}), gas damping (Q_{GAS}), thermoelastic damping (Q_{TED}) and support loss (Q_{SUPP}) [83], [84].

$$Q_{TOTAL}^{-1} = Q_{SUPP}^{-1} + Q_{SURF}^{-1} + Q_{TED}^{-1} + Q_{GAS}^{-1} + Q_{OTHER}^{-1} \tag{7.1}$$

Q_{SUPP} is one of the dominant contributors to the overall Q of the resonator; this is quantified by Equation 7.2 [84].

$$Q_{SUPP} = 2\,\pi\,\frac{W_n}{\Delta W} \tag{7.2}$$

Where W_n and ΔW are the stored energy and energy loss through the support respectively. For a beam resonator vibrating its nth natural frequency, ω_n, the stored energy can be described by Equation 7.3. Where ρ, A and L are the density, cross sectional area and length of the beam respectively. U_n is the vibration amplitude [85].

$$W_n = \frac{1}{8}\rho A L \omega_n{}^2 U_n{}^2 \tag{7.3}$$

The energy lost through the support can be written in terms of the shear force, F_S, and the displacement field, u, at the beam-substrate interface [84]. The contribution due to the bending moment can be neglected [86].

$$\Delta W = \pi F_S u_{x=0} \tag{7.4}$$

The Q_{SUPP} can be optimised by designing a resonator geometry so that the oscillating force, F_S, at the support interface is minimized, and the energy stored, W_n, in the bulk of the resonator is maximized. A structure exhibiting a trapped mode would be an ideal candidate for a high Q_{SUPP} resonator. One class of finite periodic system that can exhibit trapped modes are stepped beams. These can be easily integrated into planar systems and are well suited for use as isolating tethers, wave guides, delay lines or resonant sensors.

The particular geometry of interest is elucidated in Figure 7.1. Slender Euler-Bernoulli (EB) beams are separated by much thicker sections of the beam, which do not themselves fall within the bounds of EB assumptions.

Figure 7.1 Mode shape and geometry of the trapped mode beam resonator. The distal ends are clamped and the central slender section is mistuned in thickness from the surrounding slender beams. Therefore a mode exists in which vibration is localized to the central beam.

It has been shown experimentally that as little as three periods of such a system excited in the stop band can enable a complete decay of the displacement field [87]. The present analysis focuses on a 4.5 period beam, with the displacement field localized to the central region (Figure 7.1).

7.2.2 Lumped parameter model

An equivalent lumped parameter model was employed to gain initial insight into the parameters of interest. This is presented here, along with the underlying approximations.

In the global mode shape of interest (Figure 7.1) the EB beam sections will be oscillating locally in their first mode, therefore they are modelled with a single degree of freedom. This limits the analysis to the first band gap. The larger sections of the

beam are assumed to experience minimal deformation. To simplify the model and reduce the degrees of freedom, zero elastic deformation is assumed and therefore these are also modelled with one degree of freedom. The sections can be connected to form the full 4.5 period equivalent system of interest (Figure 7.2).

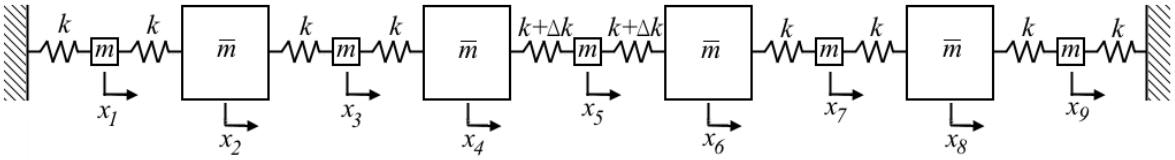

Figure 7.2 Lumped parameter model of the trapped mode beam resonator

The general non-dimensionalised eigenvalue problem for the non-localised system is given in equation 7.5. The form of the stiffness and mass matrices are given in equations 7.6 and 7.7 and respectively.

$$(\mathbf{K} - \lambda\,\mathbf{M})\underline{x} = [0] \tag{7.5}$$

$$\mathbf{K} = \begin{bmatrix} 2 & -1 & & & & & \\ -1 & 2 & -1 & & & & \\ & -1 & 2 & & & & \\ & & & \ddots & & & \\ & & & & \ddots & & \\ & & & & & 2 & -1 \\ & & & & & -1 & 2 \end{bmatrix} \tag{7.6}$$

$$\mathbf{M} = \begin{bmatrix} m_r & & & & & & \\ & 1 & & & & & \\ & & m_r & & & & \\ & & & \ddots & & & \\ & & & & \ddots & & \\ & & & & & 1 & \\ & & & & & & m_r \end{bmatrix} \tag{7.7}$$

$$m_r = \frac{m}{\bar{m}}, \qquad m_r < 1, \qquad m_r \neq 0 \tag{7.8}$$

A simple numerical analysis can be performed for the non-dimensional case by perturbing the stiffness matrix (the change in mass is assumed negligible). Equations 7.9-7.11 are substituted into equation 7.5.

$$\mathbf{K} = \mathbf{K_0} + \boldsymbol{\delta}\mathbf{K} \tag{7.9}$$

$$\boldsymbol{\delta}\mathbf{K} = \begin{bmatrix} \mathbf{0} & & & & & & \\ & \cdot & & & & & \\ & & \boldsymbol{\delta_k} & -\boldsymbol{\delta_k} & & & \\ & & -\boldsymbol{\delta_k} & \mathbf{2}\boldsymbol{\delta_k} & -\boldsymbol{\delta_k} & & \\ & & & -\boldsymbol{\delta_k} & \boldsymbol{\delta_k} & & \\ & & & & & \cdot & \\ & & & & & & \mathbf{0} \end{bmatrix} \tag{7.10}$$

$$\delta_k = \frac{\Delta k}{k}, \qquad \delta_k \ll 1 \tag{7.11}$$

A quantity is required that is comparable to Q_{SUPP}. In order to maximize Q_{SUPP}, the stored energy at the centre must be maximized and the energy at the ends minimized. Solving the perturbed EVP will yield a localised mode, x_L, from which the potential energy for the central and end masses can be calculated. The ratio of these is assumed to be proportional to the support loss. Thus, an 'energy localization coefficient', ζ, is defined by taking the ratio of the strain energy stored in the central (5^{th}) DOF to the energy stored in the end (1^{st} and 9^{th}) DOFs (equation 7.12).

$$\zeta = \frac{(1 + \delta_k)\left|x_L^{(5)}\right|^2}{\left|x_L^{(1)}\right|^2 + \left|x_L^{(9)}\right|^2} \tag{7.12}$$

The change in ζ with varying mass ratio, m_r, and stiffness perturbation, δ_k, is shown in Figures 7.3-7.4. It must first be noted that the cases when either $m_r = 0$ or δ_k =-1 are both unphysical and are to be ignored in the analysis. It can be seen from both Figures 7.3 and 7.4 that when $|\delta_k| > 0$, ζ asymptotically tends to infinity as as m_r approaches zero. In addition to this, Figure 7.4 shows that the rate of change of the gradient increases with increasing δ_k. It is shown in Figure 7.3 that ζ approaches a maximum at an optimal value of $\delta_k \approx$ -0.5.

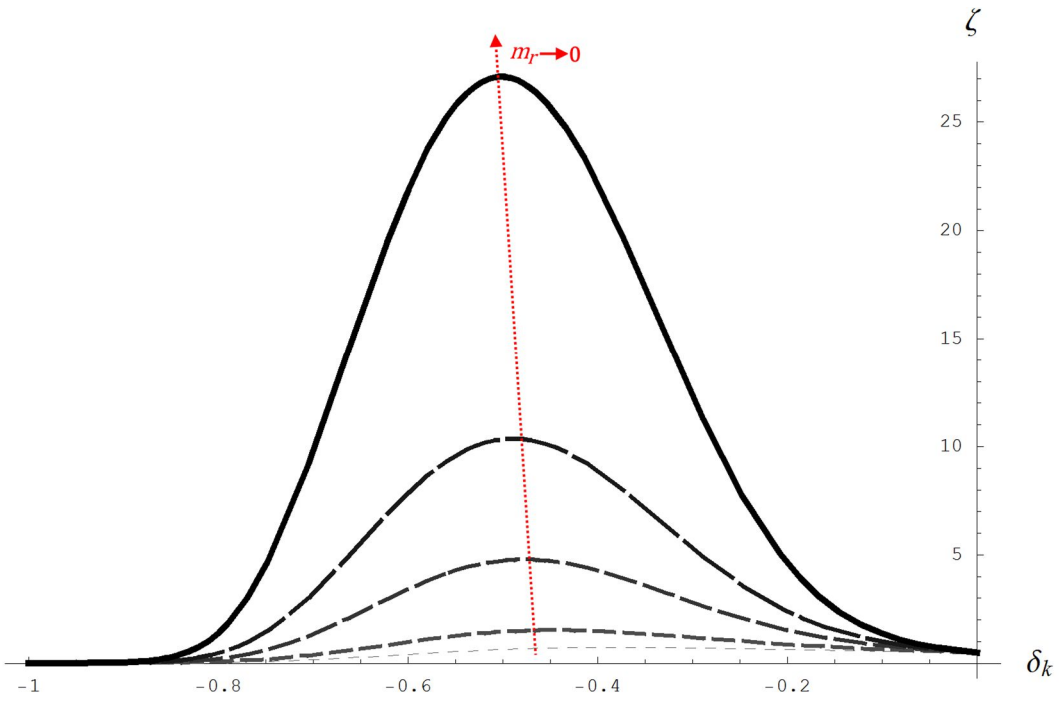

Figure 7.3 Plot of ζ, the localization coefficient, against the non-dimensional stiffness perturbation for thicker lines as the mass ratio tends to zero.

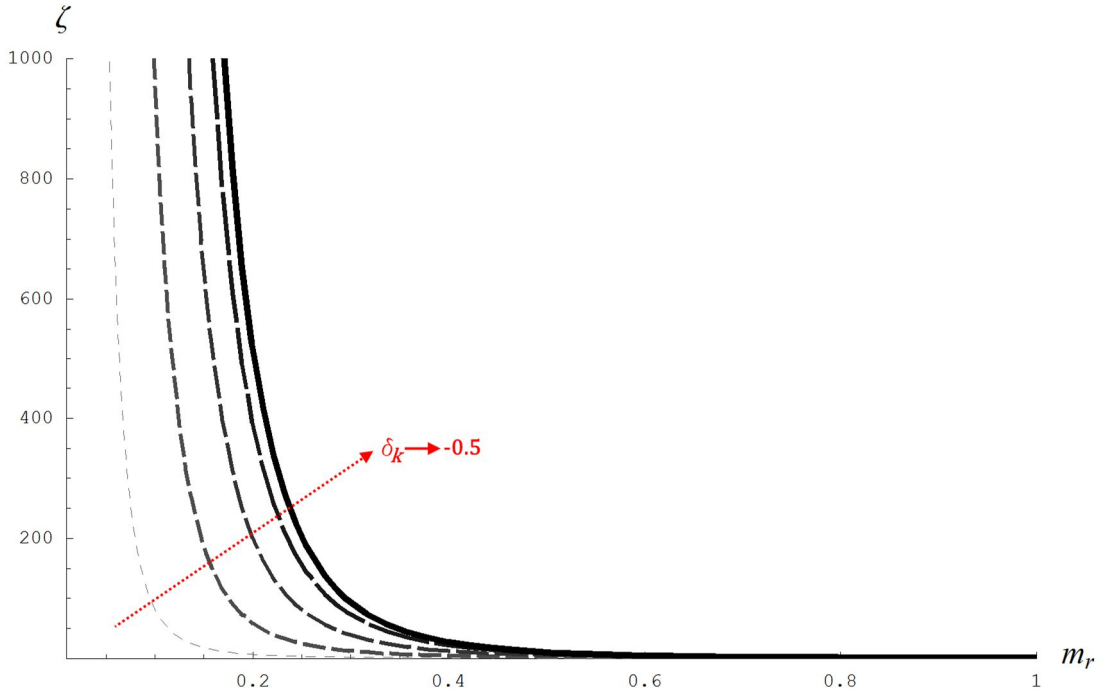

Figure 7.4 Plot of ζ, the localization coefficient against the mass ratio for thicker lines as δk tends to -0.5.

7.2.3 COMSOL models

Two separate 2D models were used for the resonator and substrate, both using silicon material properties. The resonator geometry (Figure 7.5) was halved and replaced by a symmetry boundary in the centre of the central slender beam section. This assumes that the energy loss at each boundary is equal and uncoupled. The substrate model (Figure 7.6) consisted of three concentric semicircles, the smallest of which defined the loaded region, and the others to defined the total substrate region and a perfectly matched layer (PML).

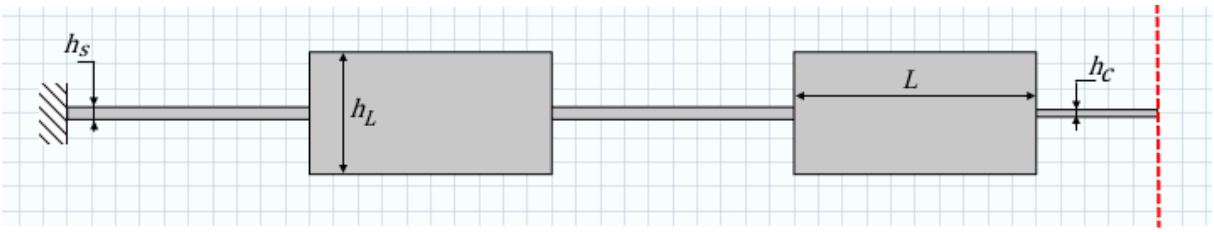

Figure 7.5 Geometry and geometric parameters used for the trapped mode beam finite element model.

Meshing for both models was predominantly accomplished using free quadrilateral meshing. A mapped face mesh was employed for the slender sections in the resonator model. The meshed model of the substrate and the displacement field solution are shown in Figures 7.7-9.

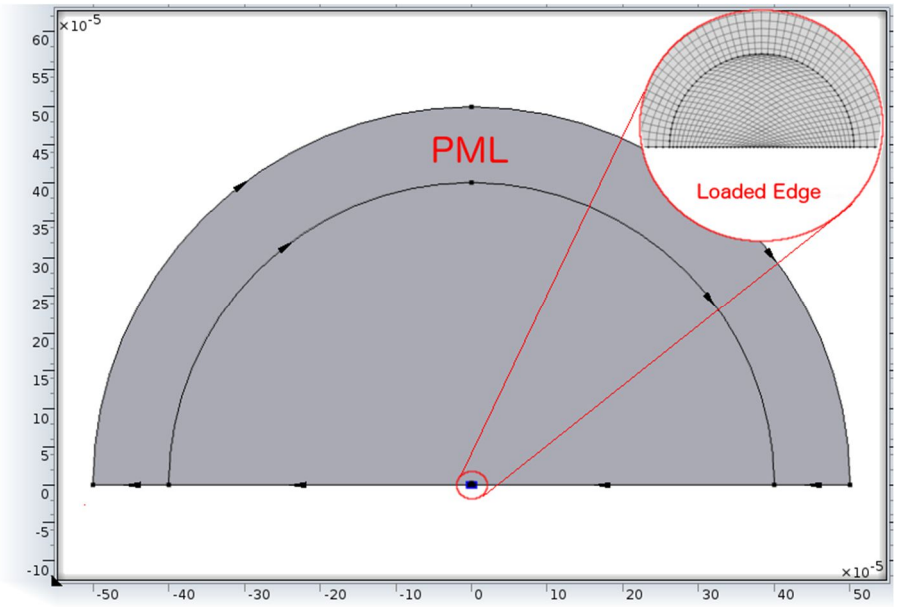

Figure 7.6 Substrate geometry used for the finite element model to calculate energy lost through the support. PML shown and mesh of loaded edge depicted in inset.

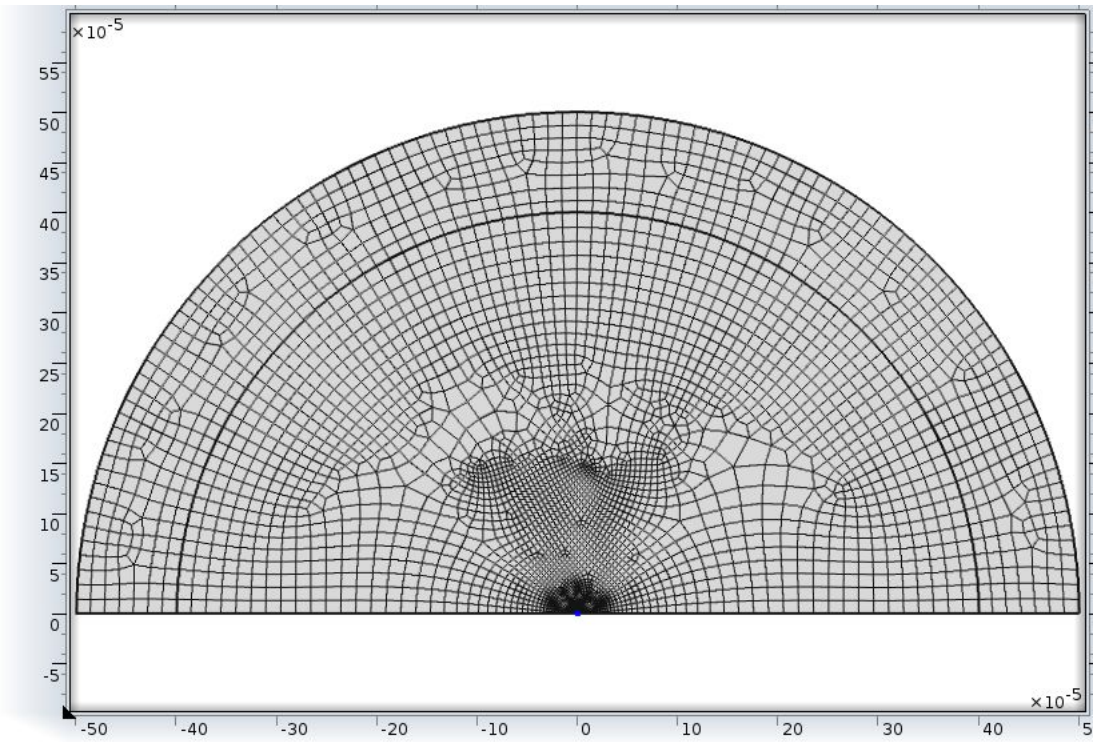

Figure 7.7 Fully meshed of substrate model.

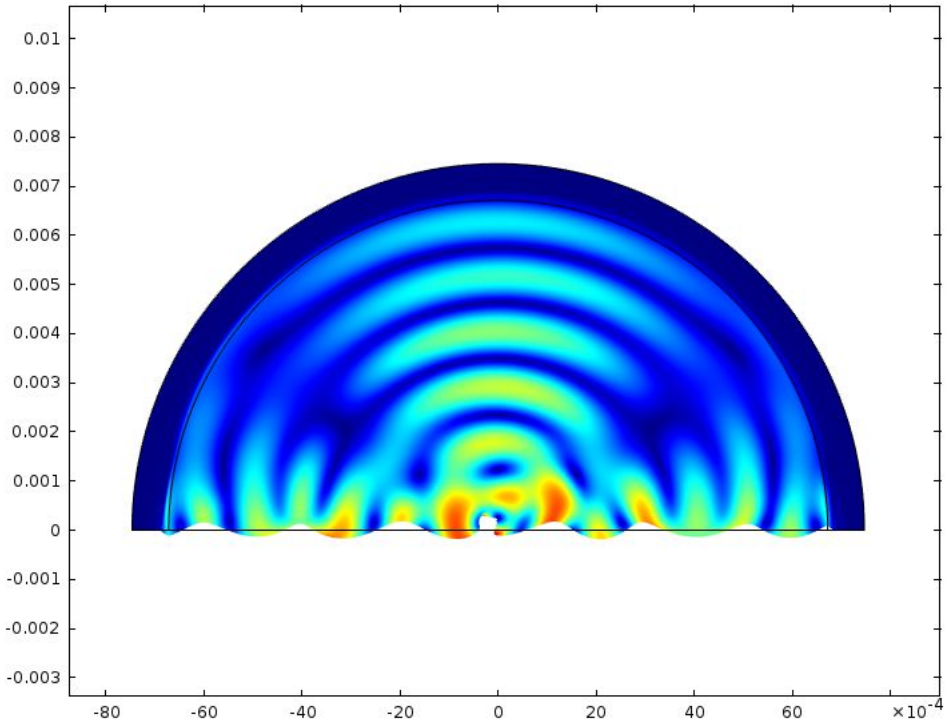

Figure 7.8 2D view of displacement field in substrate used to calculate support loss.

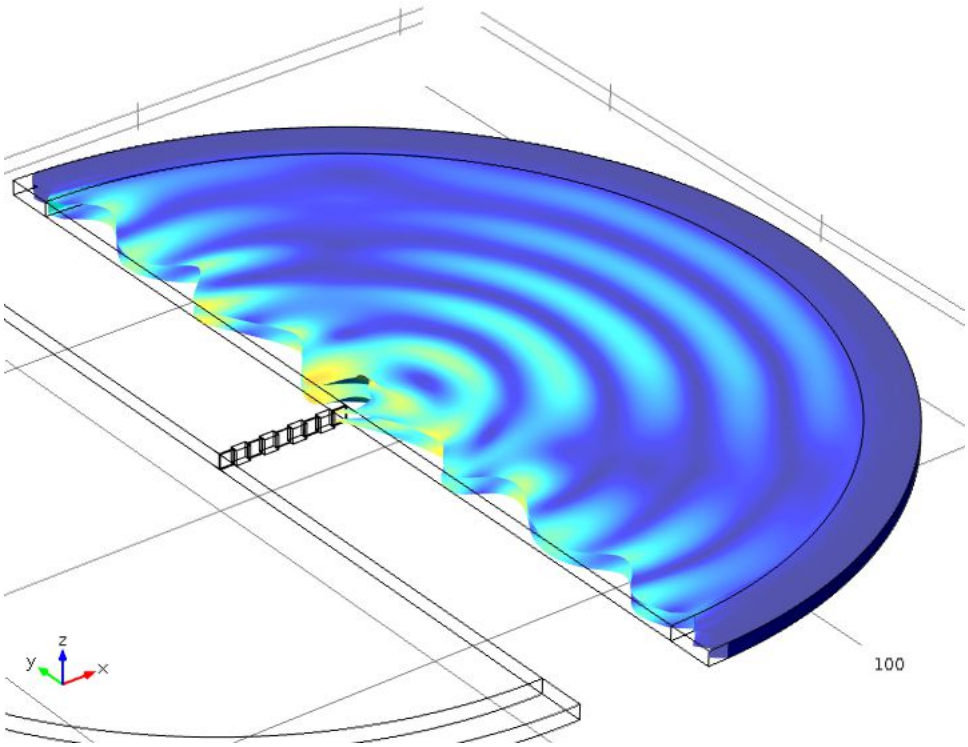

Figure 7.9 3D view of displacement field solution in substrate used to calculate support loss, with beam geometry shown in wire frame to exemplify the full coupled system.

The dimensions of the resonator geometry are summarised in Table 7.1.

Table 7.1 Trapped mode beam resonator dimension summary

Parameter	Symbol	Value
Length of beam sections	L	100 μm
Thickness of slender beams	h_S	5 μm
Thickness of central slender beam	h_c	1.25 - 5 μm
Thickness of large beam sections	h_L	50 - 100 μm

COMSOL's post processor provided a value for the stored energy. This was compared to an analytical calculation of the sum of the energy (equation 7.3) stored in each of the slender beam sections, with the displacement amplitudes taken from the COMSOL solution. These were found to agree to within 20%, with an average difference of 15%. The difference can most likely be attributed to energy stored in the thick beam sections that is neglected in the analytical comparison calculation.

The shear stress can also be taken directly from COMSOL, however, due to the sharp changes in cross section, an extremely fine mesh would be required to achieve a consistent result. To allow for a coarser mesh and faster computation times, the shear force was calculated from equation 7.4 using the displacement solution from Comsol.

A parametric sweep ran through the desired values of h_L and h_c as defined in Table 7.1. The required data was taken from the 5th Eigenmode output from an Eigenfrequency analysis.

The substrate model was used to quantify the energy radiated away from the resonator per cycle. Referring to equation 7.4 it can be seen that the displacement field across the loading region is required as output from this model. Frequency and shear load solutions gleaned from the resonator solution were input into a parametric sweep for a Frequency Domain analysis.

7.2.4 Discussion

The results from the COMSOL models were combined with equations 7.2-7.4 and a maximum value sought. The parameter space solved for is plotted in Figure 7.10.

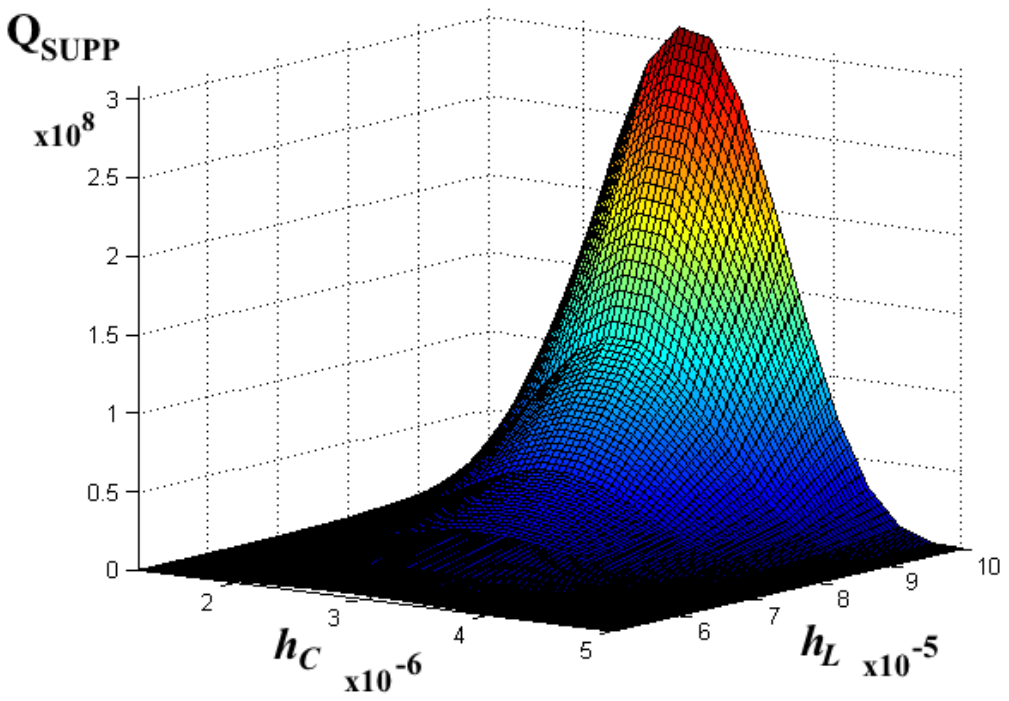

Figure 7.10 Surface plot of the support Q against central beam and large beam thicknesses.

The maximum Q_{SUPP} achieved was ~$3x10^8$ which corresponded to a step thickness ratio of 20 and a disorder thickness ratio of 0.45. These values correspond to $m_r = 0.05$ and δ_k ⊠-0.8. The contour plots (Figure 7.11) compare the COMSOL solution and the lumped parameter solution. In general, good qualitative agreement is found within the bounds of validity of the perturbation solution.

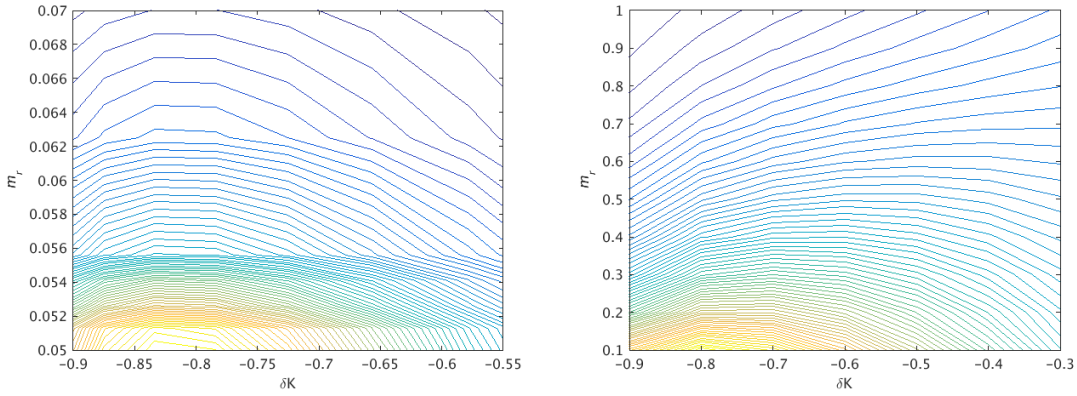

Figure 7.11 Contour plots comparing the qualitative behaviour of the lumped parameter and Comsol solutions. The left hand plot depicts the Comsol solution and the right hand plot the lumped parameter solution.

Quoted values for Q_{SUPP} are sparse in the literature, however, the TMBR compares favourably to the values available. Two examples of note are for a xylophone bar resonator (XBR) [69], [83] and a micro-cantilever [84]. Contrasting these to the TMBR, the TMBR Q_{SUPP} is found to be of the same order or greater.

The numerical value given for Q_{SUPP} is dependent on the scale of the device. Therefore, it is more useful to compare the parameters affecting the Q_{SUPP} and the limits imposed by them. In the case of the TMBR the Q_{SUPP} is limited by the maximum thickness ratio, which is equivalent to the wave-speed ratio, V_R, between the segments.

Therefore, the Q_{SUPP} is limited by the mass the slender beams can support. Increasing V_R provides a simple method for increasing the Q_{SUPP} in a TMBR. The Q_{SUPP}, however, only needs to be tuned to a value where it is no longer the dominant form of dissipation. After this, efforts should be focused on reducing the new dominant dissipation mechanism to achieve the maximum Q_{TOTAL}.

Q_{SUPP} is limited in general by geometric factors. Tuning to optimise these may affect the other Q contributors, leading to a compromised Q_{TOTAL}. It is reasoned in this section

that in the case of the TMBR, the parameters determining the other dominant Q contributors are uncoupled from the Q_{SUPP} tuning parameters.

The dominant Q contributors for a silicon MEMS resonator operating in a vacuum are Q_{SUPP}, Q_{TED} and Q_{SURF} [84]. Calculating the equivalent values of these quantities for coupled systems [69] takes advantage of the fact that both Q_{TED} and Q_{SURF} are local dissipation mechanisms [88].The Q_{TED} expression reduces to one dimension by assuming negligible axial heat flux. When this is combined with the assumption that the strain in the thick section of the beam is negligible, it implies that the Q_{TED} is determined solely from the slender beam sections. Similarly, Q_{SURF} is a fundamentally local dissipation mechanism [88] and the geometric dependence is predominantly the beam thickness [69]. Thus, both Q_{TED} and Q_{SURF} are unaffected by the main Q_{SUPP} tuning parameter, $\frac{h_L}{h_S}$.

From this is it not unreasonable to assert that a set of geometric parameters can be found that provide a Q_{TED} and Q_{SURF} in line with the highest found in the literature for a beam resonator, whilst still maintaining the same $Q_{SUPP.}$

7.2.6 Conclusions

It has been shown that a Q_{SUPP} value for the TMBR can theoretically be achieved of the order of those currently available in the literature and can be increased or decreased by altering the wave-speed ratio between segments. In addition, it has been reasoned that the other dominant Q contributors can be tuned with minimal effect on the achievable Q_{SUPP} value. The use of the equivalent lumped parameter model for obtaining qualitative information about TMBR systems has been validated. The given conclusions indicate that the TMBR geometry can be a suitable choice as a MEMS resonator as a support structure for other resonant devices.

A device was manufactured in order to experimentally validate the conclusions of the analysis, a microscope image of one of the die including three trapped mode beam resonators is shown in Figure 7.12.

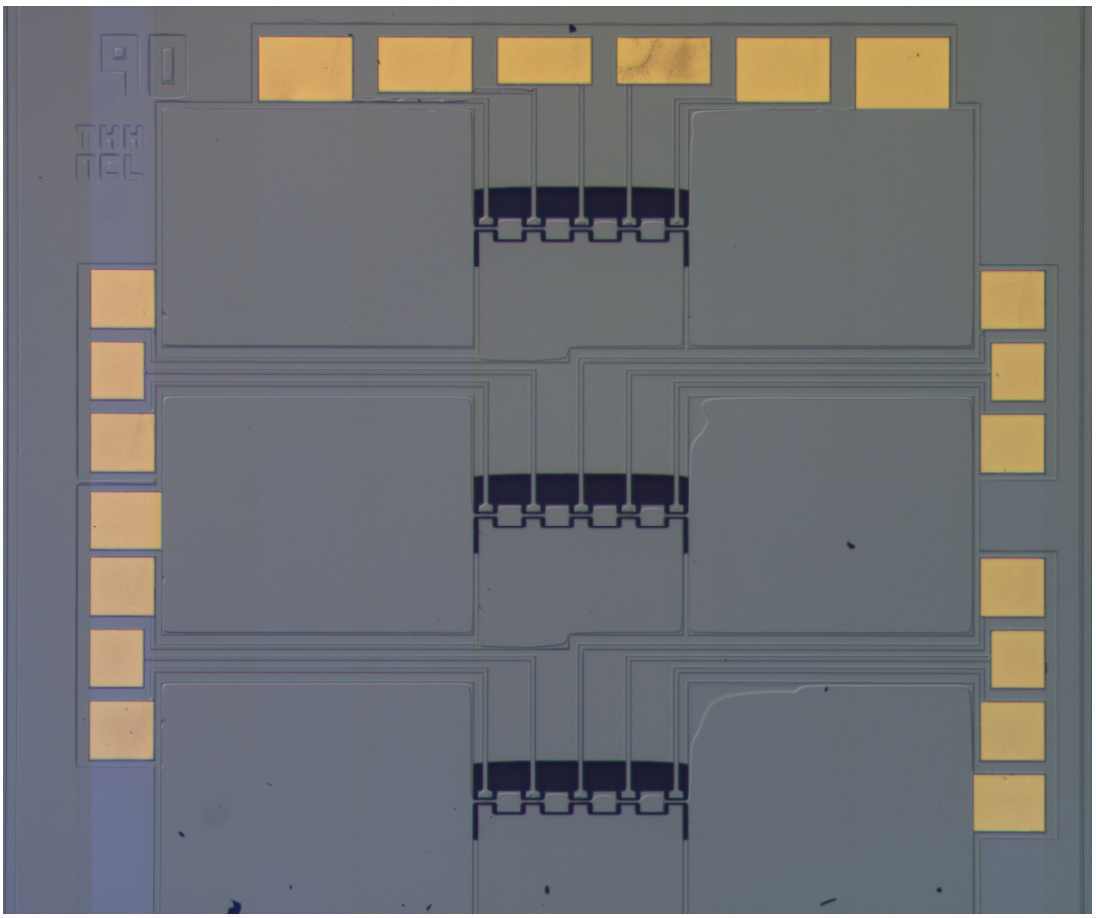

Figure 7.12 Optical microscope image of a MEMS die containing three trapped mode beam resonators.

When the device was placed within a vacuum a high-Q mode was detected near the frequency of interest using a Laser Doppler Vibrometer. This result, however, has not yet been found to be sufficiently repeatable and further work is planned to validate the analysis. This includes repeat observation of the high-Q peak as well as mapping of the characteristic mode shape of the 'trapped mode'.

7.3 Design and manufacture of a prototype SAW mode localization sensor

7.3.1 Device geometry

The device geometry was designed to be multi-purpose and capable of yielding results for various experiments. In particular, a previous experiment for a conference paper [36] by the author. This related work was seeking to demonstrate tuning of the coupling array and evaluate the use as a sensor. Due to this the device is symmetric about the centre of the coupling array and will not exhibit localization without the use of external circuitry. Within this section the details of the geometry and design are presented.

The device is constructed from 150nm thick aluminium strips deposited on YX128-$LiNbO_3$, the free surface wave speed of which is widely reported as 3995 m/s [60]. The wave speed within the plated regions can be calculated using the equations of section 3.2.3. It is detailed in reference [42] that aluminium strips of this thickness load the substrate and perturb the wave speed to approximately 97.3% of its original value. An overview of the layout is shown in Figures 7.13-15.

The dimensions were chosen to operate with a nominal wavelength of 20 µm, therefore the period of the arrays and IDT's is 10µm. The substrate wave speed is 3995m/s, this indicates the operating frequency range to be near 199MHz. The enclosing arrays consist of 250 reflectors each to ensure near total reflection, calculated using the model presented in chapters 3 and 4 and available in appendix C. The coupling array is 100 periods long to allow approximately 50% transmission and the IDT's each consist of 5 fingers. There are two IDT's per cavity, allowing tuning in both cavities if desired, as well as giving the option of electrical sensing in both cavities. The IDTs are labelled depending on their chosen function, excitation, sensing or tuning.

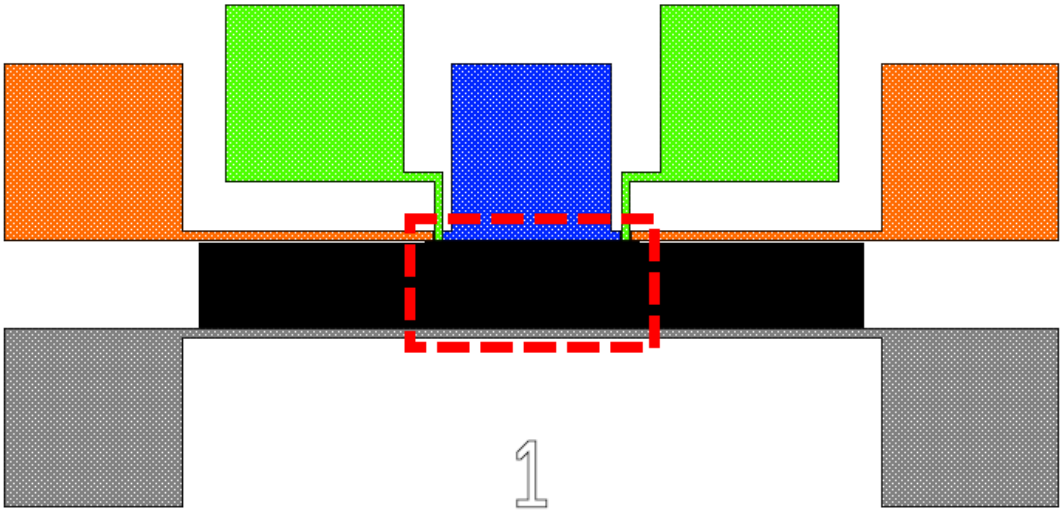

Figure 7.13 Full overview of the SAW device layout. All shaded regions represents regions of Aluminium deposited on the substrate. The orange, green and blue shaded regions are the excitation, sense and coupling IDT tracks and pads respectively. The grey shaded region is ground pads. The red box indicates the region containing the cavities and coupling array as shown in Figure 7.5. Outside of the red box to the left and the right are the enclosing array reflectors.

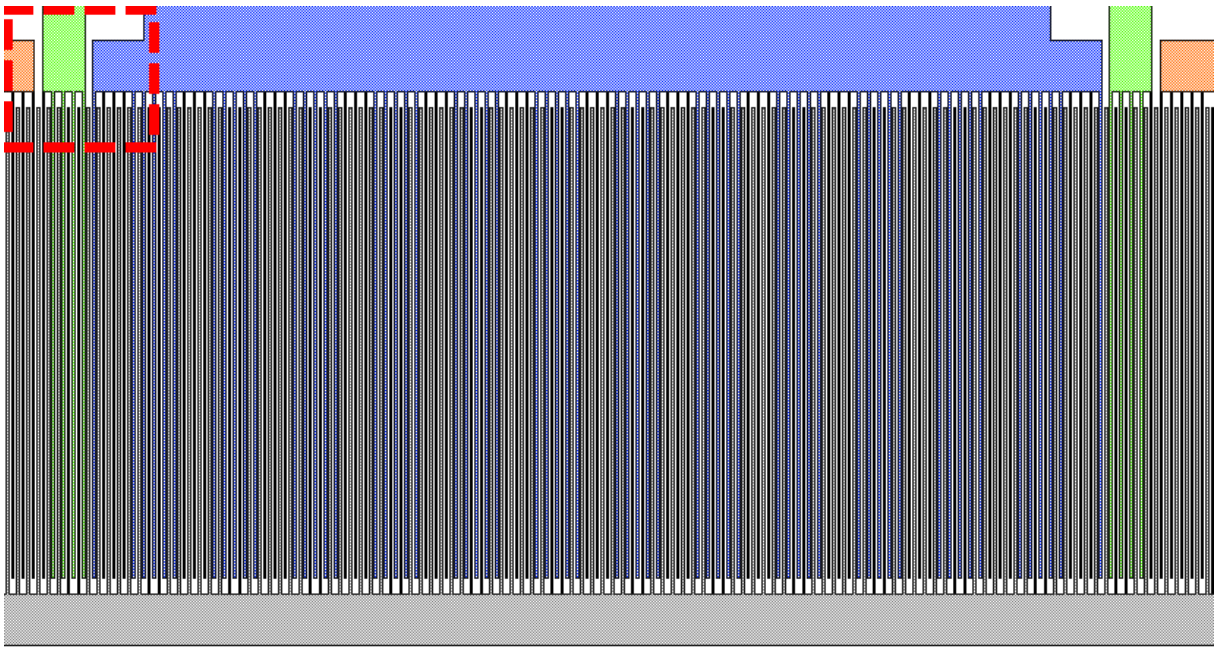

Figure 7.14 Enlarged view of the cavities and coupling array. The red box represents the region shown in Figure 7.6. It can be seen that the ground bus bar running along the bottom of the device connects to every second finger.

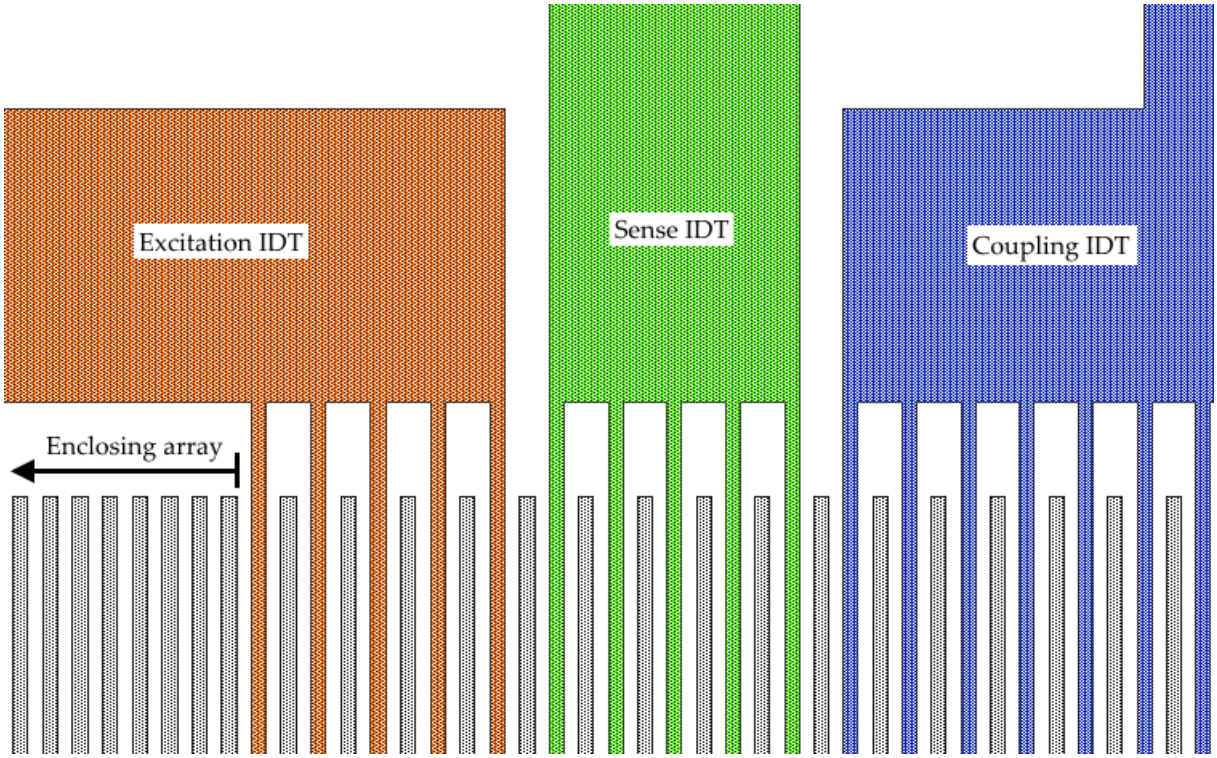

Figure 7.15 Enlarged view of the IDT fingers and enclosing array reflectors displaying the structure of the device. Each finger is five microns wide as is each space.

The device is symmetrical about the centre of the coupling array, and the IDT's are synchronous with the arrays, therefore localization would not naturally occur as no disorder exists in the system. In order to induce and tune localization, a load is attached across the sense IDT, locally perturbing the wave speed. The localised response will occur in proportion to the impedance of the load applied and hence demonstrate the potential for device operation; this is discussed in the following section.

7.3.2 Wave speed tuning

It is shown in reference [59] that a varying of the impedance of a load connected across an IDT locally alters the effective wave speed. This phenomenon will be employed in order to initiate localization to validate the potential use as a sensor.

In reference [59], tuning of a SAW resonator was demonstrated using a device constructed of aluminium strips on YZ-LINbO$_3$. Both resistive and capacitive impedances ranging from 10-10kOhms were shown to be capable of varying the wave speed by 1.5%.

A simple diagram of the electrical experimental set up is shown in Figure 7.16. The external impedance in this case will be resistive. A potentiometer is connected across the sense IDT allowing the load to be adjusted easily between experimental runs. The real load seen by the IDT, accounting for resistance in the cables and bonds will be measured across the IDT terminals using a multimeter.

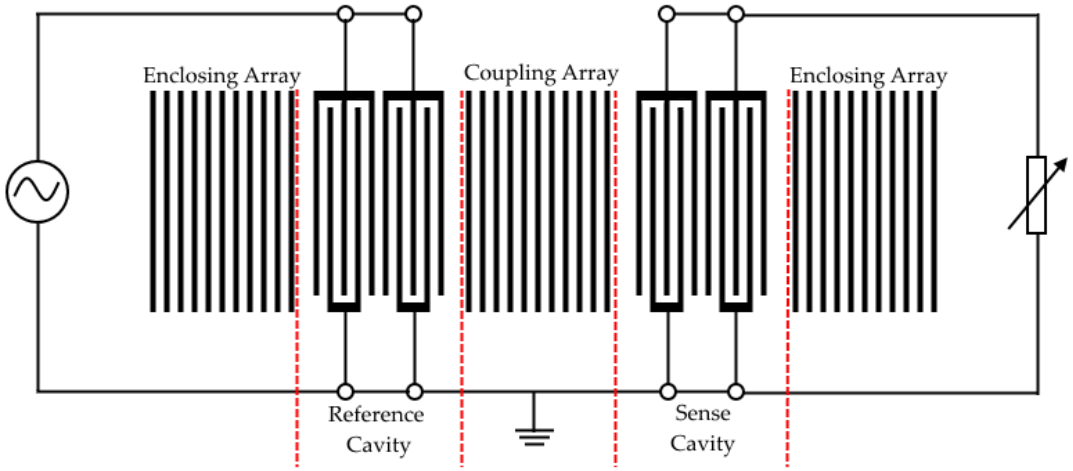

Figure 7.16 Simplified diagram of the initial experimental drive and tuning arrangement.

7.3.3 Die Manufacture

The die were manufactured using a photolithographic process, whereby first the YX128-$LiNbO_3$ substrate is sputter coated with a thin film of aluminium. A photoresist coating is deposited on top and selected areas, according to the mask of section 7.3.1, are exposed to light. The photoresist is then removed in the selected regions, exposing the aluminium to be etched away. After the aluminium etch, the remaining resist is removed leaving the patterned aluminium on YX128-$LiNbO_3$ die. The manufacturing process flow is shown graphically in Figure 7.17.

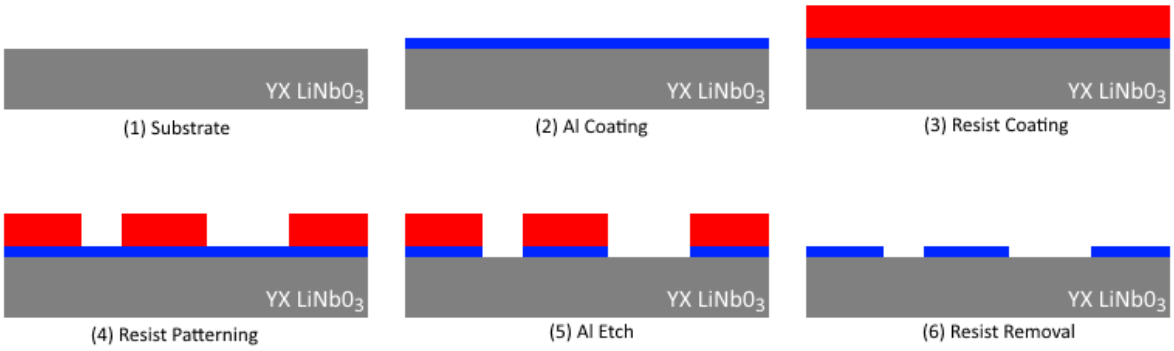

Figure 7.17 Process flow of the SAW device manufacturing process.

7.3.4 Packaging

The die were adhered into a 28-pin dual in-line package (DIP) using epoxy and wire-bonded to the package terminals. An image of the die affixed within the package, pre-wire-bonding is displayed in Figure 7.18.

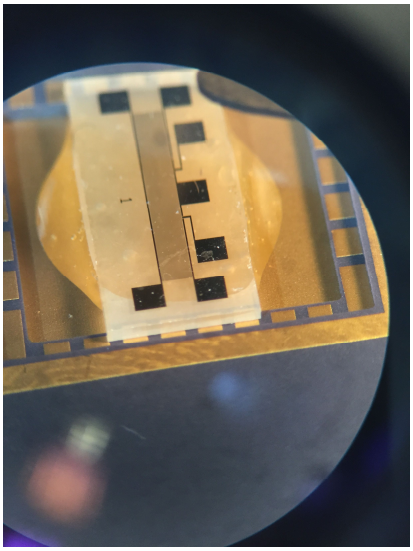

Figure 7.18 SAW device affixed in the DIP package with epoxy

The use of the 28-pin DIP allowed for utilisation of a pre-existing vacuum chamber. This could accept the DIP and routed the pins to SMA connectors using coaxial cables suitable for carrying the RF signals necessary for transduction. An image of the packaged die within vacuum chamber are shown in Figure 7.19.

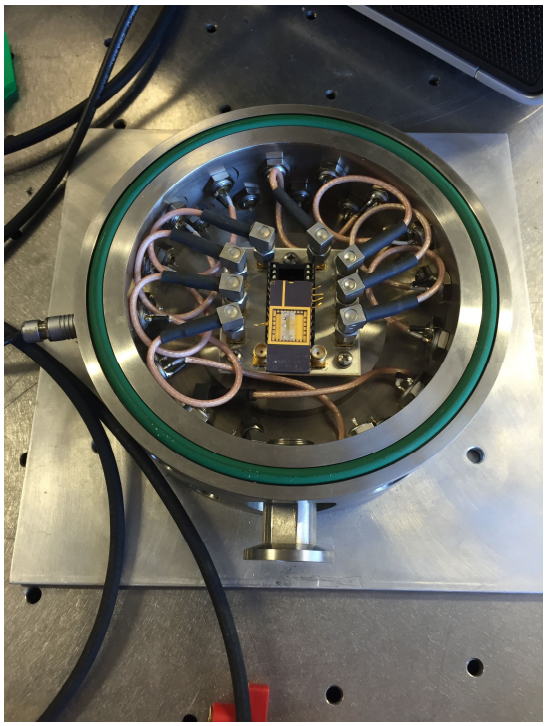

Figure 7.19 DIP located in vacuum chamber (lid not shown).

7.4 Experimental methodology

A schematic of the experiment is shown in Figure 7.20.

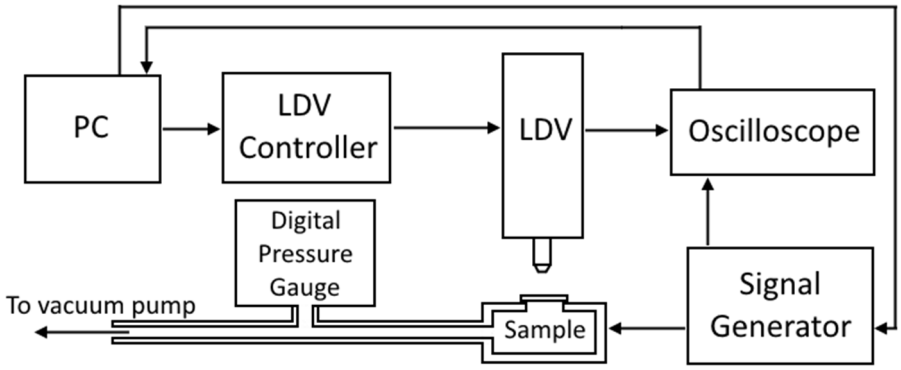

Figure 7.20 Experimental schematic

The setup is centred around the optical transduction unit of the Polytec UHF-120 Scanning Laser Doppler Vibrometer (LDV). The device uses the Doppler shift of a measurement beam in comparison to a reference beam to directly measure the velocity of the target. This is then automatically integrated within the software to provide the displacement fields, of interest to this study.

Broadband excitation was provided using a Rohde & Schwarz SMBV100A vector signal generator, this was used to provide a white noise signal in the range of 195-205MHz with an amplitude of 1.7V. The output of the signal generator was split and sent to both the device and the LeCroy WavePro 725Zi-A 2.5GHz oscilloscope, for real time inspection of the excitation signal. The LDV output was also routed to the oscilloscope, this aided focussing of the laser for the optimal strength output as well as comparison with the input signal in real time. All devices were controlled using a PC and the proprietary Polytec PSV software.

The sample was held under vacuum within the chamber shown in Figure 7.19. This was pumped to a steady partial vacuum of 4.3×10^{-2} mbar as monitored on a digital pressure gauge, plumbed in-line with the chamber. To limit transferal of pump vibrations to the sample, the vacuum hose was routed through a sand filled bucket, to significantly reduce the hose vibrations arising due to the rotary pump.

7.5 Results and Discussion

The scanning function of the LDV was used to map a section of the device on the excited IDT. The device responded to white noise excitation of the forcing IDT, producing the frequency spectrum shown in Figure 7.21. The response over the peaks present around 199MHz were inspected. The response within the frequency band indicated on Figure 7.21 corresponds to a standing wave of approximately 20um wavelength. The displacement field corresponding to this frequency band is presented in Figures 7.22 and 7.23.

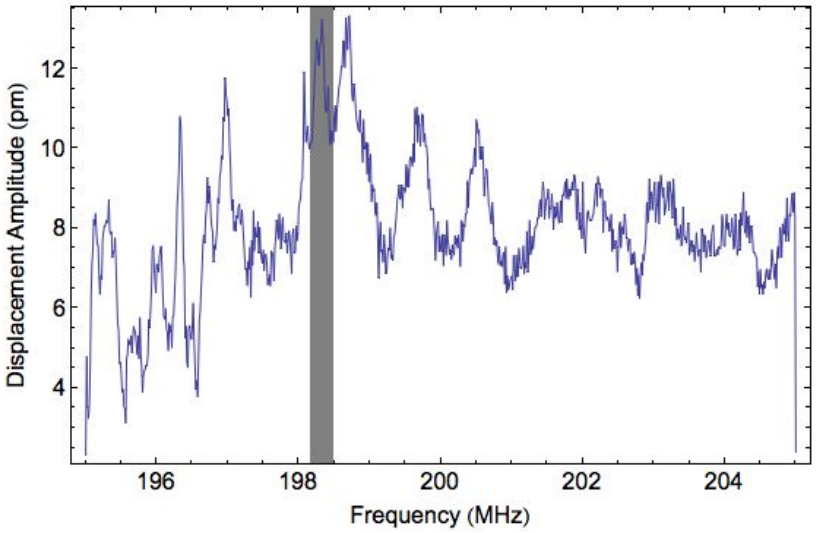

Figure 7.21 Measured frequency spectrum of a SAW prototype device. The response is relatively noisy with multiple similar sized peaks. The highlighted frequency band shows the peak near the modelled frequency of interest that produced the standing wave behaviour shown in Figures 7.12-7.13. The neighbouring peaks displayed travelling wave behaviour in the direction of interest.

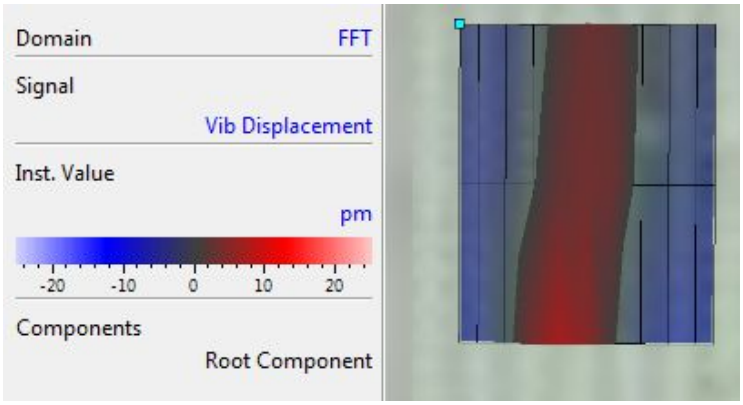

Figure 7.22 Top view of the measured displacement field.

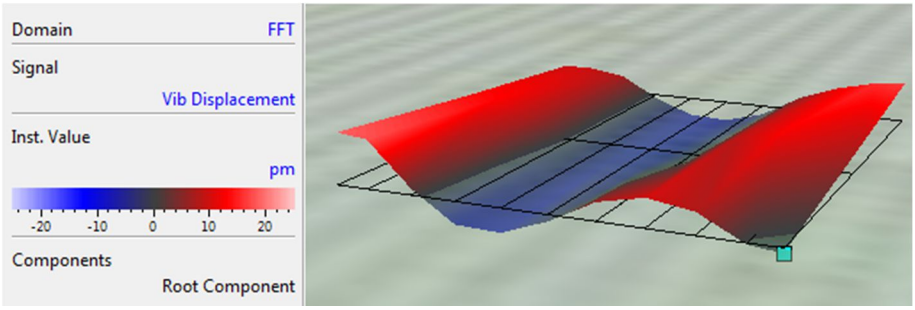

Figure 7.23 3D view of the measured displacement field.

It was found however that during pre-packaging transportation, the packaging process as well as post-packaging transportation the die developed damage to the IDT tracks that meant no positive evidence could be found with the current die. No single device had an intact IDT in both cavities, therefore one cavity could not be tuned to exhibit localization whilst the other was excited. Examples of the damage present on the die are shown in Figure 7.24. The most prevalent form of damage was a break in the long ground bus bar in the enclosing array region, between the pad and the IDT. This rendered all of the IDT's it served non-functional.

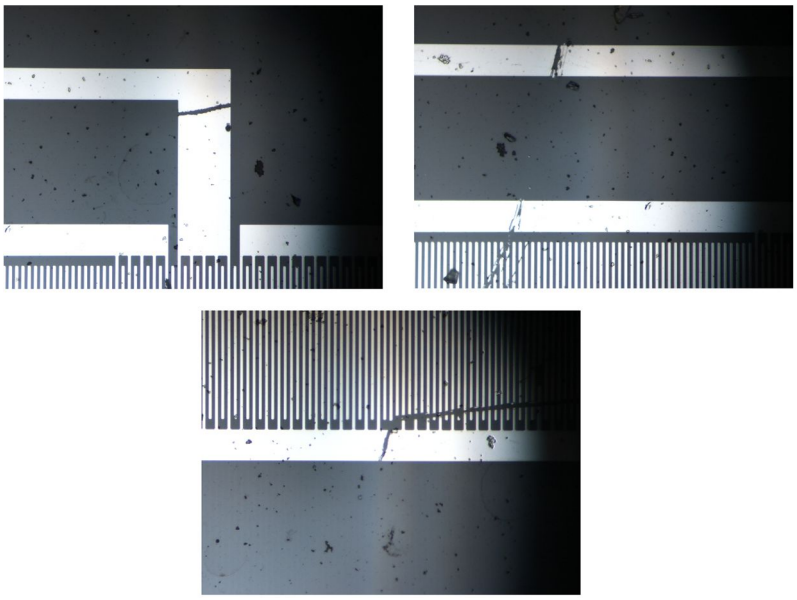

Figure 7.24 Examples of damage to thin film aluminium IDT tracks.

The cause of device damage can most likely be attributed to one of the following two sources:

- Accidental tweezer impact during the manual die pick or mounting process.
- Loose transportation between manufacture and packaging locations.

The manual process of die picking and mounting into the DIP packages is a risk that would need to be mitigated in a repeat experiment. One particular example of risk is the downwards pressure that needs to be applied when the devices are adhered into the package. This was applied with tweezers on the surface of the die, presenting a risk for scratching of the aluminium tracks. The risk of tweezer damage could be mitigated by the use of tools designed specifically for the purpose of picking and placing the die.

Transportation damage can be mitigated by packaging the die in the same location as manufacture. Furthermore, care must be taken in choosing the method to transport the packaged parts to the test lab.

7.6 Conclusions

Two separate experiments have been design, manufactured and a measurement methodology established. These aim to provide evidence to support the claims of this thesis as well as the related work completed in references [36], [89].

Due to the widespread sample damage, the devices used within the first round of testing were unable to exhibit the localization predicted within the theory. The devices however performed as predicted in the frequency range of interest, yielding a 20um standing wave resonant response within the excited cavity at approximately 199MHz. This has validated the experimental set up and characterisation technique for the ongoing further testing and future revisions of the device design.

At the time of writing the author is in continual liaison with researchers within the Mechanical Engineering School at Newcastle University. Experimental runs are ongoing and new samples are being designed and manufactured as required.

Chapter 8. Conclusions

8.1 Introduction

This chapter opens by restating and summarising the conclusions of the preceding chapters. The six open questions identified in the opening chapter are recalled and the answers provided to these questions by this thesis are outlined. Shortcomings of the study are highlighted and recommendations for further work are identified. Dissemination of the work is addressed, covering existing publications from this work as well as planned future publications. Finally, closing remarks are made.

8.2 Conclusions

8.2.1 Chapter 2

The basic geometry of the periodically-coupled SAW mode localization sensor was introduced (*section 2.3*) which allowed for the simplified lumped parameter model of the system to be constructed (*section 2.4.1*). A reduced order model was introduced alongside the LPM allowing, yielding analytical expressions of a form that could be compared directly to similar analyses in the literature (*section 2.4.2*). The reduced order model was shown to capture the majority of the behaviour of interest to device design and analysis.

The discussion of the physics of the system encapsulated the natural frequencies and normal modes (*section 2.5.1*), the frequency dependence of the periodic coupling array (*section 2.5.1*), the device level frequency response (*section 2.5.3*) and the device sensitivity (*section 2.5.4*). Alongside this the model was used to provide a mainly qualitative overview of the basic physics of the device operation (*section 2.5.2*). The device sensitivity was contrasted with an equivalent 2-DOF device in the literature (*Table 2.1*).

It was shown that the use of periodic coupling introduces an extra parameter (the number of periods) for tuning device sensitivity. The device was shown to response approximately linearly with respect to an introduced disorder and the sensitivity was

shown to have an exponential dependence on the number of periods in the coupling array.

8.2.2 Chapter 3

Chapter 3 yielded a comprehensive model of the wave dynamics of the SAW device with validation provided through FEM. The model provides insight into the physics of the device as well as forming the basis for fast numerical simulation of device behaviour. The model stemmed from the equations of linear elasticity (*section 3.2*), and the basis and prerequisites of the model were covered comprehensively (*sections 3.2-3.4*) before the expressions specific to the device were derived (*section 3.5*).

The model presented in section 3.5 was derived for a general geometry, with parameters such as cavity length, excitation location and array lengths not predetermined. Subsequently, expressions specific to the special case of the device geometry presented in chapter 2 were derived from the general solutions (*section 3.5.2*).

Good agreement was found between the derived model and an independent FEM analysis, validating the expressions (*section 3.7*). The validity of the model was discussed (*section 3.8.1*) and a comparison to the ubiquitous COM model was presented (*section 3.8.2*).

8.2.3 Chapter 4

The model derived in chapter 3 was utilised for a numerical investigation of the device behaviour. A primary tangible outcome of the work, a numerical code for fast computation of device behaviour, was introduced (*section 4.2/appendix B*). The utility of the expressions found in chapter 3 were discussed, specifically with reference to large increase in the speed of computation (*section 4.2*). The frequency response of the device was addressed in depth covering the conditions for resonance (*section 4.3.2*), the effect of the cavity length (*section 4.3.3*), coupling array tuning (*section 4.3.4*) and selective excitation (*section 4.4*). A comprehensive overview of the device behaviour was presented (*section 4.5*), detailing the behaviour of the natural frequencies (*section 4.5.2*) and the amplitude response in the context of device operation and sensitivity (*section 4.5.3*). The chapter concluded by presenting the calibration curve and linear approximation to the device response (*section 4.5.3*).

8.2.4 Chapter 5

The primary loss mechanisms of the SAW device were enumerated and their individual contributions quantified. These consisted of radiation loss (*section 5.2.1*), diffraction loss (*section 5.2.2*), bulk scattering (*section 5.2.3*), fluid damping (*section 5.2.4*) and material loss (*section 5.2.5*). The individual contributions to the overall device loss was discussed and quantified. It was found that device geometry could be tuned to make all forms of loss negligible when compared to the material loss. The likely impact of mechanical-thermal noise was addressed and expressions for the RMS noise amplitude, SNR and LOD were derived (*section 5.3*).

8.2.5 Chapter 6

An overview of the current-state-of-the-art in MEMS magnetometers was provided (*section 6.1*). A similar device to the one proposed by this work, the SAW delay line magnetometer, was introduced and details from literature provided (*section 6.2*). This provided evidence of the manufacturability of the device as well as realistic parameters to be used for this case study of the SAW mode localization sensor performance.

The design of the novel MEMS magnetic field sensor was presented and expressions for the field sensitivity and SNR were derived (*section 6.3*). By tuning the length of the coupling array it was found that competitive device sensitivity ($10^3\ nT/\sqrt{Hz}$) could be achieved.

8.2.5 Chapter 7

Detail of the design and implementation of two MEMS scale experiments was provided. The first experiment sought to employ an alternative geometry to the SAW device and was therefore addressed only briefly (*section 7.2*). Details of a conference paper arising from the work encompassing the analysis was provided.

The design of the first prototype SAW mode localization sensor was detailed. The device geometry was presented (*section 7.3.1*) alongside the principles of operation (*section 7.3.2*) and method of manufacture and experimental apparatus (s*ections 7.3.3, 7.3.4 and 7.4*). A brief overview of the results gained was provided, however, no experimental evidence of a functional SAW mode localization sensor was provided. This shortcoming was primarily due to wide scale device damage and time constraints.

8.3 Answers to open questions

- *How does using a periodic array as a coupler effect or enhance the operation of a mode localization sensor?*

This question was addressed primarily in chapter 2. The simplified model indicated that the main utility of the coupling array was the introduction to two parameters that could be used independently as a means of tuning the device sensitivity, namely the propagation constant and the number of periods. This result is general and common to all types of periodic arrays, be these acoustic waves or suspended MEMS structures (i.e. a cantilever array).

Further examples of the utility of the periodic array outlined above were shown in chapters 3 and 4, directly in relation to the SAW device. Additionally, the overt and practical benefit being that the periodic array is the simplest non-dissipative method of weakly coupling two SAW cavities.

- *Can a mode localization sensor be constructed using SAW?*

From a theoretical standpoint this question has been answered relatively conclusively within chapters 3 and 4. A model of the wave mechanics of the SAW system, constructed using minimal assumptions and inclusive of dissipation, exhibited behaviour mimicking that of the mode localization sensors described in the literature. This model was validated, showing a good level of agreement with a separate finite element model.

Experimental evidence of a functioning SAW mode localization sensor has remained elusive. However, the theoretical analysis and numerical validation provides substantial evidence that a device can function in this manner. The practical limitations on device size and performance however still require experimental validation before the results can be quoted with absolute confidence.

- *What are the benefits afforded by using the SAW platform and how can they be best exploited?*

One benefit was first alluded to in chapter 2: the use of a periodic coupling array provides a unique method of tuning the device sensitivity. This was reinforced throughout the thesis, with the coupling array length shown to have an exponential relationship with device sensitivity.

Chapter 5 and 6 provided evidence that the SAW platform is likely to be a low-loss and hence low-noise implementation of the mode localization sensor. This aligns with another area within microelectronics, filters, where bulk acoustic wave filters (BAW) were widely replaced by SAW as it provided superior noise performance [90].

The inherently robust design of SAW devices was asserted within the opening chapter, however, this runs contrary to the wide-scale damage and low yield found on the experimental prototypes. This indicates that the claim of greater robustness is only valid is sufficient device packaging procedures are in place.

- *What are the limits imposed on such a device by loss mechanisms and thermal noise contributions?*

Chapter 5 provided an analysis of the primary loss mechanisms affecting the SAW system. The loss mechanisms were shown to impose a limit on device size. The total loss of the device was used to calculate a first estimate of the thermal noise of the transducer; expressions were presented outlining the parameters contributing to the device SNR and LOD. It was shown that device geometry and viscous losses to the material were two factors that needed to be considered to produce a device exhibiting low thermal noise.

- *Does the SAW mode localization sensor present a viable platform to construct a competitive MEMS magnetometer?*

Chapter 6 directly addressed this question, first providing a novel device design of a MEMS SAW mode localization magnetometer. The calculations showed the performance in terms of the magnetic field sensitivity in the presence of noise is likely to be competitive. This provides evidence that the platform is likely to be viable. Experimental evidence to support this is not currently forthcoming in the time scale of

this research. The analysis, however, provides evidence that this would likely be a fruitful direction of further study in the field of MEMS magnetic field sensors.

8.4 Further work

8.4.1 Model improvements

The model produced in this work focussed on the elastodynamic properties of operation, neglecting the electrical properties of the device as well as the interaction with external networks. This was identified as the initial area that required investigation to determine the mechanics of the device operation. The end product of such a device described within this thesis would be a transducer component within an electrical circuit. Further work to model the system level performance would provide greater insight to the important parameters in device design.

8.3.2 Experimental work

The most fruitful focus of further work on this topic would be to obtain experimental data of the phenomena described. Initially, proof of concept and performance using the device design presented in section 7.3 is required. This will allow critique of the performance predictions of the loss and noise analysis. Furthermore, manufacture and testing of the MEMS magnetometer has not yet been performed. This will likely will require process development and research to obtain the correct magnetostrictive film performance.

8.3.3 Applications

There is much scope to expand the ideas presented within this thesis towards specific applications. One of these, a MEMS magnetometer, has been explored within the case study of chapter 7. Another application that presents itself is as a biological mass sensor. MEMS based bio-analyte detectors are often suggested in the literature. One common problem is that to function as a useful sensor in this field, these need to operate whilst submerged in a biological fluid. This can induce multiple failures in many common MEMS structures, in particular stiction or fracturing due to the fluid load. However, the main limitation is the Q-degradation associated with losses to a viscous fluid. Many of the proposed MEMS bio-mass sensors depend on high-Q to operate as does the SAW mode localization sensor. The SAW mode localization sensor

however presents potential solutions to these issues. The geometry will not fail due to stiction or fracture and Q-degradation can be addressed by the use of Love waves. These shear surface waves present no out-of-plane motion and therefore do not radiate energy to the fluid, thus the device can maintain a high Q. Therefore, focus of further study on a Love wave mode localization sensor may prove fruitful in this field.

8.5 Dissemination

Subsets of the work carried out during the period of candidature have been presented at three international conferences:

- The initial steps of the mathematical model were presented at the International Conference on Vibration Problems (September 2013, Lisbon, Portugal).
- The analysis of the first experimental design was presented at the 2014 COMSOL conference (September 2014, Cambridge, UK).
- The concept and parts of the analysis of the SAW mode localization sensor were presented at the 13th International Conference on Dynamical Systems: Theory and Applications (December 2015, Lodz, Poland).

The main components of chapters 1-4 were condensed into an article that has been published in the Journal of Mechanical Systems and Signal Processing [37].

A further article detailing the experimental study will be submitted to a MEMS specific journal, such as The Journal of Micro-electromechanical Systems, once sufficient results have been gained.

8.6 Closing remarks

This thesis centred on the design of a novel MEMS sensor: the SAW mode localization sensor. The in-depth mathematical analysis combined known methods in a novel manner to yield an accurate description of the device physics and aid experimental design. The body of work provides evidence of the feasibility and potential performance of this sensor, encouraging future experimental work into the development and optimisation of this sensor platform in multiple applications.

Appendix A. LPM Analysis Code (Mathematica)

Definition of system matrices

The following section of script defines mass and stiffness matrices described in chapter 2, section. The form of the mass and stiffness matrices are also presented below, with the nomenclature of the script highlighted.

$$\text{MXLcX} = \begin{pmatrix} 1 & \square & \square & \square & \square \\ \square & m & \square & \square & \square \\ \square & \square & 1 & \square & \square \\ \square & \square & \square & m & \square \\ \square & \square & \square & \square & 1+m_p \end{pmatrix}$$

$$\text{KXLcX} = \begin{pmatrix} 2 & -1 & \square & \square & \square \\ -1 & k+2 & -1 & \square & \square \\ \square & -1 & 2 & -1 & \square \\ \square & \square & -1 & k+2 & -1 \\ \square & \square & \square & -1 & k_p+2 \end{pmatrix}$$

- Matrices are called using the form MXLcX, where X is a place holder for a number.
- The number following the 'M' or 'K' specifies the number of DOFs in the entire system.
- The number following the 'Lc' specifies the number of DOFs in each end 'cavity'.
- In the below script the total number of DOFs must be even and range between 2 and 40. The number of DOFs per cavity can be any number from 1 to 14.

In[1]:=
```
Do[Do[Clear[Evaluate["M" <> ToString[Np - 1] <> "Lc" <> ToString[Lc]]],
  {Np, 1, 40, 2}], {Lc, 1, 8}]
Do[Do[ToExpression["M" <> ToString[Np - 1] <>
    "Lc" <> ToString[Lc] <> "=" <> ToString[
     Table[If[(i == j) ⋀ j ≤ Lc, 1, If[i == j && j > (Lc + (Np - 2 Lc)), 1 + mp, If[i == j ⋀
           OddQ[j] == OddQ[Lc + 1], m, If[i == j ⋀ OddQ[j] == OddQ[Lc + 2], 1, 0]]]],
      {i, 1, Np}, {j, 1, Np}]]], {Np, 1, 40, 2}], {Lc, 1, 14}]
Do[Do[Clear[Evaluate["K" <> ToString[Np - 1] <> "Lc" <> ToString[Lc]]],
  {Np, 1, 40, 2}], {Lc, 1, 8}]
Do[Do[ToExpression["K" <> ToString[Np - 1] <> "Lc" <> ToString[Lc] <> "=" <>
    ToString[Table[If[(i == j) ⋀ j ≤ Lc, 2, If[i == j && j > (Lc + (Np - 2 Lc)),
        2 + kp, If[i == j ⋀ OddQ[j] == OddQ[Lc + 1], 2 + k,
         If[i == j ⋀ OddQ[j] == OddQ[Lc + 2], 2, If[i == j - 1 ⋁ i == j + 1, -1, 0]]]]],
      {i, 1, Np}, {j, 1, Np}]]], {Np, 1, 40, 2}], {Lc, 1, 14}]
```

■ Examples

An example of both matrices are shown below:

```
In[5]:= M6Lc2 // MatrixForm
        K6Lc2 // MatrixForm
```

Out[5]//MatrixForm=

$$\begin{pmatrix} 1 & 0 & 0 & 0 & 0 & 0 & 0 \\ 0 & 1 & 0 & 0 & 0 & 0 & 0 \\ 0 & 0 & m & 0 & 0 & 0 & 0 \\ 0 & 0 & 0 & 1 & 0 & 0 & 0 \\ 0 & 0 & 0 & 0 & m & 0 & 0 \\ 0 & 0 & 0 & 0 & 0 & 1+mp & 0 \\ 0 & 0 & 0 & 0 & 0 & 0 & 1+mp \end{pmatrix}$$

Out[5]//MatrixForm=

$$\begin{pmatrix} 2 & -1 & 0 & 0 & 0 & 0 & 0 \\ -1 & 2 & -1 & 0 & 0 & 0 & 0 \\ 0 & -1 & 2+k & -1 & 0 & 0 & 0 \\ 0 & 0 & -1 & 2 & -1 & 0 & 0 \\ 0 & 0 & 0 & -1 & 2+k & -1 & 0 \\ 0 & 0 & 0 & 0 & -1 & 2+kp & -1 \\ 0 & 0 & 0 & 0 & 0 & -1 & 2+kp \end{pmatrix}$$

Solve for eigenvalues

```
In[8]:= Eigs = Eigensystem[Inverse[M6Lc2 /. mp → 0 /. m → 2].(K6Lc2 /. kp → 0 /. k → 0.25)];
```

- **Example plot of eigenvalues**

```
In[48]:= ListPlot[Sort[√Eigs[[1]], Less],
          PlotMarkers → {"●", 12, Blue},
          Frame → True,
          FrameStyle → Black,
          ImageSize → 350,
          FrameLabel → {{"Normalised Freq.", ""}, {"Mode Number", ""}},
          LabelStyle → {Black, FontFamily -> "Tahoma", FontSize → 16}]
```

Out[48]=

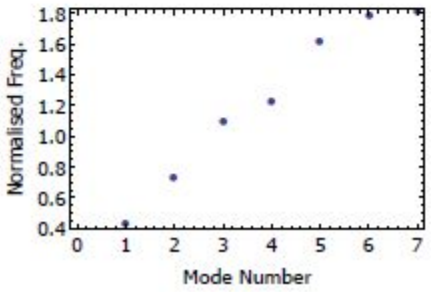

Solve for damped frequency response

```
FRF = Table[If[i = 1, 1, If[i = 23, 0, 0]], {i, 1, 23}];(* Forcing vector *)
FRβ = 0.01; (* Damping coefficient -
 Rayleigh damping stiffness matrix coefficient *)
FRζ = 0.5 FRβ Ω; (* Damping ratio *)
FRΩLL = 0; (* Frequency lower limit *)
FRΩUL = 2; (* Frequency upper limit *)
FRΩSTEP = 0.001; (* Frequency step *)
FRu0 =
 Table[Inverse[(Inverse[M22Lc4 /. mp → 0 /. m → 2].(K22Lc4 /. k → 0.25 /. kp → 0)
         (1 - i FRβ Ω) - Ω^2 IdentityMatrix[23]) /. Ω → i].
    (Inverse[M22Lc4 /. mp → 0 /. m → 2].FRF), {i, FRΩLL, FRΩUL, FRΩSTEP}];
(* Frequency response solver *)
DOF = 1;(* Degree of freedom to calculate frequency response for *)
```

- **Example frequency response plots**

```
FRAmpResp = ListLinePlot[Table[{FRQLL + i, Abs[FRu0[[All, DOF]][[1 + 1/FRQSTEP]]]},
    {i, 0, FRQUL - FRQLL, FRQSTEP}],
   PlotRange → All,
   PlotStyle → {Blue, Thickness[0.005]},
   Frame → True,
   FrameLabel → {{"Amplitude", ""}, {"Normalised Frequency", ""}},
   LabelStyle → {Black, FontFamily -> "Tahoma", FontSize → 16}];
FRPhaseResp =
  ListLinePlot[Table[{FRQLL + i, Arg[FRu0[[All, DOF]][[1 + 1/FRQSTEP]]]},
    {i, 0, FRQUL - FRQLL, FRQSTEP}],
   PlotRange → All,
   PlotStyle → {Red, Thickness[0.005]},
   Frame → True,
   FrameLabel → {{"Phase", ""}, {"Normalised Frequency", ""}},
   LabelStyle → {Black, FontFamily -> "Tahoma", FontSize → 16}];
GraphicsRow[{FRAmpResp, FRPhaseResp}, ImageSize → 800]
```

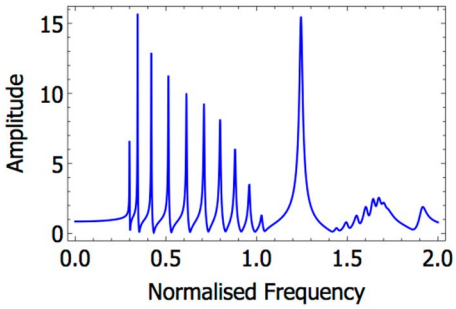

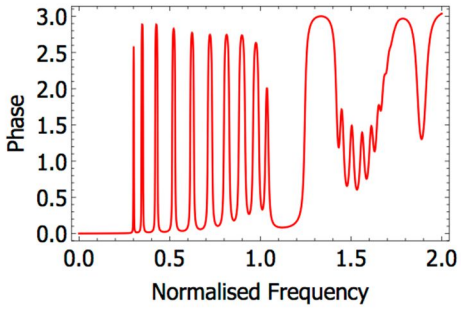

Appendix B. SAW Numerical Analysis Code (Matlab)

B1: Input code

```
%% SAW MODE LOCALIZATION SENSOR

% T. H. Hanley
% Numerical calculation of sensitivity, SNR and resolution
%% Parameters
mu = 0.5; % plating ratio
c1 = 0.975; % wave speed ratio
att = 0.001; % attenuation coefficient (29.1*(f/10^9)^2 Nepers/m Bell & Li)
Nc = 50:10:220; % periods in coupling array
f = 0.978:0.000001:0.997; % frequencies vector
eta = 0.95:0.001:1.05; % sense cavity disorder
La = 1; % reference cavity length (in wavelengths - can be non-integer)
Lb = 1; % sense cavity length
P0 = 1; % excitation load N/m
rho = 2650; % density of Quartz
deltaeta = 0.064; % maximum physical change in eta
sm = 29e9; % shear modulus of quartz
lambda = 20e-6; % wavelength of interest
kbT = 1.38e-23*300; % Boltzmann's constant multiplied by ambient
temperature
cR = 3158;% Rayleigh wave speed of ST-cut Quartz
Q = 10^5; % quality factor
%% Frequency dependent transmission and reflection coefficients
ep = 0.5*(c1+1/c1);
em = 0.5*(c1-1/c1);
w = zeros(1,length(f));
z = zeros(1,length(f));
zeta = zeros(1,length(f));
trns = zeros(length(Nc),length(f));
ref = zeros(length(Nc),length(f));
for i = 1:length(f)
    for j = 1:length(Nc)
w(i) = (cos((pi*mu*f(i))/c1)-
1i*ep*sin((pi*mu*f(i))/c1))*exp(1i*pi*mu*f(i));
z(i) =  -1i*em*sin((pi*mu*f(i))/c1);
zeta(i) = real(w(i))*cos(pi*f(i))+imag(w(i))*sin(pi*f(i));
trns(j,i) =  exp(-att*Nc(j))/((w(i)*exp(-1i*pi*f(i))*...
    (sin((Nc(j))*acos(zeta(i)))/sin(acos(zeta(i))))...
    -(sin((Nc(j)-
1)*acos(zeta(i)))/sin(acos(zeta(i)))))*exp(1i*pi*mu*f(i)));
ref(j,i) =
z(i)*(sin((Nc(j))*acos(zeta(i)))/sin(acos(zeta(i))))*trns(j,i)*exp(att*Nc(j
));
    end
end

%% Find stop band centre
[tmin,fcind] = min(abs(trns(1,:)));
fc = f(fcind);% centre frequency (non-dimensional)
a = 2*La/fc; % length of reference cavity
b = 2*Lb/fc; % length of sense cavity

%% Assemble wavenumber arrays
gamma_a = pi.*f - ones(1,length(f))*1i*att; % non-dimensional complex
wavenumber vector in ref cavity
```

```
gamma_b = zeros(length(eta),length(f));
for i = 1:length(eta)
    for j= 1:length(f)
gamma_b(i,j) = eta(i)*pi*f(j) - 1i*att; % non-dimensional complex
wavenumber matrix in sense cavity
    end
end

%% Cavity Amplitude Frequency Responses
xA=cell(length(Nc));
xB=cell(length(Nc));
xC=cell(length(Nc));
for j = 1:length(Nc)
xA{j} = -ref(j,:).*exp((1i*2*a).*gamma_a);
%xB = zeros(length(eta),length(f));
%xC = zeros(length(eta),length(f));
for i = 1:length(eta)
xB{j}(i,:) =
(trns(j,:).^2).*exp(((1i*2*a).*gamma_a)+((1i*2*b).*gamma_b(i,:)));
xC{j}(i,:) = -ref(j,:).*exp((1i*2*b).*gamma_b(i,:));
end
%XR=zeros(length(eta),length(f));
%XS=zeros(length(eta),length(f));
for i = 1:length(eta)
XR{j}(i,:) = (1-xC{j}(i,:))./(sm.*(1-xA{j}-xB{j}(i,:)-
xC{j}(i,:)+xA{j}.*xC{j}(i,:)));
XS{j}(i,:) = (-
trns(j,:).*exp(2*1i.*(gamma_a.*a+gamma_b(i,:).*b))./(sm.*(1-xA{j}-
xB{j}(i,:)-xC{j}(i,:)+xA{j}.*xC{j}(i,:)));
end
end
%% Eigenvalue loci and tracking modal amplitudes
for i = 1:length(eta)
    for j=1:length(Nc)
[PKS1 LOCS1] = findpeaks(abs(XR{j}(i,:)));
if length(LOCS1(:)) == 1
    wn{j,i} = [f(LOCS1(1)) NaN];
    XRAMP{j,i} = [abs(XR{j}(i,LOCS1(1))) NaN];
    XSAMP{j,i} = [abs(XS{j}(i,LOCS1(1))) NaN];
else
    wn{j,i} = [f(LOCS1(1)) f(LOCS1(2))];
    XRAMP{j,i} = [abs(XR{j}(i,LOCS1(1))) abs(XR{j}(i,LOCS1(2)))];
    XSAMP{j,i} = [abs(XS{j}(i,LOCS1(1))) abs(XS{j}(i,LOCS1(2)))];
end
    end
end
wnLOW=zeros(length(Nc),length(eta));
wnHIGH=zeros(length(Nc),length(eta));
for i = 1:length(eta)
    for j= 1:length(Nc)
wnLOW(j,i)=wn{j,i}(1);
wnHIGH(j,i)=wn{j,i}(2);
end
end
%% Reference cavity modal amplitudes
XRLOW=zeros(length(Nc),length(eta));
XRHIGH=zeros(length(Nc),length(eta));
for i = 1:length(eta)
    for j=1:length(Nc)
XRLOW(j,i)=XRAMP{j,i}(1);
XRHIGH(j,i)=XRAMP{j,i}(2);
```

```
    end
end

%% Sense cavity modal amplitudes
XSLOW=zeros(length(Nc),length(eta));
XSHIGH=zeros(length(Nc),length(eta));
for i = 1:length(eta)
    for j = 1:length(Nc)
XSLOW(j,i)=XSAMP{j,i}(1);
XSHIGH(j,i)=XSAMP{j,i}(2);
    end
end

%% Amplitude ratios
for j =1:length(Nc)
AMPRATLOW{j} = XRLOW(j,:)./XSLOW(j,:);
AMPRATHIGH{j} = XRHIGH(j,:)./XSHIGH(j,:);
end



%% Find linear sensitivity coefficient
for j = 1:length(Nc)
Coeffs{j} =
polyfit(eta(3*floor(length(eta)/4):end),AMPRATHIGH{j}(3*floor(length(eta)/4
):end),1);
LinSens{j} = @(x) Coeffs{j}(1)*x+Coeffs{j}(2);
end
%% Noise calculations (in the context of the magnetic field sensor of
chpt.6)
% Parameters
fdn = (fc*cR)/(lambda); % dimensionalised frequency (Hz)
wdn = 2*pi*fdn; % angular frequency
deltaf = fdn/Q; % bandwidth
C1=zeros(length(Nc),1);
for j = 1:length(Nc)
C1(j) = Coeffs{j}(1); % linear sensitivity coefficient
end
refamp = 10e-12; % 10 picometer reference amplitude

% SNR
% SNR=(1000*pi*sm^2*Q*C1^2*deltaeta^2*refamp^2)/(4*kbT*wdn^2*rho*a);

% Magnetometer resolution (Limit of detection)
LODMAG2 = zeros(length(Nc),1);
for j = 1:length(Nc)
LODMAG2(j) =
sqrt((100*kbT*wdn^2*a*rho)/(C1(j)^2*refamp^2*pi*Q*sm^2*deltaf));
disp(['Field Sensitivity = ',num2str(LODMAG2(j)*1e9),' nT/sqrt(Hz)'])
end
%% Plots

% Plot transmission and reflection coefficients frequency behaviour
figure
hold on
plot(f,abs(trns))
plot(f,abs(ref))
xlim([f(1) f(length(f))])
t1 = title('Transmission Spectrum');
lx1 = xlabel('Normalised frequency');
```

```
ly1 = ylabel('|T_N| and |R_N|');
for i = 1:length(Nc)
leg1{i} = ['Nc = ',num2str(Nc(i))];
end
legend(leg1,'location','northeastoutside')
set([t1, lx1, ly1]                , ...
    'FontName'   , 'Helvetica'    ,...
    'FontSize'   , 14             );
hold off

% Plot cavity amplitude frequency response for symmetric case
figure
subplot(121)
hold on
plot(f,abs(XR{1}(floor(length(eta)/2),:)))
plot(f,abs(XS{1}(floor(length(eta)/2),:)),'r--')
xlim([f(1) f(length(f))])
t2 = title('Cavity Amplitude Responses (\eta=1)');
lx2 = xlabel('Normalised frequency');
ly2 = ylabel('Amplitude (m)');
legend('Reference Cavity', 'Sense Cavity')
set([t2, lx2, ly2]                , ...
    'FontName'   , 'Helvetica'    ,...
    'FontSize'   , 14             );
hold off

% Plot cavity amplitude frequency response for an asymmetric case
subplot(122)
hold on
plot(f,abs(XR{1}(floor(length(eta)/2)+50,:)))
plot(f,abs(XS{1}(floor(length(eta)/2)+50,:)),'r--')
xlim([f(1) f(length(f))])
t3 = title('Cavity Amplitude Responses (\eta=1.049)');
lx3 = xlabel('Normalised frequency');
ly3 = ylabel('Amplitude (m)');
legend('Reference Cavity', 'Sense Cavity')
set([t3, lx3, ly3]                , ...
    'FontName'   , 'Helvetica'    ,...
    'FontSize'   , 14             );
hold off

% Plot eigenvalue loci
figure
hold on
plot(eta,wnLOW)
plot(eta,wnHIGH)
xlim([eta(1) eta(length(eta))])
t4 = title('Eigenvalue Loci Veering');
lx4 = xlabel('\eta');
ly4 = ylabel('Normalised natural frequency');
legend(leg1,'location','northeastoutside')
set([t4, lx4, ly4]                , ...
    'FontName'   , 'Helvetica'    ,...
    'FontSize'   , 14             );
hold off

% Plot reference cavity modal amplitudes against wave-speed ratio
figure
subplot(121)
hold on
```

```
plot(eta,XRLOW(10:(length(Nc)),:))
plot(eta,XRHIGH(10:(length(Nc)),:))
xlim([eta(1) eta(length(eta))])
t5 = title('Reference Cavity Modal Displacement Amplitude');
lx5 = xlabel('\eta');
ly5 = ylabel('Reference cavity amplitude at resonance (m)');
for i = 10:length(Nc)
leg5{i-9} = ['Nc = ',num2str(Nc(i))];
end
legend(leg5)
set([t5, lx5, ly5]                 , ...
    'FontName'   , 'Helvetica'    ,...
    'FontSize'   , 14             );
hold off

% Plot sense cavity modal amplitudes against wave-speed ratio
subplot(122)
hold on
plot(eta,XSLOW(10:(length(Nc)),:))
plot(eta,XSHIGH(10:(length(Nc)),:))
xlim([eta(1) eta(length(eta))])
t6 = title('Sense Cavity Modal Displacement Amplitude');
lx6 = xlabel('\eta');
ly6 = ylabel('Sense cavity amplitude at resonance (m)');
legend(leg5)
set([t6, lx6, ly6]                 , ...
    'FontName'   , 'Helvetica'    ,...
    'FontSize'   , 14             );
hold off

% Plot change in amplitude ratio against wave-speed ratio and linear fit
% (Calibration curve)
figure
hold on
plot(eta,AMPRATHIGH{1},'r.')
fplot(LinSens{1},[1 1.05])
xlim([1 eta(length(eta))])
t7 = title('Calibration curve');
lx7 = xlabel('\eta');
ly7 = ylabel('Amplitude ratio');
legend('Quasi-linear device response','Linear fit')
set([t7, lx7, ly7]                 , ...
    'FontName'   , 'Helvetica'    ,...
    'FontSize'   , 14             );
hold off

% Plot change in field sensitivity in the presence of noise with length of
% coupling array
figure
plot(Nc,(LODMAG2.*1e9))
xlim([Nc(1) Nc(length(Nc))])
t8 = title('Magnetic field sensitivity');
lx8 = xlabel('Number of periods in coupling array');
ly8 = ylabel('Field sensitivity (nT/sqrt(Hz))');
grid on
grid minor
set( [t8, lx8, ly8]                          , ...
    'FontName'   , 'Helvetica'    ,...
    'FontSize'   , 14             );
```

B2: Output plots

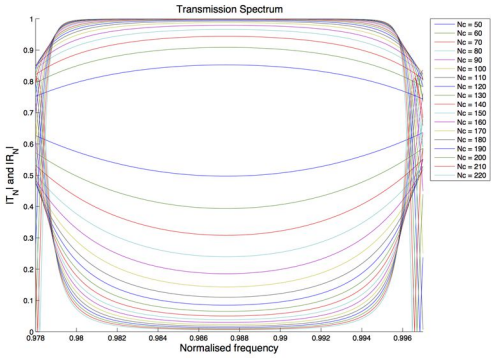

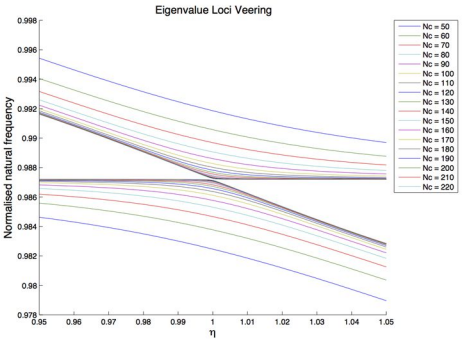

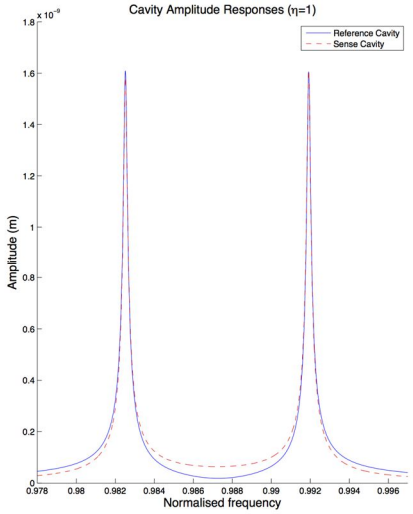

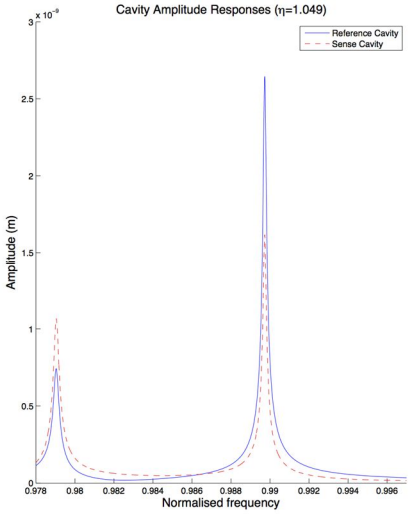

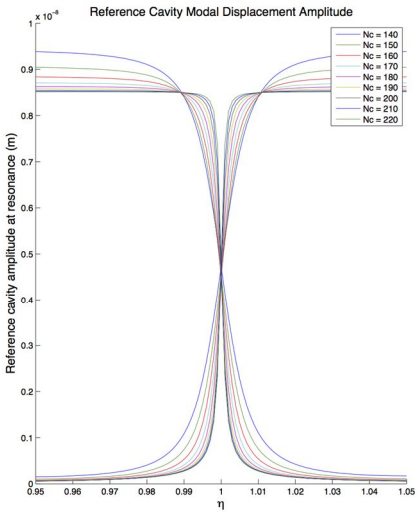
Reference Cavity Modal Displacement Amplitude
x 10^-8
Reference cavity amplitude at resonance (m)
η
Nc = 140
Nc = 150
Nc = 160
Nc = 170
Nc = 180
Nc = 190
Nc = 200
Nc = 210
Nc = 220

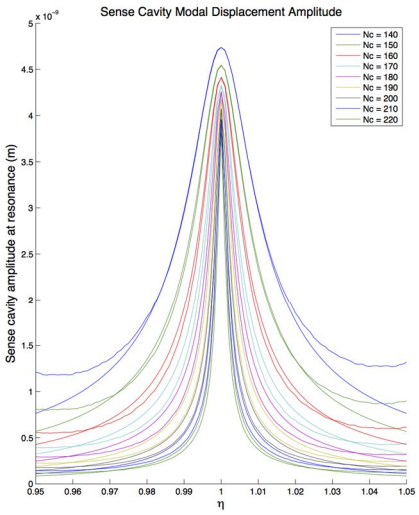
Sense Cavity Modal Displacement Amplitude
x 10^-9
Sense cavity amplitude at resonance (m)
η
Nc = 140
Nc = 150
Nc = 160
Nc = 170
Nc = 180
Nc = 190
Nc = 200
Nc = 210
Nc = 220

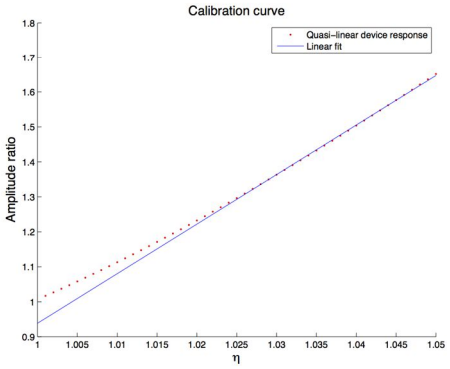
Calibration curve
Quasi−linear device response
Linear fit
Amplitude ratio
η

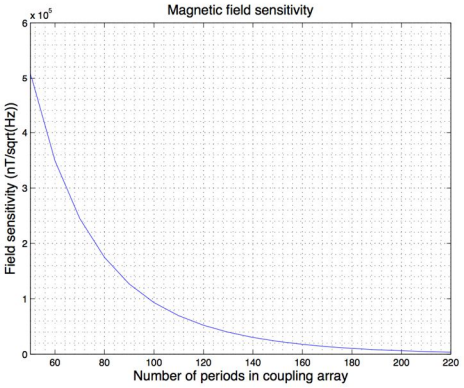
Magnetic field sensitivity
x 10^5
Field sensitivity (nT/sqrt(Hz))
Number of periods in coupling array

References

[1] L. Nicu and C. Bergaud, "Modeling of a tuning fork biosensor based on the excitation of one particular resonance mode," *J. Micromechanics Microengineering*, vol. 14, no. 5, pp. 727–736, 2004.

[2] M. Spletzer, A. Raman, A. Q. Wu, X. Xu, and R. Reifenberger, "Ultrasensitive mass sensing using mode localization in coupled microcantilevers," *Appl. Phys. Lett.*, vol. 88, no. 25, p. 254102, 2006.

[3] P. Thiruvenkatanathan, J. Yan, J. Woodhouse, A. Aziz, and A. A. Seshia, "Ultrasensitive mode-localized mass sensor with electrically tunable parametric sensitivity," *Appl. Phys. Lett.*, vol. 96, no. 8, p. 81913, 2010.

[4] L. Brillouin, *Wave propagation in periodic structures*. New York: Dover Publications Inc., 1946.

[5] G. Floquet, "Sur les équations différentielles linéaires à coefficients périodiques," *Ann. Sci. l'École Norm. Supérieure*, vol. 12, pp. 47–88, 1883.

[6] C. Elachi, "Waves in active and passive periodic structures: a review.," *Proc. IEEE*, vol. 64, no. 12, pp. 1666–1698, 1976.

[7] D. J. Mead, "Wave Propagation in Continuous Periodic Structures: Research Contributions From Southampton, 1964–1995," *J. Sound Vib.*, vol. 190, no. 3, pp. 495–524, Feb. 1996.

[8] D. J. Mead, "Wave propagation and natural modes in periodic systems: I. Mono-coupled systems," *J. Sound Vib.*, vol. 40, pp. 1–18, 1975.

[9] D. J. Mead, "Wave propagation and natural modes in periodic systems: II. Multi-coupled systems, with and without damping," *J. Sound Vib.*, vol. 40, no. 1, pp. 19–39, May 1975.

[10] D. J. Mead and A. S. Bansal, "Mono-coupled periodic systems with a single disorder: Free wave propagation," *J. Sound Vib.*, vol. 61, no. 4, pp. 481–496, Dec. 1978.

[11] D. J. Mead, "A new method of analyzing wave propagation in periodic structures;

Applications to periodic timoshenko beams and stiffened plates," *J. Sound Vib.*, vol. 104, no. 1, pp. 9–27, Jan. 1986.

[12] D. J. Mead, "A general theory of harmonic wave propagation in linear periodic systems with multiple coupling," *J. Sound Vib.*, vol. 27, no. 2, pp. 235–260, 1973.

[13] M. G. Faulkner and D. P. Hong, "Free vibrations of a mono-coupled periodic system," *J. Sound Vib.*, vol. 99, no. 1, pp. 29–42, 1985.

[14] D. J. Griffiths and C. A. Steinke, "Waves in locally periodic media," *Am. J. Phys.*, vol. 69, no. 2, p. 137, 2001.

[15] P. Pereyra and E. Castillo, "Theory of finite periodic systems: General expressions and various simple and illustrative examples," *Phys. Rev. B*, vol. 65, no. 20, p. 205120, May 2002.

[16] M. I. Hussein, "Wave Motion in Periodic Flexural Beams and Characterization of the Transition Between Bragg Scattering and Local Resonance," *J. Appl. Mech.*, vol. 79, no. January, pp. 1–17, 2012.

[17] E. K. Sittig and G. A. Coquin, "Filters and Dispersive Delay Lines Using Repetitively Mismatched Ultrasonic Transmission Lines," *IEEE Trans. Sonics Ultrason.*, vol. 15, no. 2, pp. 111–119, 1968.

[18] P. Pereyra, "Eigenvalues, eigenfunctions, and surface states in finite periodic systems," *Ann. Phys. (N. Y).*, vol. 320, no. 1, pp. 1–20, Nov. 2005.

[19] P. Pereyra, "Erratum to 'Eigenvalues, eigenfunctions, and surface states in finite periodic systems' [Ann. Phys. 320 (2005) 1-20] (DOI:10.1016/j.aop.2005.05.010)," *Ann. Phys. (N. Y).*, vol. 321, no. 5, p. 1276, 2006.

[20] P. W. Anderson, "Local moments and localized states," *Rev. Mod. Phys.*, vol. 50, no. 2, pp. 191–201, 1978.

[21] I. A. Butt and J. A. D. Wattis, "Discrete breathers in a two-dimensional Fermi–Pasta–Ulam lattice," *J. Phys. A. Math. Gen.*, vol. 39, no. 18, pp. 4955–4984, May 2006.

[22] M. Spletzer, A. Raman, H. Sumali, and J. P. Sullivan, "Highly sensitive mass detection

and identification using vibration localization in coupled microcantilever arrays," *Appl. Phys. Lett.*, vol. 92, no. 11, p. 114102, 2008.

[23] R. C. and D. Hilbert, *Methods of Mathematical Physics*, vol. 1. New York: Interscience, 1953.

[24] P. Thiruvenkatanathan, J. Woodhouse, J. Yan, and A. A. Seshia, "Limits to mode-localized sensing using micro- and nanomechanical resonator arrays," *J. Appl. Phys.*, vol. 109, no. 10, p. 104903, 2011.

[25] P. Thiruvenkatanathan, S. Member, J. Yan, J. Woodhouse, and A. A. Seshia, "Enhancing Parametric Sensitivity in Electrically Coupled MEMS Resonators," vol. 18, no. 5, pp. 1077–1086, 2009.

[26] C. Pierre, "Mode Phenomena and Eigenvalue Loci Veering," *J. Sound Vib.*, vol. 126, no. 3, pp. 485–502, 1988.

[27] P. Thiruvenkatanathan, J. Woodhouse, J. Yan, and a. a. Seshia, "Limits to mode-localized sensing using micro- and nanomechanical resonator arrays," *J. Appl. Phys.*, vol. 109, no. 10, p. 104903, 2011.

[28] T. J. Ryan, J. A. Judge, J. F. Vignola, and A. A. Glean, "Noise sensitivity of a mass detection method using vibration modes of coupled microcantilever arrays," *Appl. Phys. Lett.*, vol. 101, no. 4, pp. 10–14, 2012.

[29] T. J. Ryan, "A Coupled Microresonator Array for Mass Detection," The Catholic University of America, 2013.

[30] B. E. DeMartini, J. F. Rhoads, S. W. Shaw, and K. L. Turner, "A single input-single output mass sensor based on a coupled array of microresonators," *Sensors Actuators, A Phys.*, vol. 137, no. 1, pp. 147–156, 2007.

[31] B. E. DeMartini, J. F. Rhoads, M. a. Zielke, K. G. Owen, S. W. Shaw, and K. L. Turner, "A single input-single output coupled microresonator array for the detection and identification of multiple analytes," *Appl. Phys. Lett.*, vol. 93, no. 5, pp. 1–4, 2008.

[32] E. Gil-Santos, D. Ramos, A. Jana, M. Calleja, A. Raman, and J. Tarnayo, "Mass sensing based on deterministic and stochastic responses of elastically coupled nanocantilevers,"

Nano Lett., vol. 9, no. 12, pp. 4122–4127, 2009.

[33] H. Pakdast and M. Lazzarino, "Triple coupled cantilever systems for mass detection and localization," *Sensors Actuators, A Phys.*, vol. 175, pp. 127–131, 2012.

[34] T. Chopard, A. Bienaime, C. Elie-Caille, and T. Leblois, "High Sensitive Mass Detection using Piezoelectric Coupled Microcantilevers," *Procedia Eng.*, vol. 47, pp. 350–353, 2012.

[35] M. K. Zalalutdinov, J. W. Baldwin, M. H. Marcus, R. B. Reichenbach, J. M. Parpia, and B. H. Houston, "Two-dimensional array of coupled nanomechanical resonators," *Appl. Phys. Lett.*, vol. 88, no. 14, pp. 2004–2007, 2006.

[36] T. H. Hanley, B. J. Gallacher, and H. T. D. Grigg, "Towards the exploitation of local resonances for novel MEMS devices," in *Proceedings of the 13th International Conference on Dynamical Systems - Theory and Applications: Dynamical Systems - Mechatronics and Life Sciences*, 2015, pp. 207–216.

[37] T. H. Hanley, B. J. Gallacher, and H. T. D. Grigg, "On the Exploitation of Mode Localization in Surface Acoustic Wave MEMS," *Mech. Syst. Signal Process.*, vol. 89, pp. 27–26, 2017.

[38] B. K. Sinha and H. F. Tiersten, "Variational analysis of the reflection of surface waves by arrays of reflecting strips," *J. Appl. Phys.*, vol. 47, no. 7, pp. 2824–2832, 1976.

[39] J. D. Achenbach, *Wave Propagation in Elastic Solids*. Amsterdam: North-Holland Pub. Co., 1975.

[40] K. F. Graff, *Wave motion in elastic solids*. New York: Dover Publications Inc., 1991.

[41] P. H. Mott and C. M. Roland, "Limits to Poisson's ratio in isotropic materials," *Phys. Rev. B - Condens. Matter Mater. Phys.*, vol. 80, no. 13, pp. 1–4, 2009.

[42] H. F. Tiersten, "Elastic surface waves guided by thin films," *J. Appl. Phys.*, vol. 40, no. 2, pp. 770–789, 1969.

[43] B. K. Sinha, "Elastic and piezoelectric surface waves guided by thin films," *J. Appl. Phys.*, vol. 44, no. 11, p. 4831, 1973.

[44] D. F. Thompson and B. A. Auld, “Surface Transverse Wave Propagation Under Metal Strip Gratings,” *IEEE 1986 Ultrason. Symp.*, pp. 261–266, 1986.

[45] D. H. Cortes, S. K. Datta, and O. M. Mukdadi, “Elastic guided wave propagation in a periodic array of multi-layered piezoelectric plates with finite cross-sections.,” *Ultrasonics*, vol. 50, no. 3, pp. 347–56, Mar. 2010.

[46] V. Plessky and J. Koskela, “Coupling-of-Modes Analysis of Saw Devices,” *Int. J. High Speed Electron. Syst.*, vol. 10, no. 4, pp. 867–947, 2000.

[47] H.-S. Tuan, “Rayleigh-wave reflection from groove and step discontinuities,” *J. Acoust. Soc. Am.*, vol. 55, no. 6, p. 1212, 1974.

[48] D. A. Simons, “Scattering of normally incident Rayleigh waves by thin strips,” *J. Acoust. Soc. Am.*, vol. 60, no. 5, p. 1100, 1976.

[49] D. A. Simons, “Reflection of Rayleigh waves by strips, grooves, and periodic arrays of strips or grooves,” *J. Acoust. Soc. Am.*, vol. 63, no. 5, p. 1292, 1978.

[50] H. Lamb, “On the Propagation of Tremors over the Surface of an Elastic Solid,” *Philos. Trans. R. Soc. London A Math. Phys. Eng. Sci.*, vol. 203, no. 359–371, pp. 1–42, Jan. 1904.

[51] W. M. Ewing, W. S. Jardetzky, and F. Press, *Elastic waves in layered media*. New York: McGraw-Hill, 1957.

[52] M. Bath, *Mathematical aspects of seismology*. Amsterdam: Elsevier, 1968.

[53] N. S. Clarke and J. S. Burdess, “A Rayleigh Resonator,” *Wave Motion*, vol. 13, pp. 193–200, 1991.

[54] F. Lanza di Scalea, H. Matt, and I. Bartoli, “The response of rectangular piezoelectric sensors to Rayleigh and Lamb ultrasonic waves,” *J. Acoust. Soc. Am.*, vol. 121, no. 1, p. 175, 2007.

[55] K. Y. Hashimoto, *Surface Acoustic Wave Devices in Telecommunications*. Berlin: Springer-Verlag, 2000.

[56] C. K. Campbell, *Surface acoustic wave devices for mobile and wireless communications*. Orlando, FL: Academic Press, 1998.

[57] S. Datta and B. J. Hunsinger, "First-order reflection coefficient of surface acoustic waves from thin-strip overlays," *J. Appl. Phys.*, vol. 50, no. 9, p. 5661, 1979.

[58] P. S. Cross and R. V. Schmidt, "Coupled Surface Acoustic Wave Resonators," *Bell Syst. Tech. J.*, vol. 56, no. 8, pp. 1447–1482, 1977.

[59] P. S. Cross, W. H. Haydl, and R. S. Smith, "Design and Applications of Two-Port SAW Resonators on YZ-Lithium Niobate," *Proc. IEEE*, vol. 64, no. 5, pp. 682–685, 1976.

[60] T. Kannan, "Finite Element Analysis of Surface Acoustic Wave Resonators," University of Saskatchewan, 2006.

[61] Z. Knittl, *Optics of Thin Films*. London: John Wiley & Sons, Inc., 1976.

[62] B. J. Gallacher, "Principles of a Micro-Rate Integrating Ring Gyroscope," *IEEE Trans. Aerosp. Electron. Syst.*, vol. 48, no. 1, 2012.

[63] B. J. Gallacher, J. S. Burdess, and K. M. Harish, "A control scheme for a MEMS electrostatic resonant gyroscope excited using combined parametric excitation and harmonic forcing," *J. Micromechanics Microengineering*, vol. 16, no. 2, pp. 320–331, Feb. 2006.

[64] C. Pierre and E. H. Dowell, "Localization of vibrations by structural irregularity," *J. Sound Vib.*, vol. 114, no. 3, pp. 549–564, 1987.

[65] D. T. Bell and R. C. M. Li, "Surface-Acoustic-Wave Resonators," *Proc. IEEE*, vol. 64, 1976.

[66] E. J. Staples, J. S. Schoenwald, R. C. Rosenfeld, and C. S. Hartmann, "UHF surface acoustic wave resonators," in *IEEE Ultrasonics Symposium*, 1974, pp. 245–252.

[67] R. C. M. Li, J. A. Alusow, and R. C. Williamson, "The Physics and Equivalent Circuit of the Basic Saw Resonator," in *1976 IEEE-MTT-S International Microwave Symposium*, 1976, pp. 280–282.

[68] R. C. M. Li, R. C. Williamson, D. C. Flanders, and J. A. Alusow, “On the Performance and Limitations of the Surface-Wave Resonator Using Grooved Reflectors,” in *IEEE Ultrasonics Symposium*, 1974, pp. 257–262.

[69] H. T. D. Grigg, “The Principles and Practice of the Xylophone Bar Magnetometer,” Newcastle University, 2013.

[70] T. B. Gabrielson, “Mechanical-Thermal Noise in Micromachined Acoustic and Vibration Sensors,” *IEEE Trans. Electron Devices*, vol. 40, no. 5, pp. 903–909, 1993.

[71] F. Mohd-Yasin, D. J. Nagel, and C. E. Korman, “Noise in MEMS,” *Meas. Sci. Technol.*, vol. 21, no. 1, p. 12001, 2009.

[72] J. Lenz and S. Edelstein, “Magnetic sensors and their applications,” *IEEE Sens. J.*, vol. 6, no. 3, pp. 631–649, 2006.

[73] A. L. Herrera-May, L. A. Aguilera-Cortés, P. J. García-Ramírez, and E. Manjarrez, “Resonant Magnetic Field Sensors Based On MEMS Technology.,” *Sensors (Basel).*, vol. 9, no. 10, pp. 7785–813, 2009.

[74] P. Ripka and M. Janosek, “Advances in Magnetic Field Sensors,” *IEEE Sens. J.*, vol. 10, no. 6, pp. 1108–1116, 2010.

[75] A. Clark and H. Savage, “Giant Magnetically Induced Changes in the Elastic Moduli in Tb Dy Fe,” *IEEE Trans. Sonics Ultrason.*, vol. 22, no. 1, pp. 50–52, 1974.

[76] D. K. Wickenden, T. J. Kistenmacher, R. Osiander, and S. A. Ecelberger, “Development of Miniature Magnetometers,” *John Hopkins APL Tech. Dig.*, vol. 18, no. 2, 1997.

[77] R. Osiander, S. A. Ecelberger, R. B. Givens, D. K. Wickenden, J. C. Murphy, and T. J. Kistenmacher, “A microelectromechanical-based magnetostrictive magnetometer,” *Appl. Phys. Lett.*, vol. 69, no. 19, p. 2930, 1996.

[78] M. Yamaguchi, K. Y. Hashimoto, H. Kogo, and M. Naoe, “Variable Saw Delay Line Using Amorphous TbFe2 Film,” *IEEE Trans. Magn.*, vol. 16, no. 5, pp. 916–918, 1980.

[79] K. Y. Hashimoto, M. Yamaguchi, and H. Kogo, “Magnetostrictive Properties of Sputtered Co-Cr Film on Surface Acoustic Wave,” *IEEE Trans. Magn.*, vol. 17, no. 6,

pp. 3181–3183, 1981.

[80] S. M. Hanna, “Magnetic Field Sensors Based on SAW Propagation in Magnetic Films.,” *IEEE Trans. Ultrason. Ferroelectr. Freq. Control*, vol. 34, no. 2, pp. 191–4, 1987.

[81] W. Li, P. Dhagat, and A. Jander, “Surface Acoustic Wave Magnetic Sensor using Galfenol Thin Film,” *IEEE Trans. Magn.*, vol. 48, no. 11, pp. 4100–4102, Nov. 2012.

[82] A. K. Ganguly, K. L. Davis, D. C. Webb, C. Vittoria, and D. W. Forester, “Magnetically Tuned Surface-Acoustic-Wave Phase Shifter,” *Electron. Lett.*, vol. 11, pp. 610–611, 1975.

[83] H. T. D. Grigg and B. J. Gallacher, “Efficient Parametric Optimisation of Support Loss in MEMS beam resonators via an enhanced Rayleigh-Ritz method,” *J. Phys. Conf. Ser.*, vol. 382, p. 12028, Aug. 2012.

[84] Z. Hao, A. Erbil, and F. Ayazi, “An analytical model for support loss in micromachined beam resonators with in-plane flexural vibrations,” *Sensors Actuators A Phys.*, vol. 109, no. 1–2, pp. 156–164, Dec. 2003.

[85] S. Rao, *Vibration of Continuous Systems*. New Jersey: John Wiley & Sons, Inc., 2007.

[86] M. Cross and R. Lifshitz, “Elastic wave transmission at an abrupt junction in a thin plate with application to heat transport and vibrations in mesoscopic systems,” *Phys. Rev. B*, vol. 64, no. 8, p. 85324, Aug. 2001.

[87] G. Rogers, “A diameter 300 μm Bragg reflector for acoustic isolation of resonant micro-actuators,” *J. Micromechanics Microengineering*, vol. 21, no. 4, p. 42001, Apr. 2011.

[88] T. Yang, J.Ono and M. Esashi, “Energy dissipation in submicrometer thick single-crystal silicon cantilevers,” *J. Microelectromechanical Syst.*, vol. 11, no. 6, pp. 775–783, Dec. 2002.

[89] T. H. Hanley, B. J. Gallacher, and H. T. D. Grigg, “Support-Q Optimisation of a Trapped Mode Beam Resonator,” in *Proceedings of the 2014 COMSOL Conference in Cambridge*, 2014.

[90] T. E. Parker and G. K. Montress, “Precision Surface-Acoustic-Wave (SAW)

Oscillators," *IEEE Trans. Ultrason. Ferroelectr. Freq. Control*, vol. 35, no. 3, pp. 342–364, 1988.